Developing high spatial and temporal resolution structured illumination microscopy to study the dynamics of scaffolding proteins FtsZ and MipZ in *Rhodobacter sphaeroides*



Stephen Maughan
Worcester College
University of Oxford

A thesis submitted for the degree of
Doctor of Philosophy
Michaelmas Term 2023

ABSTRACT

Super resolution microscopy has been a transformational tool for biologists, allowing the structures and dynamics which together constitute form the cell to be studied at up to 10x the resolution previously available. Amongst other things, super resolution techniques have improved our understanding of bacterial cell division, for example the role of MipZ in regulating the polymerisation of FtsZ in *Rhodobacter sphaeroides*. Structured Illumination Microscopy (SIM) is a popular super resolution technique due to its ability to image bulk fluorescence using conventional fluorescent fluorophores at speeds suitable for imaging moderate speed (up to 90 nm/s) dynamics, despite generally being limited to only a 2x spatial resolution improvement over the resolution of a widefield fluorescence microscope. This is determined by the Numerical Aperture (NA) and therefore, to improve the resolution of SIM, the NA of the underlying widefield microscope would have to be improved.

Here, I investigate combining SIM with a Solid Immersion Lens (SIL); a high refractive index hyper-hemispherical lens which replaces both the immersion medium and coverslip, providing a 1.4x increase in NA, in a way which is compatible with live cell imaging. I detail the design considerations of such a system, including the method to spatially modulate and maintain the polarisation of the illumination and mounting the SIL.

In this DPhil project, the aim was to apply this combination of techniques, complemented by an *in vitro* study and other microscopy modalities, to further examine the ring-like structure which MipZ forms at mid-cell with FtsZ, as discovered previously This behaviour is very different to that described in studies of other α-proteobacteria where MipZ prevents the polymerisation of FtsZ by forming a bipolar gradient, causing FtsZ to polymerise at mid-cell. I confirm that MipZ is diffusing between the poles and mid-cell and present evidence that FtsZ is exhibiting treadmilling behaviour as has been observed in other bacterial species.

ACKNOWLEDGEMENTS

I would like to gratefully acknowledge the BBSRC for funding my research, STFC, the DTC and the Micron Advanced Bioimaging Facility.

I would like to thank my supervisors Judy, Lin, George, Richard and Mark for their support throughout this project. In particular, I would like to thank Mark, who has taught me so much and who has been so supportive over the past three years. Mark, I will be eternally grateful for the faith you put in me to finish this thesis and your commitment in getting me to the finish line.

I'm very grateful to Richard Berry and Ben Berks for making space for me and making me feel so welcome in their labs, which also happened to be filled with some really wonderful people. Thanks to Jad, Sam, Camilla, Xiaolong, Jim, Andreas and Fred and the rest of the Berks lab for a huge amount of advice, but also a lot of fun and treating me as one of your own. Thanks to Helen, Robert, and the rest of the Berry lab for your help and the strangest group photo I will ever be in!

To Alasdair, Amy, Connor, Megan and Sumanth: thanks for adding fun to some tough times.

To my Refeyn colleagues: I'm hugely grateful to all of you who have given me back my drive and passion for helping people measure small stuff; especially my managers Svea and Catia.

Thanks to the brilliant people of the DTP and in particular Anna, Lea and Sofia for being such lovely housemates. Thanks to Will, Hannah, John, Anna, Laura & Jamie, Patricia & the late Phillip, the late Janet and all the people at the University Church for being such wonderful friends and always being there for me.

I'd like to thank to all those I have known at Worcester College throughout the years, in particular Ellen and Rory who had such a positive effect on the experience of so many members there.

Thank you to Sam, Lauren, Michelle, Tor, Tom and the rest of the corner crew for your many years of friendship prior to, during, and hopefully post DPhil life. A special mention must go to Michelle who was such an inspiration pursuing her PhD.

I'm so grateful to Katie and my fellow HAB Patrick for making watching rowing a whole lot more fun and being there whenever beer was required. Thank you to Signe and Tom for some truly special times and getting me through many of the lows; and to Nicola for your supportive messages, pandemic walks and generally being my fellow Worcester College-member, church-going northerner who is interested in imaging!

Thanks to my mam, dad, brother, grandma and the rest of my family for all of their support over the last 6 years. Like all things, I really could not have done it without them, and I am sorry to them for all the times when my answer to the question "How is it going?" was not as constructive or informative as they would have liked!

Finally, and most importantly, thank you to my best friend, wife and soulmate Renée. Your love and care, in addition to your inspirational science have fuelled me through the last 6 years. I look forward to having my evenings/weekends back to spend more time with you, HR, Lucky and Ollie.

CONTENTS

Abstract 2

Acknowledgements 3

List of Figures 11

List of Tables 19

1 Introduction 21

1.1 Fluorescence microscopy 21

1.1.1 Background 21

1.1.2 Limits of Resolution 22

1.1.3 Total Internal Reflection Fluorescence and Highly Inclined and Laminated Optical Sheet 26

1.1.4 Surpassing the resolution limit 28

1.1.5 Structured illumination microscopy 32

1.1.6 Solid Immersion Lens in Life Sciences 35

1.2 An Introduction to *Rhodobacter sphaeroides* 39

1.3 FtsZ 40

1.4 MipZ and FtsZ regulation in Alphaproteobacteria 43

1.5 Research Motivation 47

2 Materials and Methods 49

2.1 Growth Conditions 49

2.1.1 *R. sphaeroides* 49

2.1.2 *E. coli* 49

2.1.3 Strains 50
2.1.4 Plasmids 50
2.2 Cloning and DNA Analysis Methods 50
2.2.1 Polymerase Chain Reaction 50
2.2.2 DNA and PCR Product Purification 52
2.2.3 Gibson Assembly 52
2.2.4 Site Directed Mutagenesis 53
2.2.5 Transformation 53
2.2.6 Conjugation 54
2.2.7 Homologous Recombination 55
2.2.8 DNA Analysis by Gel Electrophoresis 56
2.2.9 DNA Sequencing 56
2.3 Protein Analysis Methods 57
2.3.1 Sodium Dodecyl Sulphate and Polyacrylamide Gel Electrophoresis 57
2.3.2 Western Blot 58
2.3.3 In-gel Fluorescence 59
2.3.4 Liquid Chromatography with tandem mass spectrometry 59
3 Observing the behaviour of FtsZ and MipZ 60
3.1 Introduction 60
3.2 Materials and Methods 61
3.2.1 Growth for microscopy 61
3.2.2 Labelling techniques 62

3.2.3 Sample mounting 63
3.2.4 Imaging protocol 63
3.2.5 Image analysis 64
3.2.6 Control experiments 65
3.3 Results 68
3.3.1 Dual Colour Imaging of MipZ and FtsZ 68
3.3.2 SNAP-tag Ligand Binding to Native *R. sphaeroides* Protein 69
3.3.3 Single colour imaging 72
3.3.4 Kymograph analysis of FtsZ data 75
3.3.5 MipZ Imaging 79
3.4 Discussion 81
3.4.1 Snap-tag labelling 81
3.4.2 Labelling Efficiencies 82
3.4.3 Imaging modality 82
3.4.4 FtsZ Dynamics 83
3.4.5 MipZ Observations 84
4 *In vitro* experiments 86
4.1 Introduction 86
4.2 Materials and Methods 87
4.2.1 Buffers for protein purification 87
4.2.2 Protein Expression Strains 87
4.2.3 Protein Expression and lysis 88

4.2.4 Protein Purification 88
4.2.5 TEV Cleavage 89
4.2.6 Sedimentation Assay 90
4.3 Results 91
4.3.1 Purification issues with FtsZ 91
4.3.2 Sedimentation Assays of MipZ and FtsZ 94
4.4 Discussion 98
4.4.1 Double FtsZ band 98
4.4.2 Reflections and further work 98
5 Microscope building 100
5.1 Introduction 100
5.1.1 Objective 100
5.1.2 Structured Illumination Microscopy Theory Overview 101
5.1.3 Solid Immersion Lens Theory Overview 104
5.1.4 Total Internal Reflection Fluorescence with SIM/SIL 107
5.2 Apparatus 107
5.2.1 Spatial Light Modulator Selection 108
5.2.2 SIL Selection 109
5.2.3 Pairing conventional objective with solid immersion lens 110
5.3 Incoherent SIM development 112
5.3.1 Incoherent SIM 112
5.3.2 Optical Design 113

5.3.3 Decision to move to a coherent design 115
5.4 Coherent SIM Development 116
5.4.1 Optomechanics 120
5.4.2 Light Source 121
5.4.3 DMD and Blaze angle 122
5.4.4 Structured Illumination magnification 125
5.4.5 Spatial filtering 126
5.4.6 Illumination Polarisation 127
5.4.7 Dichroic Mirrors 128
5.4.8 Detector and magnification 132
5.4.9 Emission Filter 133
5.4.10 Beam Expander 134
5.5 ASIL Integration 135
5.5.1 SIL Mounting 135
5.5.2 Aligning the ASIL 138
5.6 System Verification 140
5.6.1 Alignment verification 140
5.6.2 Magnification verification 141
5.7 Discussion 143
5.7.1 Future approach to addressing issues encountered using fluorescence 144
5.7.2 Further system quantification 144
5.7.3 Further Development 145

5.7.4 Sample Testing 146
5.7.5 Multicolour microscopy 147
5.8 Conclusions 147
6 Conclusions and Future Directions 149
6.1 Conclusions 149
6.1.1 Applying SIM/SIL to imaging FtsZ and MipZ in *R. sphaeroides* 149
6.1.2 FtsZ and MipZ in *R. sphaeroides* 150
6.2 Future Directions 150
7 Appendix 153
7.1 Buffers and Media 153
7.2 List of Primers 157
7.3 Histrap FF Elution Protocol 158
7.4 Size Exclusion Chromatography Protocol 164
7.5 Image overlay code 171
7.6 Kymograph Builder code 172
7.7 Kymograph Analysis Code 173
8 References 175

LIST OF FIGURES

Figure 1 – Diagram illustrating the relationship between the half angle of light acceptance α, aperture diameter D, and focal length f. a) Lens with a long focal length with a low value for α. b) Lens with a reduced focal length, increasing the value of α. 24

Figure 2 – Effect of immersion medium refractive index on objective NA. In a) the sample and immersion medium refractive indices are well matched resulting in low refraction of rays. In b) where the immersion medium refractive index is much lower than that of the sample, rays are refracted away from the objective, reducing the emission angles captured. 25

Figure 3 – Chinese hat shaped OTF and its effect on different frequency (low-high, left-right) information in the sample. Credit: Sanderson, 2019 26

Figure 4 – Moiré fringes are formed when high frequencies in a sample are illuminated with a characterised high frequency illumination pattern. Crucially, these fringes are a lower frequency and therefore are more likely to be within the bandwidth of the microscope. Changing the orientation or translating orthogonally to the angle of the illumination stripes (changing the phase) changes the Moiré fringes formed. Image credit: (Vangindertael et al., 2018)..... 33

Figure 5 – a) Hemispherical SIL (HSIL) and b) the hyper-hemispherical Aplanatic SIL (ASIL), both with a refractive index of n_{SIL}, a light collection half angle of α and a conventional objective underneath. 35

Figure 6 – The first widefield HSIL system for fluorescence imaging. Image credit (Wu et al., 1999). 37

Figure 7 – Schematic of SIM-SIL design described by Wang. Image credit: (Wang, 2010)..... 38

Figure 8- Current model the of the divisome in E. coli. Core proteins are depicted in a), non-core protein are depicted in b). The Inner Membrane (IM), Outer Membrane (OM), old peptidoglycan

(orange) and new peptidoglycan (green) are shown in the periplasm. Image credit: (McQuillen and Xiao, 2020). 41

Figure 9 – The MinCD system, including the oscillating MinE ring which controls the location of MinD, which in turn controls the locations of MinC. Absence of high concentrations of MinC at mid-cell allows polymerisation of FtsZ. Image credit: (Lutkenhaus, 2007) 44

Figure 10 – Phylogenetic tree showing MipZ and Min systems. Image credit: (Toro-Nahuelpan et al., 2019)..... 45

Figure 11- Dynamics of the ParB1-parS1 complex, MipZ(1), FtsZ and MipZ2 (M. gryphiswaldense only) across the 3 species previously studied. Adapted from: (Dubarry et al., 2019) 47

Figure 12 – Section of pk18mobsacb with insert and 500bp homologous regions interrupting lacZα..... 55

Figure 13 – Image of R. sphaeroides with line overlays along the length (a) and the fluorescence (b) of the cell 64

Figure 14 - Comparison of R. sphaeroides cell lengths of 45 cells of each mutant, SM0020, SM0050 and the wild type WS8N + pIND. Boxes indicate interquartile range with median, whilst whiskers indicate 1.5x interquartile range..... 66

Figure 15 – OD_{700} of the three strains of R. sphaeroides used in this experiment over time. Readings are relative to the starting OD of the lowest reading on the plate. This was used in place of a blank due to some suspected contamination. 67

Figure 16 – In-gel fluorescence results. a) In-gel fluorescence of SM0022 with Halo-tag labelled FtsZ and SNAP-tag labelled MipZ. b) Graph of emission spectra for JF646 and JF669, corrected for excitation efficiency at 635nm, and the quantum yield and excitation coefficient of each dye (Lambert, 2019)..... 68

Figure 17 - Examples of JF669 dye distributed across the cell, which was not expected behaviour for MipZ. 69

Figure 18 - In-gel fluorescence image of SM0022 and WS8N+pINDlabelled with JF669-SNAP. 70

Figure 19 - Structure of SNAP-tag protein with corresponding ligand bound at the active cysteine highlighted in purple. PDB ID: 6Y8P (Berman et al., 2000; Sehnal et al., 2021; Wilhelm et al., 2021) 71

Figure 20 - AlphaFold predictions of Methylated-DNA--protein-cysteine S-methyltransferase structures from both F. johnsoniae (left) and WS8N (right) where the active Cysteine binding site has been highlighted in red. Both models are predicted with a reasonably high degree of confidence as shown by the high predicted local distance difference test (pLDDT) where a maximum score of 100, predicts the highest confidence in the location of that amino acid..... 72

Figure 21 – a) HILO image of SM0022 where a < 2 µm showing FtsZ moving across the mid-cell region highlighted by the white arrow. Scale bar 1 µm; blue dotted line is measured length. b) HILO image of SM0022 where a > 2.5 µm showing stationary FtsZ location. Scale bar 1 µm; blue dotted line is measured length. c) Proportion of cells with fluorescence at the septum where FtsZ exhibits dynamic behaviour for each the three cell classes..... 74

Figure 22 - Kymographs from R. sphaeroides cells under 2 µm in length with dynamic FtsZ. Centroid at each line marked and connected in yellow. Length: 240 seconds, Scale bar: 500µm 76

Figure 23 - Kymographs from R. sphaeroides cells between 2 and 2.5 µm in length with dynamic FtsZ. Centroid at each line marked and connected in yellow. Length: 240 seconds, Scale bar: 500µm 77

Figure 24 – Velocity profiles of dynamic FtsZ across kymographs in Figure 22 a-g. Boxes indicate interquartile range, with median whilst whiskers indicate 1.5x interquartile range..... 78

Figure 25 - Velocity profiles of dynamic FtsZ across kymographs in Figure 23 a-d. Boxes indicate interquartile range, with median whilst whiskers indicate 1.5x interquartile range. 78

Figure 26 – MipZ imaging of R. sphaeroides. a) HILO images of SM0050 showing highly dynamic MipZ forming foci at both poles and at mid-cell at different time points, along with the average intensity t-projection showing the foci preset in all 3 locations. The right most image highlights the Regions of Interest (RoI's) analysed in (b) with a threshold of >3.35 % to highlight the foci locations. b) Intensity at top pole, bottom pole, and mid-cell relative to the average of all three at each time point. c) Boxplot with jitter of the lengths of 113 cells with foci at both poles only, both poles and mid-cell and mid-cell only. Boxes indicate interquartile range, with median whilst whiskers indicate 1.5x interquartile range. 80

Figure 27 – Start of 6xhis-TEV-FtsZ Amino Acid Sequence. Created using: SnapGene software (www.snapgene.com) 89

Figure 28 – a) SDS-PAGE gel and b) Western blot using α 6xHis tag (MA1-21315, Invitrogen) of 6xHis-TEV-FtsZ following elution from Ni affinity column. FtsZ highlightd by red box. Ladder: Dual Colour 1kB ladder, BioRad. 91

Figure 29 – Sequence of 6x His-TEV-FtsZ with the section identified as missing highlighted in red 92

Figure 30 – SDS-page gels with FtsZ highlighted in red box showing: a) SM0021 and SM0015 strains grown under different conditions. OD is the OD_{600} value at which the cells were induced, 3h / ON indicates whether the culture was induced for 3 hours or overnight, and the temperature indicates the temperature the cells were induced at. b) Supernatant and pellet samples from SM0021 lysis using different lysis buffer conditions. c) Result of full preparation before and after TEV cleavage. Ladder: Dual Colour 1kB ladder, BioRad. 93

Figure 31 - a) and b): Repeats of the SDS-PAGE gel from the sedimentation assays detailed in 96

Figure 32 - a) SDS-PAGE gel with suspected MipZ bands highlighted in red and bands sent for LC-MS-MS analysis in blue. b) Western blot using α 6xHis tag (MA1-21315, Invitrogen) of MipZ-6xHis. Ladder: Dual Colour 1kB ladder, BioRad. 97

Figure 33 - High frequency (red) and low frequency (green) signals present in the sample are imaged by the microscope optical system, represented by the PSF in the spatial domain and the OTF in the Fourier domain. The signals are convolved and multiplied by the PSF and OTF respectively to give the imaged output. Only the low frequency signal is within the bandwidth of the microscope and is therefore visible in the output image. However, the remaining signal is at a reduced amplitude. 101

Figure 34 – a) Convolution in the Fourier domain of signal Sk and structured illumination Ik, demonstrating how the signal is modulated into the microscope bandwidth indicated by the dotted black lines. b) Bandwidth of the microscope in two dimensions indicated by the blue circle, and 2D Fourier transform of the illumination pattern shown by 3 purple dots. c) Through the use of structured illumination, phase shifting the pattern at least 3 times, and reassigning the information captured, twice the bandwidth can be captured in one dimension. d) By rotating the structured illumination pattern by 120° and 240°, the resolution enhancement can be achieved in all directions. 103

Figure 35 - a) Hemispherical SIL where d, diameter along optical axis, is the equal to the radius r and b) Aplanatic SIL where d is a function of r and SIL refractive index, n. 106

Figure 36 – Illumination profile in Z of a bacterial sample on a zirconium ASIL, with an illumination wavelength of 636 nm and illumination angle of 66°, simulated using 107

Figure 37 - Diagram showing the optical configuration of the ASIL with radius r, and the conventional objective with working distance W.D. $_{conv}$. Samples are placed on the truncated surface of the ASIL at the Object Plane which creates a virtual image at the Image Plane, at a distance of r(n+1) from the curved surface of the ASIL, where n is the refractive index of the ASIL. 111

Figure 38 - Optical layout of incoherent structured illumination microscopy design..... 114

Figure 39 - Optical transfer function at different degrees of coherence. Image Credit: (TelescopeOptics.net, 2006)..... 116

Figure 40 – Diagram of the coherent structured illumination microscopy optical layout. Key conjugate sample planes and conjugate back focal planes have been identified with spots and circles, respectively. 117

Figure 41 – Images of the coherent SIM illumination path. a) Illumination path from laser to L3 with beam path superimposed (L1 and L2 not shown) b) Custom bracket to support DMD at 45° with tip/tilt stage.. c) diffraction pattern from DMD, with high orders blocked by the iris and fundamental blocked by the mask. d) Illumination path from PP to objective with the beam path superimposed..... 119

Figure 42 - Periscope section of the system without stage. Stage mounting shown in inset. ... 121

Figure 43 – Experiment to optimise the illumination angle of the DMD. a) Aligning the DMD with the 0° line. b) Experimental set-up showing the goniometer which revolved the laser around the centre of the DMD so the power of diffraction orders could be measured. c) Results of the experiment, showing the intensity of M is maximised at 39°. Protractor image obtained from and https://maths.prideaux.id.au/ on 29-12-2023..... 124

Figure 44 - Mask or Fourier filter to block the 0th diffraction order. (Designed and rendered in Solid Edge, Siemens). 127

Figure 45 - Diagram of pizza polariser with arrows showing direction of polarisation..... 128

Figure 46- Dichroic spectra shown in grey with spectral position of the laser line marked in orange, and the excitation and emission spectra of JF646 shown in yellow and blue respectively. Plot generated using FPBase (Lambert, 2019). 129

Figure 47 – Demonstration of depolarisation resulting from 0 dichroic mirrors (a), 1 horizontal dichroic mirror (b), one vertical dichroic mirror (c) and 2 dichroic mirrors, one of which is

horizontal, and the other is vertical (d). The results (e) show the mean +/- standard deviation pixel value in the dark segment of the pizza polariser. n = 49,964. 131

Figure 48 – Size of DMD, laser illumination beam and usable SIL LOD at sample. Constraint on detector FoV at sample is shown..... 133

Figure 49 – a) Illustration of the design used in Wang et al., 2019 with estimated half angle of acceptance shown. b) Process for assembling an ASIL (white) into a #1.5 coverslip (blue) using a partially adhesive surface (red) to temporarily secure the SIL whilst the 2-part epoxy (green) is applied and cures. c) 1 mm (represented by red arrows) holes drilled into #1.5 coverslips using a stainless-steel drilling bit (left), an ultrasonic drill (centre), and diamond tipped drill (right). d) Photos of ASIL assembled into #1.5 coverslip taken through a microscope. e) Image of the ASIL/coverslip (edge highlighted in blue) assembly secured with magnets onto a nickel slide, making it compatible with a standard microscope stage. Purple dots are dense sub-diffraction limit fluorescent beads on and off the ASIL so both could be imaged without changing set-up. 137

Figure 50 - Transillumination images of the ASIL during alignment: a) Locating the ASIL out of focus, b) finding the centre of the curved ASIL surface, c) focussed onto the flat ASIL surface. Scratches are a result of ASIL manufacturing processes. NOTE: The magnification in b) is not uniform across the image due to the focal plane being inside the ASIL, therefore no scale bar is shown. 139

Figure 51 – a) Image of apparatus to test the alignment of diffraction orders with the resulting image as inset, which shows that all 6 1st order beams are blocked by the iris at the same point. b) 3 diffraction orders labelled with their power as measured just above the iris. 140

Figure 52 – Pattern magnification verification (without the ASIL) test with a 12-pixel period pattern at the DMD. a) Image at conjugate sample plane between D1 and D2 to test magnification of first 4f system and spatial filtering. b) FFT of (a) generated in ImageJ. c) Intensity profile of yellow line in (a). d) Image at main detector with pixel size set for the image plane where a mirror

has been placed to reflect the excitation beam. e) FFT of (d) showing. The theoretical system bandwidth is shown in yellow. 142

Figure 53 - Pattern magnification verification (without the ASIL) test results using patterns generated with a 12-pixel period pattern at the DMD. a) Image from the system detector from fluorescence. b) FFT of (a). 143

Figure 54 – Architecture of the proposed microscope control system, adapted from Sandmeyer et al., (2019). 146

LIST OF TABLES

Table 1 - Summary of common immersion medium refractive indices. 24

Table 2 - Strains used in this research. 50

Table 3 - Plasmids used in this research 50

Table 4 - Thermocycler program for Q5 polymerase reactions. 51

Table 5 - Thermocycler program for OneTaq polymerase reactions 52

Table 6 - Buffer components for TBF I and TBF II, used in making cells chemically competent. 54

Table 7 – TAE Buffer 56

Table 8 – Sequencing primers 57

Table 9 – SDS PAGE materials 57

Table 10 – Amino acid alignment of the section surrounding the active site (purple) in SNAP-tag protein against sections of Methylated-DNA--protein-cysteine S-methyltransferase in WS8N, F. johnsoniae and E. coli. 72

Table 11 – Summary of strain information 88

Table 12 - Sedimentation Assays plan. 95

Table 13 – DMD properties 109

Table 14 – Properties of combined SIL objective 112

Table 15 – Laser properties 121

Table 16 – Laser power measured at output 1 of the PBC at different laser intensities and attenuation. 122

Table 17 – DMD Illumination 125

Table 18 – Structured illumination system properties..... 126

Table 19 – ZWO ASI 294MC-Pro Key Camera Specifications 132

Table 20 - M22 Media 153

Table 21 - 1M Phosphate buffer 153

Table 22 - Concentrated Base 153

Table 23 - Metals 44 Solution 154

Table 24 - Growth Factor 154

Table 25 - LB / LB Agar 154

Table 26 - Succinate Media (Sux) 154

Table 27 - FtsZ Buffer 154

Table 28 - FtsZ Lysis Buffer 155

Table 29 - FtsZ Elution Buffer 155

Table 30 - MipZ Buffer 155

Table 31 - MipZ Lysis Buffer 155

Table 32 - MipZ Elution Buffer 155

Table 33 - MipZ Storage Buffer 155

Table 34 - Antibiotics 156

Table 35 - List of primers used in this study. 157

1 INTRODUCTION

1.1 FLUORESCENCE MICROSCOPY

1.1.1 Background

Robert Hooke and Anthonie van Leeuwenhoek are considered the pioneers when it comes to the invention of the microscope, with Hooke developing a two-lens compound microscope, and Van Leeuwenhoek developing a single lens system. Hooke published the first depiction of a microorganism, the fungus *Mucor*, in 1665, while Van Leeuwenhoek later described bacteria. It was not until around 150 years later that the microscope took off as the pivotal tool in helping scientists to understand the role of microbes in disease and ecology (Gest, 2004).

Meanwhile, the discovery of fluorescence in 19th century was first properly examined by George Gabriel Stokes, who observed that when a fluorescent material is illuminated using light of a certain wavelength, the emitted light will have a longer wavelength (Stokes, 1852). This wavelength difference later became known as the 'Stokes Shift'. It is this property which allows for the separation of light originating from fluorescent molecules in the sample, and light originating from the illumination source which has been scattered or reflected by the sample. Because of this property, fluorescence microscopy is capable of high contrast and specificity.

Microscopes for fluorescence microscopy had two major advances with the development of the epi-fluorescence microscope in 1929 by Philipp Ellinger and August Hirt. Using an epi-fluorescence set-up, both the excitation and emission light pass through the objective, leading to more efficient excitation. While these earlier systems used filters to remove most of the excitation light, in 1967 Johan Sebastiaan Ploem described a system where dichroic mirrors were used to perform this role, which simplified the design greatly, and ultimately led to the epi-fluorescence microscope becoming a universal tool in science (Rusk, 2009).

Fluorescently labelling a sample and imaging it with a microscope was achieved in the 1920s by Max Haitinger, but the two major advances in fluorescent labelling came with development of immunofluorescence staining in 1941 (Coons, Creech and Jones, 1941). Here, antibodies are used to bind dye molecules to specific proteins. Another advancement took place in 1994, with the development of fluorescent proteins such as Green Fluorescent Protein (GFP) (Chalfie *et al.*, 1994) which allowed researchers to genetically engineer fluorescent labels inside the cell being studied (Diaspro, 2011).

1.1.2 Limits of Resolution

Microscope resolution is defined as the distance at which two objectives have to be spaced by to be identified as two separate objects. The fundamental factor limiting resolution in a microscope is the diffraction caused by the microscope optics. This diffraction takes the form of an Airy disk, which consists of a bright spot surrounded by rings. An Airy disk takes the same basic shape for any optical system; however, the width varies as a function of the system. For an aberration-free system, this is the Point Spread Function (PSF), and it is the convolution of this function with the sample which produces the image. The first bright ring in the Airy disk is always 1.75% of the peak value, while the radius of the first dark ring is defined by the equation:

$$r_0 = \frac{0.61\lambda}{NA}$$

Equation 1 (Guenther and Steel, 2018)

Where λ is the wavelength of light, and NA is the Numerical Aperture of the objective lens defined by the equation:

$$NA = n \sin \alpha$$

Equation 2 (Sanderson, 2019)

Where n is the refractive index of the immersion medium and α is the half angle of light acceptance. Equation 1 is known as the Rayleigh criterion (Rayleigh, 1879) and is one of two common definitions of microscope lateral resolution. This is because at this distance, the centre of one Airy disc is above the first minimum and is therefore just resolvable.

The other definition for microscope resolution is the Abbe limit (Abbe, 1873):

$$d = \frac{\lambda}{2NA}$$ *Equation 3* (Sanderson, 2019)

Whilst the Rayleigh limit is defined by the PSF, the Abbe limit is defined by the cut-off frequency of PSF's Fourier transform, the Optical Transfer Function (OTF). This means that the Abbe limit is the smallest period at the sample plane which can be detected in the image. Whilst there are slight differences between the formulas, it is clear that microscope resolution is determined by the wavelength of light and the Numerical Aperture (NA), encompassing the refractive index of the immersion medium and the half angle of light acceptance. Therefore, if one optimises these three factors, the resolution of a microscope can be increased.

First, regarding the factor of wavelength, as shorter wavelengths diffract less, reducing the radius of each diffraction order and thus the resultant resolution is decreased, as described in Equation 1.

Second, increasing α to a value of up to 90° increases the NA and this can be achieved by increasing the diameter of the aperture (D), or reducing the focal length f, as illustrated in Figure 1. This can also be expressed by the following equation:

$$NA = n \sin \alpha \approx \frac{nD}{2f}$$ *Equation 4* (Albertazzi and Zijlstra, 2024)

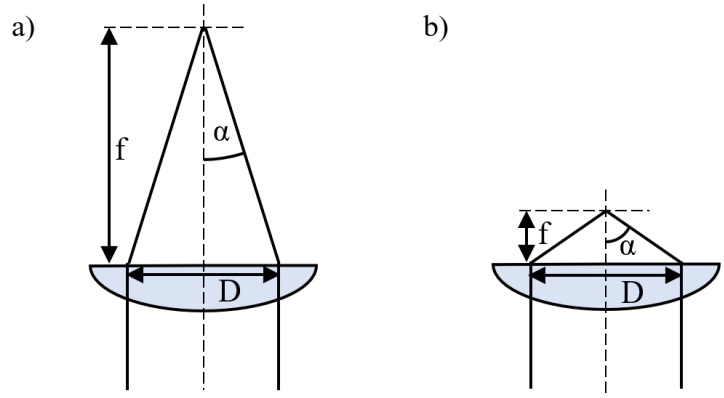


Figure 1 – Diagram illustrating the relationship between the half angle of light acceptance α, aperture diameter D, and focal length f. a) Lens with a long focal length with a low value for α. b) Lens with a reduced focal length, increasing the value of α.

Third, as the highest value for sin(α) is 1, achieved at 90 degrees, the limiting factor for the numerical aperture becomes the refractive index of the immersion medium. Standard immersion mediums are shown in Table 1:

Immersion Medium	Refractive Index
Air	1.0003
Water	1.33
Glycerol	1.47
Standard immersion oil	1.515

Table 1 - Summary of common immersion medium refractive indices.

For n_2 in Figure 2, we can consider a typical biological sample refractive index such as that of bacterial cytoplasm at 1.39 (Liu *et al.*, 2014). In Figure 2a, n_{1a} is water with an n value of 1.33, nearly identical that of n_2, and therefore the light is not refracted significantly through the immersion medium. This is not the case in Figure 2b, where air is the immersion medium in n_{1b}. In this situation, light which would have reached the objective in Figure 2a is now refracted away from the objective according the Snell's Law:

$$n_1 \sin\theta_1 = n_2 \sin\theta_2$$ *Equation 5*

(Sanderson, 2019)

Where n_1 and n_2 are the refractive indices of the immersion medium and sample respectively, θ_2 is the angle of incidence relative to the normal and θ_1 is the angle of refraction relative to the normal.

Conversely, if n_1 were an immersion oil, light would be refracted into the objective's collection cone (Abramowitz and Davidson, 2015).

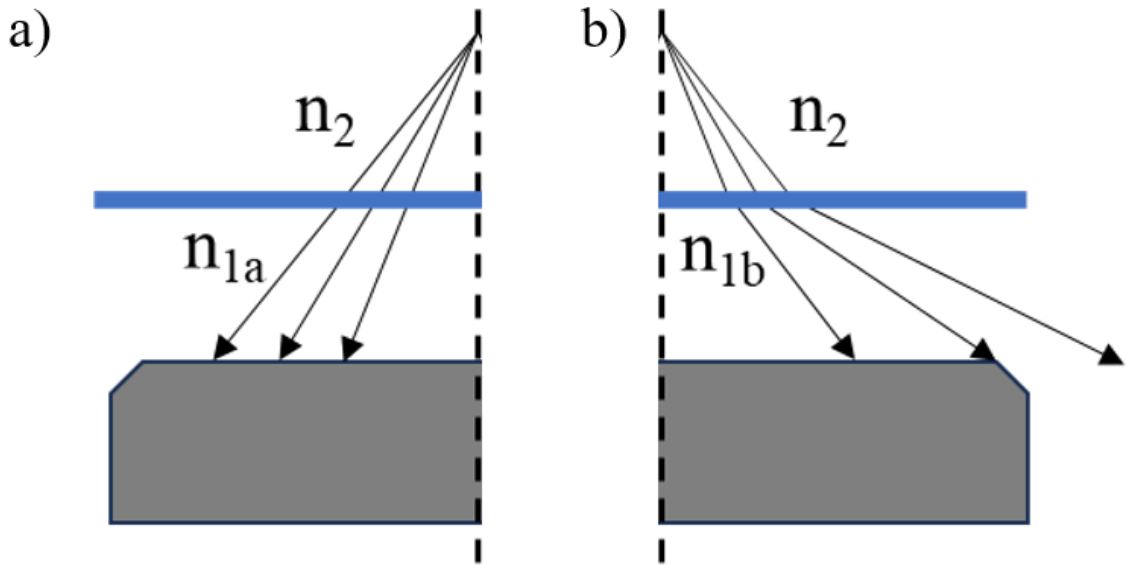


Figure 2 – Effect of immersion medium refractive index on objective NA. In a) the sample and immersion medium refractive indices are well matched resulting in low refraction of rays. In b) where the immersion medium refractive index is much lower than that of the sample, rays are refracted away from the objective, reducing the emission angles captured.

It is important to note that the PSF is not a 2D structure but a 3D one, which also relates to Abbe's formula for axial resolution:

$$d = \frac{2\lambda}{NA^2}$$ *Equation 6*

(Sanderson, 2019)

The Fast Fourier Transform of the PSF is the OTF, which characterises how the microscope maps the frequency content of the object onto the image (Sanderson, 2019). It is the OTF which defines

the bandwidth of the system, beyond which no frequency information will be captured. The effect of the OTF on different frequency components in a sample is shown in Figure 3, which depicts the general OTF for non-coherent light, which has a cut-off frequency at $2\frac{NA}{\lambda}$, as defined by the Abbe limit in Equation 3 (Period = 1/Frequency).

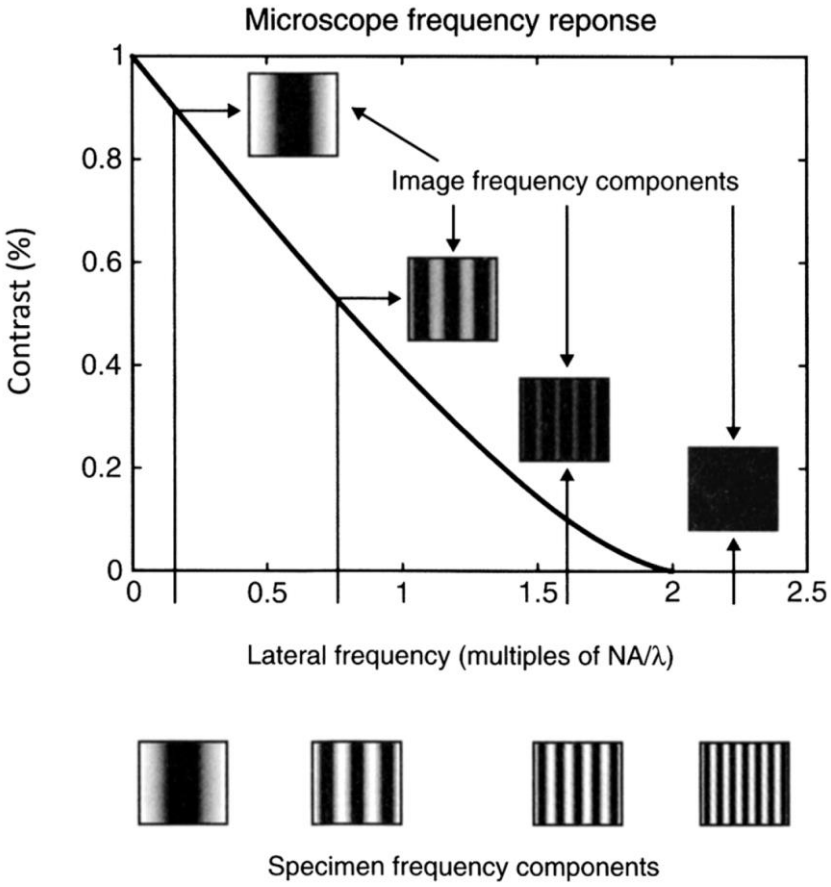


Figure 3 – Chinese hat shaped OTF and its effect on different frequency (low-high, left-right) information in the sample. Credit: Sanderson, 2019

1.1.3 Total Internal Reflection Fluorescence and Highly Inclined and Laminated Optical Sheet

Total Internal Fluorescence Microscopy (TIRF) (Axelrod, 1981) and HILO (Tokunaga, Imamoto and Sakata-Sogawa, 2008) are techniques which utilise inclined illumination of the sample to limit the illumination depth. Using TIRF limits the illumination depth to around 200nm, which reduces background fluorescence, enhancing the signal to noise ratio of the image. In TIRF, the angle at which the illumination intercepts the sample is beyond the critical angle which results in

total internal reflection. This creates an evanescent field which propagates into the sample. The critical angle is defined as:

$$\theta(c) = \mathrm{ar}csin\left(\frac{n_2}{n_1}\right)$$

Equation 7
(Sanderson, 2019)

Where n_2 is the refractive index of the sample (typically around 1.39 for bacterial cytoplasm (Liu *et al.*, 2005)) and n_1 is the refractive index of the coverslip, around 1.52.

TIRF can be achieved using a prism, but when using a high numerical aperture (NA) objective and epi-fluorescence as is the case in this work it is common to use the objective lens. The NA of the objective for TIRF must be high enough to achieve illumination at beyond the critical angle. NA is defined by the equation:

$$NA = n\,sin(\theta)$$

Equation 8
(Sanderson, 2019)

Where n is the refractive index of the glass and θ is the cone angle of the objective which also defines the maximum possible angle of illumination. Using Equation 7 with values for bacterial cytoplasm and a coverslip, we can see that the critical angle is around 60°. This means, using Equation 8, that the minimum numerical aperture required to achieve TIRF is around 1.35. As cells do not fill the field of view, the majority of the TIRF field is formed at the interface between glass and water. Since water has a lower refractive index (n=1.33) than cytoplasm, it has a lower critical angle, therefore, 60° is sufficient to form a TIRF field across the entire sample.

The illumination intensity I_z at depth z, is defined by:

$$I_z = I_0 e^{\frac{-z}{d}}$$

Equation 9
(Fish, 2022)

Where I_0 is the intensity at the glass sample interface and d is the penetration depth defined by:

$$d = \frac{\lambda_i}{4\pi} \cdot (n_1{}^2 \cdot sin^2\theta_1 - n_2{}^2)^{-\frac{1}{2}}$$

Equation 10

(Fish, 2022)

Where λ_i is the excitation wavelength, θ_1 is the illumination angle, n(2) is the refractive index of the sample and n(1) is the refractive index of the coverslip.

For imaging molecules beyond the 200nm illuminated by TIRF, HILO can be used to illuminate a greater sample depth. The signal to noise ratio of the resulting images is lower than that found in TIRF images but is better than if epi-illumination were to be used. The key difference between the two techniques is that the illumination angle used for HILO is below the critical angle required for TIRF. This means that the sample is illuminated by a "laser beam which is highly inclined by a large refraction and is laminated as a thin optical sheet at the specimen side" (Tokunaga, Imamoto and Sakata-Sogawa, 2008). The thickness of this beam, *dz*, is defined by:

$$dz = \frac{R}{tan\,\theta}$$

Equation 11

(Tokunaga, Imamoto and Sakata-Sogawa, 2008)

Where R is the diameter of the illuminated area at the specimen plane and θ is the incidence angle at the specimen.

1.1.4 Surpassing the resolution limit

Moving on to more recently developments in the field of microscopy, techniques have now been developed to circumvent the resolution limit and it is now possible to achieve a lateral resolution (or more precisely, localisation precision) of 1 nm (Masullo *et al.*, 2021).

Before covering techniques which surpass the resolution limit, it is necessary to introduce the concept of confocal microscopy to understand some of the super resolution techniques discussed below. This is a technique in which the light source is focussed into the sample, illuminating only a very small area, and therefore the light must be scanned across the sample. When combined with fluorescence techniques, the fluorescent labels excited at each of these positions emit light

which is detected by a photomultiplier tube or avalanche photon detector, rather than a Complementary Metal-Oxide-Semiconductor (CMOS) or Charge-Coupled Device (CCD) detector. Critically, a pinhole is placed in front of the detector to block out of focus fluorescence, leading to images with high signal to noise ratio and contrast (Vangindertael *et al.*, 2018).

The first super resolution techniques

Whilst applying deconvolution algorithms advanced the performance of confocal microscopes (Agard and Sedat, 1983), the first technique generally regarded as super-resolution is 4pi (Hell and Stelzer, 1992; Hell *et al.*, 1994), a confocal microscope which illuminates and collects emission from both sides of the sample using 2 objective lenses. 3 years later I^5M (Gustafsson, Agard and Sedat, 1995, 1999) was developed which is essentially a widefield version of 4pi. Both of these techniques improve the axial resolution (4 and 7 fold respectively) but do little for lateral resolution.

The first technique to improve lateral resolution was Stimulated Emission Depletion (STED) microscopy (Hell and Wichmann, 1994) which is similar to confocal system, but uses a donut shaped STED beam around the excitation beam to silence fluorophores within the diffraction limited region, and has been shown to provide a resolution of 20 nm (Göttfert *et al.*, 2013). The main disadvantage of STED is the very high illumination intensities that are required, which have limited the use of STED in many applications (Vicidomini, Bianchini and Diaspro, 2018).

Structured Illumination Microscopy (SIM) (Heintzmann and Cremer, 1999; M. G. Gustafsson, 2000) is also considered one of the original super-resolution techniques and remains popular, as it can be applied to samples which use standard fluorescent labels and is typically equipped with multicolour excitation/detection, facilitating more complex studies (Heintzmann and Huser, 2017). In the context of this work, SIM should be read as super resolution SIM, and not the older technique by the same name which can be used for optical sectioning (Neil, Juškaitis and Wilson, 1997). SIM will be described in more detail in section 1.1.5.

The final techniques which are part of the original super resolution methods are Photoactivated Localisation Microscopy (PALM or fPALM) (Betzig *et al.*, 2006; Hess, Girirajan and Mason, 2006) and Stochastic Optical Reconstruction Microscopy (STORM or dSTORM) (Rust, Bates and Zhuang, 2006; Heilemann *et al.*, 2008). Together, these methods are known as Single Molecule Localisation Microscopy (SMLM) (Betzig, 1995) and work by switching off the majority of fluorophores, so that fluorescence from single emitters can be imaged. In the case of PALM, this is done by using UV illumination to switch "on" a number of fluorophores, which are then imaged and bleached by the excitation source. For dSTORM, UV illumination causes stochastic blinking of dye molecules, which are excited by the excitation source and imaged. The diffraction limited spots in each recorded frame can then be fitted, to accurately calculate the location of the fluorophore to a precision of around 20 nm. By repeating this process over many frames with different fluorophores illuminated, the list of locations can be plotted to create a super-resolution representation of the sample.

Since conception, SMLM has been adapted for 3D localisation using an array of different techniques to determine how far molecules are from the focal plane and in which direction. The astigmatism approach (Huang *et al.*, 2008) uses a cylindrical lens in the detection path to induce astigmatism into the image. This means that for each localisation, the PSF will be stretched in one direction proportionally to the distance of the molecule below the focal plane, and will be stretched orthogonally by the same amount for a molecule the same distance above the focal plane. Bifocal plane detection (Juette *et al.*, 2008) works by splitting the detection path in two and projecting onto the detector using two different path lengths in a way that results in a molecule on the focal plane being equally out of focus in both images. The relative widths of a molecule's PSF in these images determines how far away from the focal plane it is and in which direction. Finally, double helix point spread function (Backlund *et al.*, 2013) uses a phase plate mask in the detection path which results in every molecule being represented by two spots in the image. The centre of these is the X, Y position, and their relative angle can be used to quantify z position.

Single Particle Tracking (SPT) (Barak and Webb, 1982) is a technique which facilitates the quantification of diffusion rates and trajectories of molecules by monitoring their position in each frame. Whilst SPT existed long before the SMLM was created, PALM has been used extensively with SPT (Manley *et al.*, 2008). Tracking techniques work by recording the position of a molecule in one image, and then identifying that same molecule in the next image and recording its position. In a data set with few visible molecules, assigning a molecule to a localisation in each frame can be done using a nearest neighbour method where a molecule is assigned to a localisation in the first image. Then in the second image, it is assigned to the localisation closest to its position the first image. For more crowded data sets, more complex globally optimised assignment can be used (Olivo-Marin, 2002). The mean squared diffusion can then be calculated using the position of the molecule in each frame and the equation:

$$\langle r^2(n)\rangle_A = \frac{1}{N_A}\sum_{i=0}^{N_A-1}[\vec{r}(i+n) - \vec{r}(i)]^2 \qquad \textit{Equation 12 (Saxton, 1997)}$$

Where N_A is the number of trajectories $\overrightarrow{r(t)}$ being analysed and n is the time between frames measured in units of δt.

Since the invention of these original methods, countless others have evolved from them, with further enhancements to lateral, axial and temporal resolution as well as improvements to biological compatibility. A STED-like donut beam and structured illumination patterns are being used in MINFLUX (Balzarotti *et al.*, 2017) and SIMFLUX (Cnossen *et al.*, 2020) respectively to achieve resolution below 10 nm. In both of these methods, the location of the fluorophore is calculated using several images utilising different forms of spatially modulated illumination. In MINFLUX, a donut shaped excitation beam is scanned across the sample. Because of the donut shape, the minimum fluorescence will occur when the donut is centred over the fluorophore, and because the centre of the donut is controlled by the scanning system, it can be very precisely known. By measuring the fluorescence intensity with the beam slightly off-centre from the fluorophore at three points, the position of the fluorophore can be calculated to within 1nm.

SIMFLUX uses a sinusoidal excitation pattern similar to that used in structed illumination microscopy. By measuring the fluorescence intensity of a molecule over 3 phase shifts in two orthogonal orientations, it's location can be calculated with twice the precision of standard localisation techniques.

Super-Resolution Radial Fluctuations (SRRF) (Culley et al., 2018) is a purely analytical single molecule method to break the diffraction barrier, which can be used with any fluorescent protein. Here, each pixel is split up into sub-pixels and the probability that it contains a fluorophore is calculated for each of them. This probability calculated by assessing the sub-pixel against two properties of an imaged fluorophore, its radially symmetry, arising from the radially symmetric PSF of the microscope, and temporal correlation in this radial symmetry over time. Using this technique it is possible to achieve 70nm spatial resolution on a densely labelled sample using non-blinking fluorophores.

1.1.5 Structured illumination microscopy

The concept of structured illumination microscopy was first proposed by Heintzmann and Cremer in 1999 as 'Laterally modulated excitation microscopy', providing a lateral resolution improvement which was then further developed and quantified as a two-fold resolution improvement a year later by Gustafsson, Agard and Sedat. The basic concept was to laterally modulate the illumination which expanded the range of measureable spatial feqeuencies. This is because of the Moiré fringes, which are formed when a sample containing high frequency content is illuminated with a high frequency pattern Figure 4. As these fringes are of lower frequency than the original information, they are more likely to fall into the bandwidth of the imaging system. If the illumination patern is well characterised, then this information, along with images from different illumination pattern phases, can be used to construct an image of the original sample.

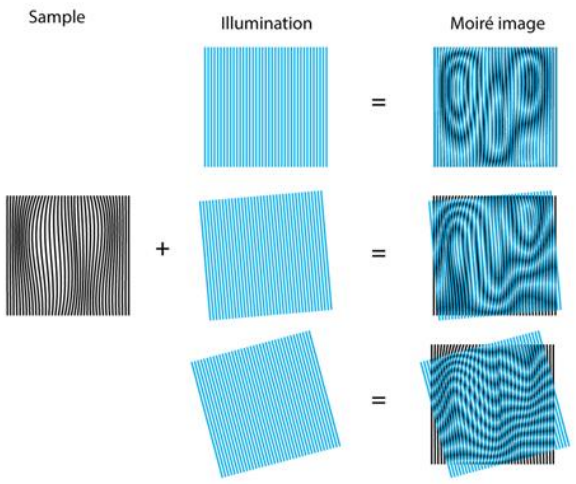


Figure 4 – Moiré fringes are formed when high frequencies in a sample are illuminated with a characterised high frequency illumination pattern. Crucially, these fringes are a lower frequency and therefore are more likely to be within the bandwidth of the microscope. Changing the orientation or translating orthogonally to the angle of the illumination stripes (changing the phase) changes the Moiré fringes formed. Image credit: (Vangindertael et al., 2018)

The system developed by Gustafson *et al.* (2000) used a phase grating to generate diffraction orders, of which all but the K_1 and K_{-1}orders were blocked, creating a sinusoidal striped pattern at the sample. 3 phase shifts and 3 angles were used to create one SIM frame, with the translation and rotation of the grating performed using translation and rotation stages. A linear polariser was mounted to the same rotation stage to ensure that the polarisation angle was maintained for all orientations (M. G. Gustafsson, 2000).

Since this publication, SIM has continued its development and there are now lots of variations on this original design. For instance, Chung *et al.* described a version of SIM applied to Total Internal Reflection Fluorescence (TIRF) illumination, meaning that the structured illumination was confined to near the coverslip (Chung, Kim and So, 2006; Kner *et al.*, 2009).

Whereas the publications mentioned so far all used 2-beam interference to generate their structured illumination, enhanced axial resolution could be achieved through 3 (Gustafsson *et al.*, 2008) or 4 (Fedosseev *et al.*, 2005) beam interference, or by combining SIM with I^5M (Shao *et al.*, 2008).

Improvements to the lateral resolution of SIM have also been made by exploiting non-linearities in the relationship between excitation intensity and emission intensity in the fluorophores saturated state (Gustafsson, 2005). Whilst the harmonics generated enhanced the detectable k-space to facilitate <50 nm resolution, the time taken to capture the necessary number of frames means that motion artifacts become a problem, and the high illumination intensity can cause rapid photobleaching and phototoxicity. To get around this problem, photoswitchable fluorescent proteins were employed, where the non-linearity in the switching behaviour could be exploited (Rego *et al.*, 2012; Lu-Walther *et al.*, 2016). 2-photon illumination, which is intrinsically non-linear, has also been used (Cheng *et al.*, 2014). The lack of photoswitchable fluorophores which can perform an adequate number of switching cycles has prevented more widespread adoption of nonlinear SIM.

To achieve a good SIM reconstruction, the sample must be identical in all illumination states. This is not a problem for fixed cells, but for live cell imaging, where movement of the labelled feature is likely, it means the images must be captured as quickly as possible. In early implementations, the speed was limited by the mechanical rotation and translation of the grating used to create the interference, however this was circumvented through the use of Liquid Crystal on Silicon (LCoS) spatial light modulators (Hirvonen *et al.*, 2009; Kner *et al.*, 2009; Li *et al.*, 2015), Digital Micromirror Devices (DMD) (Dan *et al.*, 2013; Shin *et al.*, 2018; Sandmeyer *et al.*, 2019) and use of an acousto-optic deflector (Gliko, Brownell and Saggau, 2009).

Despite these developments, the vast majority of SIM remains limited to two-fold resolution improvement due to the problems highlighted above, and this is substantially lower than other super-resolution techniques. Other limitations arise from the fact at least 9 images are required for each SIM frame, a problem which is amplified when several fields of view, or z-planes are required, making SIM prone to motion artifacts caused by diffusing molecules being in different locations in different frames, which prevents accurate reconstruction of the SIM frame. Due to the requirement to interfere the coherent beams at a specific location in the sample, imaging deep

in samples is another limitation of SIM, as backscatter and reflections prevent a high contrast illumination pattern being formed (Heintzmann and Huser, 2017).

1.1.6 Solid Immersion Lens in Life Sciences

As discussed earlier in this chapter, the refractive index of the immersion material is one of the key factors in determining the NA, and in turn, the resolution of the optical system. Changing a dry objective with an immersion material of air (n = 1.0003) for a water immersion objective (n = 1.33) will result in a resolution enhancement, however, to access NAs above the 1.7 currently offered by the highest commercially available objective from Olympus, a Solid Immersion Lens (SIL) is required. This is a hemispherical (Figure 5a) or hyper-hemispherical (Figure 5b) lens which replaces both the immersion oil and the coverslip meaning the sample is mounted directly on the SIL.

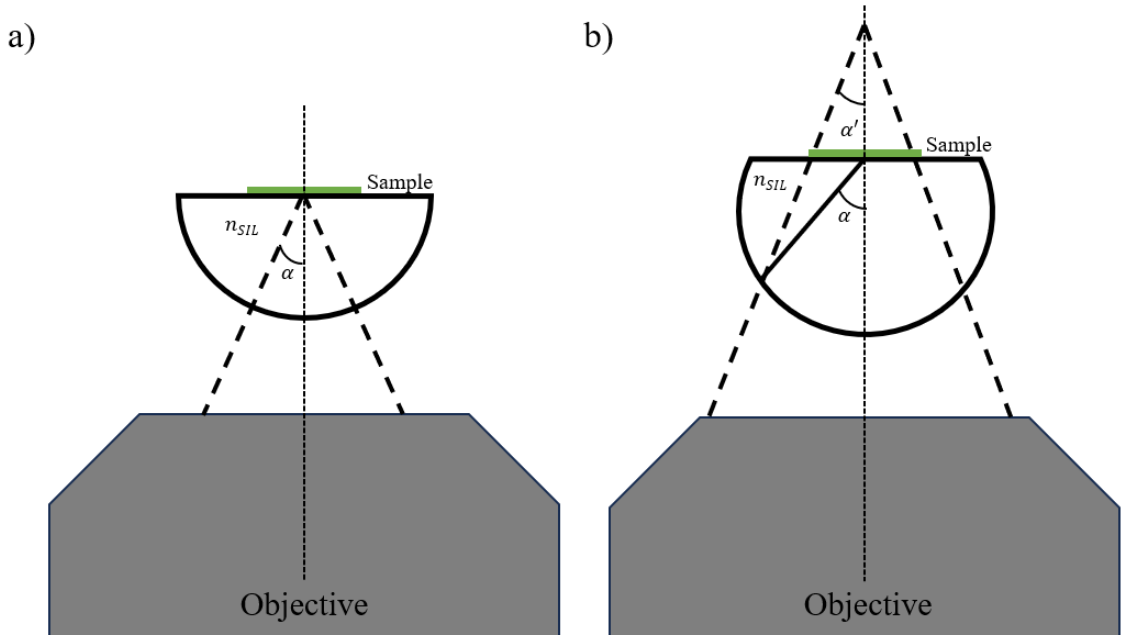


Figure 5 – a) Hemispherical SIL (HSIL) and b) the hyper-hemispherical Aplanatic SIL (ASIL), both with a refractive index of n_{SIL}, a light collection half angle of α and a conventional objective underneath.

The first type of SIL to be used in a microscope was the Hemispherical SIL (HSIL) (Mansfield and Kino, 1990). Here, the HSIL was integrated into a scanning system and used to image lines

in photoresist. This HSIL was made from n = 1.92 glass, was illuminated with a wavelength of 436 nm, and was able to image a 100 nm spaced pattern. 4 years later, the Aplanatic SIL (ASIL) had been developed and was used to write and read the domains in magneto-optic material (Terris *et al.*, 1994).

It was not until 1997 that ASIL was integrated into a widefield photoluminescent imaging system for the first time (Sasaki *et al.*, 1997) where a high refractive index glass (n = 1.8) was used to image strip lined patterns in Gallium arsenide (GaAs) quantum well structures, achieving an NA of 1.25.

In 1999 the first HSIL was integrated into a fluorescent widefield microscope (Wu *et al.*, 1999) (Figure 6), where fluorescent dye balls were used to verify a resolution performance of 139 nm. This system used a gallium phosphate HSIL (n = 3.4) and an emission wavelength of 560 nm. Later this system was used to measure the thickness of deoxyribonucleic acid (DNA) bundles, the first example of a biological sample being imaged with SIL microscope (Wu, Ghislain and Elings, 2000).

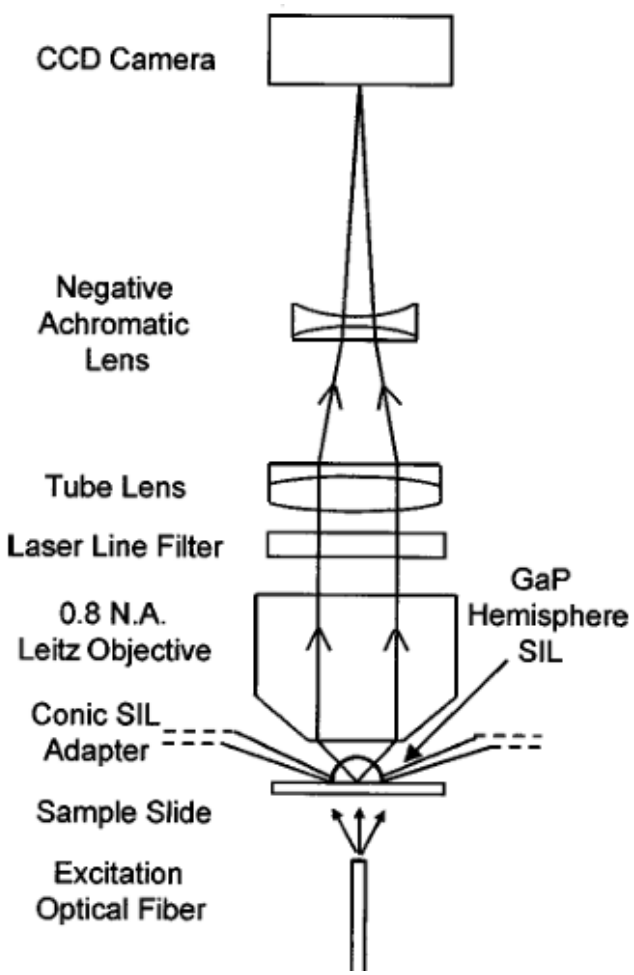


Figure 6 – The first widefield HSIL system for fluorescence imaging. Image credit (Wu *et al.*, 1999).

Following the development of HSIL and ASIL, a range of studies were conducted to look into the performance differences between HSIL and ASIL, concluding that the ASIL has a wider Field of View (FoV) and overall better resolution performance (Ippolito, Goldberg and Ünlü, 2005; Zhang, See and Somekh, 2007) (Wang, 2010). Whilst lateral resolution is important to many applications, FoV is particularly important for biological applications as the sample cannot be easily separated from the SIL surface to change the observable region, as it can be for rigid samples. An explanation why both these factors are improved for ASIL compared to HSIL is provided in 5.1.3.

The first widefield fluorescence ASIL microscope was reported in 2010, using an S-LAH79 (n = 2) (Wang, Pitter and Somekh, 2010) achieving an effective NA of 1.85 at 670 nm emission wavelength. The same research group then went on to use the ASIL with structured illumination microscopy (Wang, 2010; Wang, Pitter and Somekh, 2011a) and TIRF microscopy (Wang *et al.*, 2012). The combination of SIM with an ASIL achieved an effective NA of 3, using a lens with a refractive index of 2 on fluorescent bead samples Figure 7.

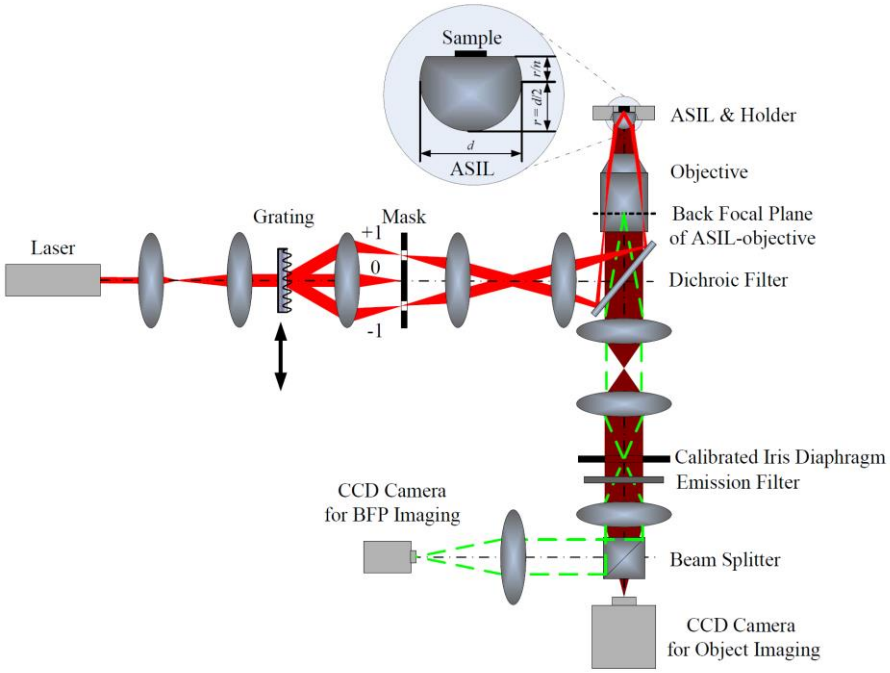


Figure 7 – Schematic of SIM-SIL design described by Wang. Image credit: (Wang, 2010).

Structured illumination is not the only super-resolution technique to be combined with SIL to further enhance resolution. STED has been combined with SIL (Wildanger *et al.*, 2012; Katayama *et al.*, 2017; Kim *et al.*, 2017) to achieve a resolution of 34 nm for a fluorescent bead sample with an ASIL, and 2.4 nm for nitrogen vacancy points in diamond, but here, the HSIL was cut into the diamond itself.

Single molecule localisation microscopy has also been combined with ASIL under cryogenic conditions (Wang *et al.*, 2019), achieving a localisation precision of 15.4 nm at room temperature and 7.7 nm at cryogenic temperatures due to the higher photon budget in the latter case. This

system was shown to be compatible with biological samples, including CHO cells expressing EGFR labelled with Alexa Fluor 488 and McjD-EGFP in *E. coli*.

Arrays of miniature SILs around 160 µm in radius (Liau *et al.*, 2015) have been combined with confocal microscopy. They demonstrated a resolution of 15 nm on both beads and fixed biological samples.

1.2 An Introduction to *Rhodobacter sphaeroides*

R. sphaeroides is a purple nonsulfur photosynthetic bacterium of the α-subclass of proteobacteria. It is often found in stagnant fresh and salt water in the form of a pinkish film (Aizawa, 2014). It is a model organism for the study of bacterial photosynthesis (Masuda and Bauer, 2002), bacteria with multipartite genomes (Suwanto and Kaplan, 1989), flagella (Armitage, 2022), and for the creation and study of novel protein expression systems (Jaschke *et al.*, 2011).

Like other α-proteobacteria, *R. sphaeroides* is metabolically diverse, able to grow aerobically, photoheterotrophically, and anaerobically in low light conditions. When switching from aerobic to photoheterotrophic growth conditions, the inner membrane becomes highly invaginated to accommodate the photosynthetic apparatus (Kiley and Kaplan, 1988). When growing aerobically, a protonmotive force (PMF) is generated by the respiratory chain and under photoheterotrophic growth conditions, *R. sphaeroides* photosynthesises using photosynthetic electron transport to generate a PMF across the inner membrane.

Under the aerobic growth conditions used in this work, *R. sphaeroides* is around 2 µm in length and 0.8 µm wide.

R. sphaeroides was the first bacteria discovered to have more than 1 chromosome (Suwanto and Kaplan, 1989) and this is the case for all *R. sphaeroides* strains, although both the size of the chromosomes and the number of plasmids present alongside them vary between strains (Nereng

and Kaplan, 1999). This is very relevant for the co-ordination of cell division as both chromosomes need to be replicated and segregated prior to division (Dubarry *et al.*, 2019).

The strain used in the experiments that were conducted as part of this thesis is WS8N (R. E. Sockett, Foster and Armitage, 1990), a spontaneous mutant conferring nalidixic acid (Nal) resistance.

Originally viewed as a strain used only for fundamental studies, a growing number of applications for *R. sphaeroides* are becoming apparent, such as bio-factories to synthesize compounds such as poly-β-hydroxybutyrate and hydrogen (Orsi *et al.*, 2021). The bacterium is also being used to detect and clean up pollution (Balsalobre *et al.*, 1993; Li *et al.*, 2017) and has been evaluated as an optoacoustic *in vivo* reporter of macrophage activity in cancer (Peters *et al.*, 2019).

1.3 FtsZ

FtsZ is a GTPase which is a highly conserved homologue of the mammalian protein tubulin (de Boer, Crossley and Rothfield, 1992; RayChaudhuri and Park, 1992; Erickson, 1995). FtsZ forms a ring at mid-cell called the z-ring and it is this which will become the future division site of the cell. The Z-ring then recruits over 30 proteins which form the divisome (Buddelmeijer and Beckwith, 2002; Goehring and Beckwith, 2005), of which 20 are involved in peptidoglycan remodelling (McQuillen and Xiao, 2020). The current model the of the divisome in *E. coli* is shown in Figure 8.

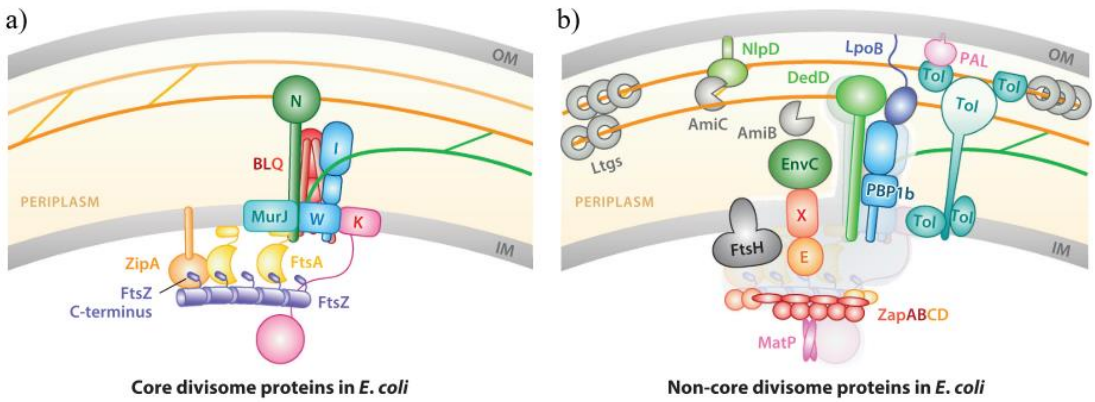


Figure 8- Current model the of the divisome in E. coli. Core proteins are depicted in a), non-core protein are depicted in b). The Inner Membrane (IM), Outer Membrane (OM), old peptidoglycan (orange) and new peptidoglycan (green) are shown in the periplasm. Image credit: (McQuillen and Xiao, 2020).

All of FtsZ's functions are performed as part of this Z-ring and it is supported by the observation that all known proteins which regulate FtsZ activity in some way, do this by promoting or preventing polymerisation. Examples of these regulatory proteins are MipZ (Thanbichler and Shapiro, 2006b), MinC (Rowlett and Margolin, 2013) and SulA (Justice, García-Lara and Rothfield, 2000).

The Z-ring is not a stolid static structure but is rather highly dynamic, formed of FtsZ filaments which have been shown to 'treadmill' both *in vivo* (Bisson-Filho *et al.*, 2017) and *in vitro* (Loose and Mitchison, 2014). This term is used to describe the process of FtsZ polymer chains moving around the circumference of the cell at mid-cell. This process is the result of GTP bound FtsZ binding to the leading edge of an FtsZ filament. Over time, the GTPase action of FtsZ causes GTP hydrolysis converting it to GDP. These GDP bound FtsZ molecules have a lower binding affinity and therefore are likely to unbind from the trailing edge of the filament. This continuous process of GTP bound FtsZ binding to the leading edge and GDP bound FtsZ unbinding from the trailing edge causes treadmilling. This behaviour has been observed in multiple species such as *E. coli*, *B. subtilis* (Bisson-Filho *et al.*, 2017), *S. aureus* (Monteiro *et al.*, 2018), *S. pneumoniae* (Perez *et al.*, 2019) and *S. mutans* (Li *et al.*, 2018). In the Alphaproteobacteria class of bacteria which

contains *R. sphaeroides* and *C. crescentus*, no-one has yet reported treadmilling behaviour by FtsZ (Lariviere and Goley, 2022), however, there is now research which assumes treadmilling behaviour in *C. crescentus* (Corrales-Guerrero *et al.*, 2022).

There has been no definitive study of FtsZ treadmilling in *R. sphaeroides* to date. However, in 2013, Chui and colleagues reported evidence that Z-rings became more dense as more FtsZ proteins joined, supporting the theory of the loose bundle model (Fu *et al.*, 2010) and they also observed the Z-ring as a heterogeneous structure with gaps (Chiu *et al.*, 2013). Whilst the 3D SIM images of the FtsZ ring in Dubarry *et al.*, (2019) show a continuous ring, this could simply be a reconstruction artifact of the time taken to perform a 3D SIM z-stack, although the ring shown does seem more complete than rings observed in comparative experiments in other bacterial species (Strauss *et al.*, 2012; Rowlett and Margolin, 2014).

Chui and colleagues also observed FtsZ spots at mid-cell in the early stages of the cell cycle, and that it is from these spots that the Z-ring develops (Chiu *et al.*, 2013). This observed behaviour is in contrast to the helical pattern of FtsZ shown to form in *E. coli* (Sun and Margolin, 1998; Tsang, Yakhnina and Bernhardt, 2017) and *B. subtilis* (Levin and Losick, 1996). Chui and colleagues suggest that this could be because the helix is simply a relaxed z-ring and the FtsZ spots observed in *R. sphaeroides* exist in all species but are more visible in *R. sphaeroides* due to the longer cell life. Another possibility is that is could be a result of differences in the regulatory systems employed in each of these species, with *B. subtilis* and *E. coli* using the Min system, and *R. sphaeroides* using the ParABS system.

Fluorescent imaging studies of FtsZ are often “met with intense scrutiny” (McQuillen and Xiao, 2020) because presently a fully functional FtsZ-Fluorescent Protein (FtsZ-FP) fusion has not yet been created. This means that copies of the labelled protein must be expressed at low levels alongside native copies, meaning there is more FtsZ present in the cell than there would be normally, on top of the fact that the labelled copies do not behave in the same way as the native variants. Research groups have created two strains with labelled FtsZ as the sole copy, and both

of these are functional in as far as they divide at a similar rate to the wild-type; however, the strain of *B. subtilis* with an FtsZ-GFP fusion (Levin, Kurtser and Grossman, 1999) was found to be temperature sensitive, and the *E. coli* strain with an FtsZ–mNeonGreen fusion (Moore *et al.*, 2017) was shown to exhibit behaviour similar to a mild FtsZ GTPase mutant (Yang *et al.*, 2017) (McQuillen and Xiao, 2020).

1.4 MipZ and FtsZ regulation in Alphaproteobacteria

MipZ is a ParA like actin homologue from the P-loop family of ATPases. Since it was first characterised by Thanbichler and Shapiro is 2006, it has been studied extensively in *Caulobacter crescentus* (Thanbichler and Shapiro, 2006b, 2006a; Kiekebusch *et al.*, 2012; Corrales-Guerrero *et al.*, 2020, 2022) as well as in *Rhodobacter sphaeroides* (Dubarry *et al.*, 2019) and *Magnetospirillum gryphiswaldense* (Toro-Nahuelpan *et al.*, 2019).

MipZ has an important role in ensuring the Z-ring forms at mid-cell; a role which it performs by interfering with FtsZ polymerisation, restricting the growth of long filaments which form its ring-like structure (Thanbichler and Shapiro, 2006b). It was recently reported that the mechanism for this in *C. crescentus* is the capping of the leading-edge C-terminal of FtsZ filaments by MipZ dimers, preventing FtsZ molecules joining. As FtsZ hydrolyses GTP and unbinds from the trailing edge, new FtsZ monomers are unable to join the leading edge because of the cap, causing disassembly (Corrales-Guerrero *et al.*, 2022).

It is crucial that MipZ performs this role in species where the MinCD system is not present. In the MinCD system, MinC is responsible for ensuring that the Z-ring forms at mid-cell by preventing polymerisation of FtsZ. It achieves this by oscillating from one pole the other, and therefore never being concentrated at mid-cell, allowing FtsZ to polymerise. MinC oscillation is driven through binding to polymers of MinD, an ATPase which forms polymers at the cell poles in an oscillatory fashion. This oscillation is driven by MinE, which causes MinD to hydrolyse ATP, depolymerise and detach from the membrane, as shown in Figure 9 (Lutkenhaus, 2007).

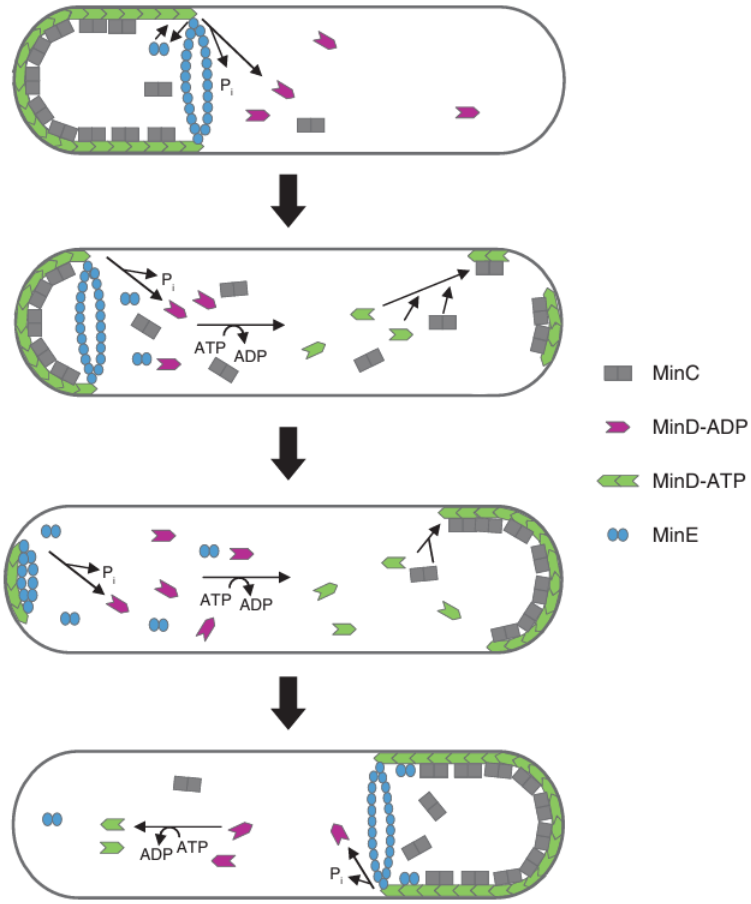


Figure 9 – The MinCD system, including the oscillating MinE ring which controls the location of MinD, which in turn controls the locations of MinC. Absence of high concentrations of MinC at mid-cell allows polymerisation of FtsZ. Image credit: (Lutkenhaus, 2007)

Most bacterial species either have a MinCD system or MipZ to ensure the Z-ring forms at mid-cell, though there are a few which have both. MinCD is present in many of the commonly studied bacteria such as *E. coli* and *B. subtilis* (although the latter lacks MinE) and is present in bacteria that branch close to the root of the phylogenetic tree (Lutkenhaus, 2007). However, in the *Rhodospirillaceae* family, of which *R. sphaeroides* (Dubarry *et al.*, 2019) and *M. gryphiswaldense* are both members, MipZ is by far most common, as can be seen in Figure 10 (Toro-Nahuelpan *et al.*, 2019).

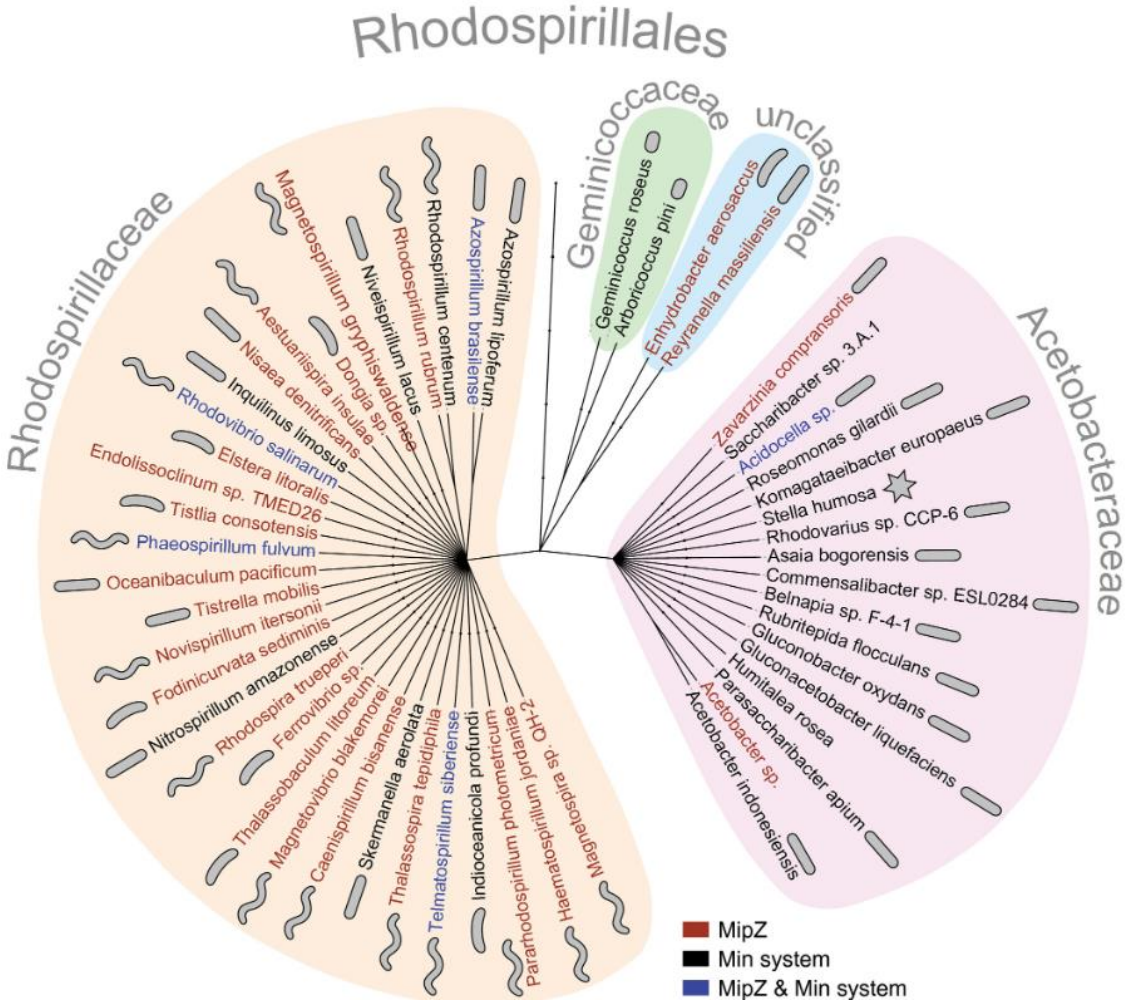


Figure 10 – Phylogenetic tree showing MipZ and Min systems. Image credit: (Toro-Nahuelpan *et al.*, 2019)

At the beginning of the cell cycle in *C. crescentus,* MipZ is concentrated at the pole with ParB molecules which form the partition complex at the *parS* site on the DNA. ParB stimulates the ATP-dependent dimerization of MipZ, and the resulting dimers then bind non-specifically to the chromosome, creating a gradient (Kiekebusch and Thanbichler, 2014). As the chromosome replicates, half of the ParB moves to the opposite pole, which has the effect of mirroring the MipZ gradient in the cell, leading to the lowest concentration of MipZ at mid-cell. This low concentration of MipZ allows the Z-ring to form (Figure 11). The relationship between ParB and MipZ is essential in ensuring that DNA replication has completed before cell division occurs.

Dubarry and colleagues (2019) observed some similar behaviour between MipZ in *R. sphaeroides* and *C. crescentus*, in that both bound non-specifically to DNA, bound to ParB as a monomer and MipZ dimers negatively regulate the polymerisation of FtsZ. There are however some significant differences in the action used to ensure the formation of the Z-ring at mid-cell. The first is that MipZ dimers do not appear to form a gradient but instead were reported to form a ring co-localised with the Z-ring. The second is that MipZ monomers are present at both the pole and mid-cell. Dubarry proposes that "it is possible that there is a dynamic exchange between the monomers and ring-forming dimers" (Dubarry *et al.*, 2019) and that the different mechanism may facilitate the adaptation to the replication and segregation of two chromosomes.

Dubarry suggests that both FtsZ and MipZ monomers localise close to the new pole in a newly divided cell, while OriC-parS complex is at the other pole. As replication and segregation approaches completion (shown as a ParB1-parS1 complex moving to the right of the cell in Figure 11), this releases the MipZ and FtsZ from the pole, allowing them to form structures elsewhere in the cell. Whilst it is clear that the mechanism is different to that of *C. crescentus*, the details, particularly around how MipZ and FtsZ molecules are structured at mid cell, remain unknown.

In *M. gryphiswaldense*, Toro-Nahuelpan and colleagues (2019) observed two MipZ homologues, MipZ1 and MipZ2, which despite their similar sequences have very different behaviour. MipZ1 shows identical behaviour to that of MipZ in *C. crescentus*, forming a gradient across the cell, and preventing FtsZ polymerisation at high concentrations. MipZ2 on the other hand did not cause an obvious phenotype when absent, but is curiously similar to the behaviour of MipZ in *R. sphaeroides*, initially forming foci at the pole before moving to mid-cell as shown on the right of Figure 11 (Toro-Nahuelpan *et al.*, 2019).

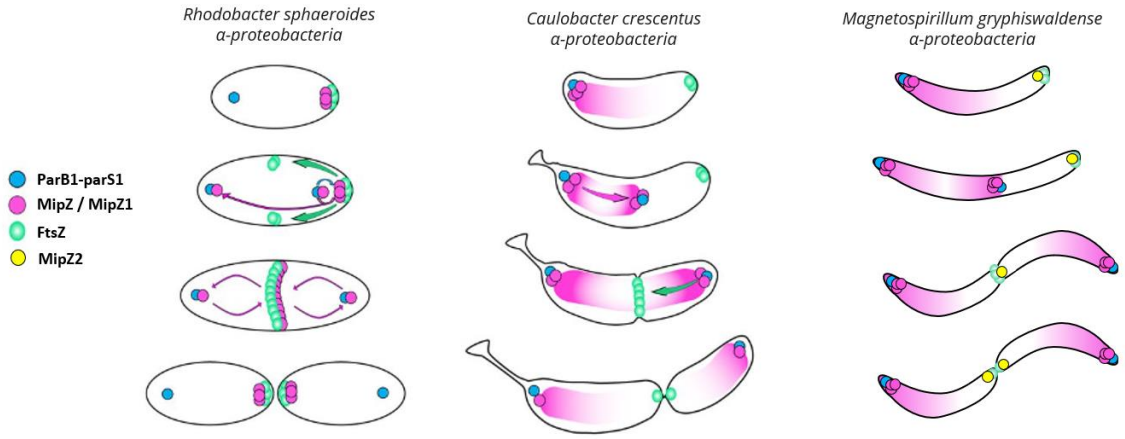


Figure 11- Dynamics of the ParB1-parS1 complex, MipZ(1), FtsZ and MipZ2 (M. gryphiswaldense only) across the 3 species previously studied. Adapted from: (Dubarry et al., 2019)

Other proteins also play a part in regulating the position and behaviour of the Z-ring. One relevant example appears to be FzlA. Goley and colleagues showed that FzlA in *C. crescentus* is essential for cell division and encourages the growth of higher order FtsZ filaments, focusses the Z-ring and causes curvature of FtsZ filaments *in vitro*. Where FzlA is not present, FtsZ rings still form, but constriction does not occur and when it is overexpressed, Z-rings are formed but rarely at mid-cell (Goley *et al.*, 2010). Another pair of proteins associated with *C. crescentus* Z-ring stability are ZapA and ZauP (Woldemeskel *et al.*, 2017).

1.5 Research Motivation

The aim of this work was to develop a microscope combining structured illumination with a solid immersion lens objective, with high spatial and temporal resolution. Once developed, the aim was to test the microscope on a biological system to observe the behaviour of two scaffolding proteins, MipZ and FtsZ in the alphaproteobacteria, *Rhodobacter sphaeroides*.

The proposal is based on the BBSRC grant application DDT00100 and builds upon work completed previously in both fields. For the microscope development, Wang, (2010) and Wang, Pitter and Somekh, (2011) describe the development of a microscope combining structured

illumination microscopy with solid immersion lens which is not fully optimised and not suitable for live cell imaging, mainly due to the mechanical translation of optical components between frames.

The intended application of this technology hopes to provide improved resolution and detail on the discovery of a MipZ ring like structure found at mid-cell prior to division described in Dubarry et al., (2019). This new microscopy approach will be augmented and confirmed through further microscopy and *in vitro* analysis which will be carried out to attempt to understand why MipZ is able to concentrate at mid-cell, close to an FtsZ structure, when MipZ is shown to prevent polymerisation of FtsZ.

2 MATERIALS AND METHODS

2.1 GROWTH CONDITIONS

2.1.1 *R. sphaeroides*

2.1.1.1 Photoheterotrophic Growth

R. sphaeroides was grown at 28°C in the presence of light from tungsten lamps in a microcentrifuge tube with 1.6ml of succinate media (Sux) (see Table 26) and appropriate antibiotics and no shaking.

2.1.1.2 Aerobic Growth

R. sphaeroides was grown at 30°C in liquid Sux (see Table 26) in a shaking incubator (225 rpm, 1" stroke) with appropriate antibiotics. Growth on plates was on LB Agar Table 25 with appropriate antibiotics at 30°C without shaking.

2.1.2 *E. coli*

E. coli was grown in either in LB broth (see Table 25) with appropriate antibiotics at 37°C in a shaking incubator (180 rpm, 2" stroke) or on LB agar (see Table 25) plates with appropriate antibiotics at 37°C with no shaking.

2.1.3 Strains

Strain	Details	Source
R. sphaeroides WS8N	Nalidixic acid-resistant derivative of wild-type WS8	(R. Elizabeth Sockett, Foster and Armitage, 1990)
R. sphaeroides JP2243	WS8N pIND ftsZ::yfp	(Chiu, 2014)
R. sphaeroides SM0019	WS8N ΔmipZ mipZ::snaptag	This study
R. sphaeroides SM0022	SM0019 containing pIND4 ftsZ::halotag	This study
R. sphaeroides SM0049	WS8N ΔmipZ mipZ::halotag	This study
R. sphaeroides SM0050	SM0049 containing pIND4	This study
E. coli DH5α	Cloning strain	NEB
E. coli BL21	Protein expression strain	Lab collection
E. coli Rosetta2	Protein expression strain	Lab collection
E. coli S17	Conjugation donor	Lab collection
E. coli SM0001	BL21 containing pSM0007	Lab collection
E. coli SM0002	BL21 containing pSM0008	Lab collection
E. coli SM0003	BL21 containing pSM0009	Lab collection
E. coli SM0015	BL21 containing pSM0004	This study
E. coli SM0021	Rosetta2 containing pSM0004	This study

Table 2 - Strains used in this research.

2.1.4 Plasmids

Plasmid	Description	Reference
sAK0241	pET15b-sprC	(Kjaer, 2022)
pk18mobsacb	Kanamycin-resistant, sucrose sensitive suicide plasmid	(Penfold and Pemberton, 1992)
pIND	*R. sphaeroides* expression vector	(Ind *et al.*, 2009)
pSM0001	pINDFtsZ-Halo	This study
pSM0002	pk18mobsacb-mipZ-snap-ds	This study
pSM0004	pet15b-FtsZ	This study
pSM0007	pet303-MipZ-His6	Lab collection
pSM0008	pet303-MipZG12-His6	Lab collection
pSM0009	pet303-MipZD40-His6	Lab collection
pSM0022	pk18mobsacb-mipZ-halo-ds	This study

Table 3 - Plasmids used in this research.

2.2 Cloning and DNA Analysis Methods

2.2.1 Polymerase Chain Reaction

Polymerase Chain Reaction (PCR) was used to amplify DNA fragments which could be assembled into plasmids. In the first instance, a reaction of 50 µl reaction 25 µl of Q5® High-

Fidelity 2X Master Mix (New England Biolabs), 2.5 µl of both forward and reverse primer at 10 µM concentration (Merck), a variable amount of template DNA and H_2O to 50 µl was used.

If this reaction failed and the template had high GC content, a 25 µl reaction of 5µl 5X Q5 Reaction Buffer (New England Biolabs), 0.5 µl of 10 mM dNTPs (New England Biolabs), 1.25 µl of both forward and reverse primer at 10 µM concentration (Sigma Aldrich (Merck)), an appropriate volume of template DNA, 5 µl of 5X Q5 High GC Enhancer (New England Biolabs), and H2O to 25 µl.

Primers were designed to specifications detailed in the relevant cloning sections below and purified by desalting. For templates consisting of plasmid stocks or genomic DNA, 1 µl was used. For PCR products, 5 µl was used. The annealing temperature required for a reaction is primer dependent and was calculated using NEB Tm Calculator (https://tmcalculator.neb.com).

PCR reactions were placed into a Thermocycler (ProFlex™ 3 x 32-well PCR System, Thermo Fisher Scientific) running a program constructed according to New England Biolabs specifications which is detailed in Table 4.

Step	Temperature	Time
Initial Denaturisation	98 °C	30 s
35 cycles	98 °C	15 s
	50-72 °C	30 s
	72 °C	30 s/kb
Final Extension	72 °C	2 min
Hold	4 °C	∞

Table 4 - Thermocycler program for Q5 polymerase reactions.

Colony PCR was performed to screen colonies for the insertion of a DNA fragment. Due to the high numbers of colonies which needed to be screened the more cost efficient Taq enzyme was used. The reaction consisted of 5 µl of 2x OneTaq Master Mix (New England Biolabs), 0.5 µl of both forward and reverse primer, H_2O and template DNA. For *E. coli*, 4 µl of H_2O was added

along with a bacterial colony picked from a plate, containing the template. For *R. sphaeroides*, 3 µl of H_2O was added and template was added by first boiling a colony in 20 µl of H_2O for 10 minutes before adding 1 µl of this mixture to the reaction. This is because *R. sphaeroides* is more difficult to lyse than *E. coli*, restricting access to the DNA.

Colony PCR reactions were placed into a Thermocycler (ProFlex™ 3 x 32-well PCR System, Thermo Fisher Scientific) running a program detailed in Table 5.

Step	**Temperature**	**Time**
Initial Denaturisation	98 °C	30 s
30 cycles	98 °C	15 s
	45-68 °C	60 s
	68 °C	60 s/kb
Final Extension	68 °C	5 min
Hold	4 °C	∞

Table 5 - Thermocycler program for OneTaq polymerase reactions

2.2.2 DNA and PCR Product Purification

DNA and PCR products were purified using QIAprep Spin Miniprep Kit (Qiagen) and QIAquick PCR Purification Kit respectively (Qiagen) according to the manufacturer's protocol.

2.2.3 Gibson Assembly

Gibson assembly is a single reaction method of assembling overlapping DNA molecules (Gibson *et al.*, 2009) and was used to create most of the plasmids assembled for this work. The reaction has three stages: 1) Chewing back the 5' end of the DNA with T5 endonuclease, 2) Annealing overlapping 3' ends, 3) Repairing with Phusion polymerase and Taq ligase. Fragments were designed using Snapgene to have around 40 base pair overlaps, which could be created by PCR with an annealing temperature between 50°C and 72 °C. PCR fragments were added to the reaction, along with Gibson Assembly Master Mix (New England Biolabs) and H_2O. After a 4-hour incubation at 50°C, the reaction mixture could be transformed into chemically competent NEB5α *E. coli* cells (New England Biolabs) and plated onto agarose with a selection antibiotic. Colonies could then be screened using colony PCR or used to inoculate liquid culture which was mini-prepped and sequenced to ensure successful assembly.

2.2.4 Site Directed Mutagenesis

Site Directed Mutagenesis (SDM) allows several base pairs in double stranded DNA to be added, removed, or changed. In this study, SDM was used principally to create mutations in the *mipZ* gene to control the dimerization process.

A PCR is the first of the two steps required for SDM. The template is the plasmid requiring modification. For modifications and additions, the forward primer contained the region to be added/modified with ≥10 nucleotides either side, and this was used with a non-overlapping reverse primer, designed to have a similar melting temperature. For deletions, primers were designed to start at either side of the region to be deleted. All primers were designed using NEBaseChanger (https://nebasechanger.neb.com/). The 2nd step is to use KLD mix (New England Biolabs) containing a kinase to phosphorylate the 5' ends, a ligase to join the two ends and DpnI to cleave the methylated DNA which forms the template, leaving only the modified plasmids. The reaction mix was transformed into transformed into chemically competent NEB5α *E. coli* cells (New England Biolabs) and plated onto agarose with a selection antibiotic. Colonies were used to inoculate liquid culture, which was grown, miniprepped and sequenced to ensure the plasmid contained the modification.

2.2.5 Transformation

Plasmids were transformed into chemically competent NEB5α *E. coli* (New England Biolabs) for cloning, S17 *E. coli* for conjugation into Rhodobacter and *BL21 E. coli* for expression of protein for *in vitro* studies. S17 and BL21 cells were made chemically competent by growing overnight, subculturing 1/50 in fresh LB and growing to OD_{600} 0.4. 100 ml of culture was incubated on ice for 30 minutes and spun down for 10 minutes at 1000xg, at 4°C. The supernatant was removed, and pellets were resuspended in 16 ml of TFB1. Cells were incubated at 4°C overnight and centrifuged for 10 minutes at 750xg. After centrifugation, the supernatant was removed and the cells were resuspended in 2 ml of TBF2, before being aliquoted in volumes of 200 µl into microcentrifuge tubes and stored in -80 °C freezer.

TBF I pH 5.8	
$RbCl_2$	100mM
Potassium acetate	30mM
$CaCl_2$	10mM
$MnCl_2$	50mM
Hexamine cobalt chloride	3mM
Glycerol	15% v/v
TBF II pH 6.5	
MOPS	10mM
$CaCl_2$	75mM
$RbCl_2$	10mM
Glycerol	15% v/v

Table 6 - Buffer components for TBF I and TBF II, used in making cells chemically competent.

To transform the plasmid into the selected strain, competent cells were thawed on ice for 20 minutes. DNA was added; 1 µl for a high copy plasmid, and up to 5 µl for a low copy plasmid. Mixture was left on ice for a further 30 minutes before being placed into a 42°C heat bath for 1.5 minutes and then back onto ice for a further 2 minutes. 800 µl of LB was added and the culture was incubated at 37°C for 1 hour before plating onto an LB Agar plate with selection antibiotics and incubated at 37°C overnight. A colony was used to inoculate 5 ml of LB with appropriate antibiotic and grown overnight at 37 °C. 600 µl of this liquid culture was mixed with 900 µl of 50% glycerol (Media Kitchen) and frozen at -80 °C for long term storage of the new strain.

2.2.6 Conjugation

To insert the plasmids into *Rhodobacter sphaeroides,* conjugation was used. 2 days before conjugation, a microcentrifuge tube full (1.6ml) of Sux (1.6ml) + Nal (25 µg/ml) was inoculated with a single colony of the desired WS8N host strain picked from a plate and incubated in a light cabinet using incandescent bulbs at 28°C for 48 hours. The resulting culture was a brown / red colour indicating photoheterotrophic growth.

On the morning of conjugation, 5 ml of LB and Kanamycin (25 µg/ml) (Kan) was inoculated with a single colony of the S17 donor strain, containing the desired plasmid. This was incubated at 37 °C until OD_{600} = 0.3. 1 ml of both strains were spun down at 6000 xg for 1 minute. The resulting

pellets were washed gently with 1 ml of LB and spun down again under the same conditions. The pellets were then resuspended gently in 100 µl of LB.

10 µl of S17 culture was mixed with 100 µl of the WS8N culture. 100 µl of the mixture was carefully pipetted onto a piece of sterile filter paper placed at the centre of an LB plate which was incubated at 30°C overnight. The following morning, the filter paper was transferred to a microcentrifuge tube containing 800 µl of LB and vortexed (Scientific Industries Vortex Genie 2) vigorously. The resulting culture was spread across 8 LB + K + Nal plates and incubated for 2-5 days at 30°C to select for strains containing the plasmid.

A selection of colonies were screened using colony PCR and sequencing to ensure the conjugation was successful.

2.2.7 Homologous Recombination

To insert a section of DNA into one of the chromosomes of *R. sphaeroides*, homologous recombination was used. First a pk18mobsacb (Schäfer *et al.*, 1994) vector was designed to include the fragment to insert into the genome plus two homologous regions of 500 bp, both upstream and downstream of the where the insertion should be made Figure 12.



Figure 12 – Section of pk18mobsacb with insert and 500bp homologous regions interrupting lacZα.

This plasmid was then created using Gibson assembly, transformed into competent *E. coli* and conjugated into WS8N *R. sphaeroides*. One colony of WS8N was picked and grown for 48 hours photoheterotrophically and plated onto plates with M22 media, 10% sucrose and 2% agarose. As M22 is the same as Sux but with the carbon sources removed, the cells are forced to use the sucrose as the carbon source. Cells where no recombination has taken place die as pk18mobsacb is a suicide vector activated by the presence of sucrose.

Each colony was then picked and replicated first onto an LB plate with Nal + Kan and then onto an LB plate with only Nal, assigning each colony the same number on both plates. Colonies where full recombination has occurred will lose the Kan resistance gene present in pk18mobsacb and therefore will not grow on the plate with Kan. Colonies which have grown only on the Nal plate can therefore be checked by PCR and gel electrophoresis for the presence of the insertion.

2.2.8 DNA Analysis by Gel Electrophoresis

0.5 g of agarose was mixed with 50 ml of TAE buffer (or 1 g into 100 ml for a large gel) and microwaved until the agarose had fully dissolved. 5 µl (or 10 µl for a large gel) of SYBR Safe DNA Gel Stain (ThermoFisher Scientific) was added to the solution which was then poured into a gel frame with a comb placed to create wells as the solution hardened. Once the gel had formed, the frame was placed into a tank filled with TAE buffer (Table 7).

TAE Buffer	
TRIS Base	4.84g/L
Acetic Acid	1.142ml/L
EDTA	0.372g/L
pH 8.2 with Acetic Acid	

Table 7 – TAE Buffer

8 µl of each DNA sample was mixed with 2 µl of DNA running dye (Qiagen) before being deposited into one of the wells in the gel. 5 µl of DNA ladder (HyperLadder 1kb, Meridian Bioscience) was loaded into every 9th well. The gel was then subjected to 120V for 30-40 minutes. Gels were then removed and imaged using blue light (E-Gel Imager, Invitrogen).

2.2.9 DNA Sequencing

Sanger sequencing (Source BioScience) was used to confirm the construction of all plasmids and genomic mutations. Plasmids were sequenced using forward and reverse primers either side of the insertion site (Table 8). Genomic insertions were checked using colony PCR and sequencing the PCR product, using a primer downstream of the insertion site.

Plasmid	Forward Primer	Reverse Primer
pIND-4	PQE30 forward	PQE30 Reverse
Pk18mobsacb	M13F	M13R
Pet15b	T7F	T7R
Colony PCR product of WS8N chromosomal with SNAP-TAG insertion or Halo-Tag insertion	priSM0033	

Table 8 – Sequencing primers

2.3 Protein Analysis Methods

2.3.1 Sodium Dodecyl Sulphate and Polyacrylamide Gel Electrophoresis

Sodium Dodecyl Sulphate and Polyacrylamide Gel Electrophoresis (SDS-PAGE) was used to assess the molecular weight distribution of protein samples and their relative abundance.

Samples were mixed with SDS-PAGE sample buffer and boiled for 5 minutes before being loaded into a Mini-PROTEAN TGX Precast poly-acrylamide gel (Bio Rad) submerged in SDS-PAGE running buffer (Table 9). All gels included Precision Plus Dual Color ladder (Bio Rad). The gel was then run at 35mA for 40 minutes before staining with Coomassie Blue Solution (Table 9). The gel was then destained using Destain Solution and imaged in white light (Table 9).

1x SDS-PAGE Sample Buffer	
Tris-HCl pH 6.8	375mM
SDS	10% w/v
Glycerol	50% v/v
Bromophenol blue	0.1% w/v
1x SDS-PAGE Running Buffer	
Tris	25nM
Glycine	192nM
SDS	0.1% w/v
DTT	10mM
Coomassie Blue Stain Solution	
Coomassie Brilliant Blue R250	2.5% w/v
Glacial acetic acid	10% v/v
Ethanol	25% v/v
Destain Solution	
Glacial acetic acid	15% v/v
Ethanol	10% v/v

Table 9 – SDS PAGE materials

2.3.2 Western Blot

To attain specificity when detecting the presence of a protein, a Western Blot was used. To run a western blot, the protocol for an SDS-PAGE gel (see 2.3.1) was followed but without the staining or detaining steps.

5 blotting papers (Bio Rad) were wetted in transfer buffer (Bio Rad) until they were soaked and placed on the base of the anode base of the case of the TransBlot system (Bio Rad). This process was repeated for the membrane (Bio Rad), the SDS-PAGE gel and another 5 layers of blotting paper. The stack was gently rolled to remove excess buffer before adding the lid containing the cathode and pouring out the excess buffer. The case was then inserted into to the TransBlot and using the 3-minute transfer protocol for TGX precast gels, the gel was transferred to the membrane.

To visualise the proteins transferred onto the membrane, it was stained with Ponceau red (0.1 % (w/v) Ponceau S, 5% (v/v) acetic acid), imaged using a desktop scanner (HP) and destained with water.

To block non-specific antibody binding, the membrane was soaked in blocking buffer (1% milk powder dissolved in TBST (20 mM Tris-HCl pH 7.6, 137mM NaCl, 0.02% Tween-20)) for 1 hour under constant agitation before adding the primary antibody, Mouse α 6xHis tag (MA1-21315, Invitrogen). This was left overnight at 4°C under constant agitation.

The membrane was then washed 3 times in TBST, before a 1 hour incubation under agitation in blocking buffer plus the secondary anti-body Goat α Mouse (A4416, Merck) at room temperature. Finally the membrane was washed in TBST for 20 minutes and sprayed with Immobilon Forte Horseradish peroxidase (HRP) substrate (WBLUF0500, Merck) before being imaged in G:Box running GeneSys software (Syngene).

2.3.3 In-gel Fluorescence

Successful protein labelling was checked using in gel fluorescence. 1 ml of cells was spun down and resuspended in 100 µl of sample and 1 µl of 100 µM of dye was added to it and mixed gently. This was incubated at 30°C for 20 minutes before washing 5 times by pelleting at 4000 xg prior to resuspending in fresh Sux. After the final wash, the pellet was resuspended in 50 µL of SDS buffer without loading dye and incubated at 50°C for 10 minutes. Samples were then loaded into a Mini-PROTEAN TGX Precast poly-acrylamide gel (Bio Rad) submerged in SDS-PAGE running buffer with Precision Plus Dual Color ladder (Bio Rad). The gel was then run at 35 mA for 40 minutes and imaged on Amersham Typhoon (Cytiva) laser scanner using the Cy5 settings for JF646 and JF669 and TMR for JF549.

2.3.4 Liquid Chromatography with tandem mass spectrometry

Protein samples were analysed using Liquid Chromatography with tandem mass spectrometry (LC-MS-MS) at University of St. Andrews Mass Spectrometry and Proteomics Facility. Samples were cut out of an SDS-PAGE gel and posted in a microcentrifuge tube with 10 µl of PBS.

3 OBSERVING THE BEHAVIOUR OF FTSZ AND MIPZ

In this chapter I carry out imaging experiments to observe the behaviour of MipZ and FtsZ. I label FtsZ on the expression vector pIND, by replacing the YFP gene on the plasmid pIND FtsZ-YFP (Chiu *et al.*, 2013) with the Hato-tag sequence (see 3.2.2). I also create strains of *R. sphaeroides* with MipZ genomically labelled with Halo-tag and SNAP-tag using the suicide vector pk18 mobsacB (Penfold and Pemberton, 1992) (see 3.2.2). I then performed time lapse imaging and analysed the results as detailed in 3.2.

3.1 INTRODUCTION

The previous work on this topic (Dubarry *et al.*, 2019) focused on observing the locations of FtsZ, MipZ and ParB foci at different stages of cell division, demonstrating counterintuitively when compared to other species, that both FtsZ and MipZ form a ring-like structure at the septum prior to division. This built on previous work by Chiu *et al.*, (2013) which showed FtsZ in *R. sphaeroides* moves out from the poles in focussed spots, before seemingly extending around the cell to form the Z-ring. Research in other species such as *E. coli* and *B. subtilitus* (Coltharp *et al.*, 2016; Bisson-Filho *et al.*, 2017) shows that FtsZ rings are not complete rings but instead rather patchy, highly dynamic structures formed of treadmilling FtsZ filaments. In this chapter I will investigate whether these ring-like structures formed by both FtsZ and MipZ in *R. sphaeroides* are complete, or indeed patchy, and I will determine whether these proteins show treadmilling behaviour in *R. sphaeroides.* Additionally, I will examine the relationship between FtsZ and MipZ dynamics to see if this relationship yields any insight as to why both proteins form ring-like structures at mid-cell.

To this end, I will image live *R. sphaeroides* using fluorescence microscopy, utilising Halo-tag and SNAP-tag labelling systems with organic dyes. To my knowledge, this is the first instance of Halo-tag and SNAP-tag bound dyes being used in α-proteobacteria. Using this kind of tag

provides a flexible platform allowing many types of bright dyes to be changed without the need for further cloning.

As bacterial cells are small and the treadmilling effects I am trying to observe occur close to the cell membrane, I chose to use Total Internal Reflection Fluorescence (TIRF) (see 0) and Highly Inclined and Laminated Optical sheet microscopy (HILO). Both techniques work by translating the illumination light across the back aperture to the edge or near the edge of the objective, providing an inclined illumination. In the case of TIRF, this beam is inclined to such an extent that all the light is reflected by the interface between the coverslip and the sample. This creates an evanescent wave field, which illuminates around 200nm of the sample depth. As a result, any treadmilling elements would only be observed when passing near the tangent of the coverslip, meaning only one side of the ring is observed, making results easier to interpret. Where the protein of interest sits further away from the coverslip, HILO can be used instead to provide illumination of the whole cell, whilst eliminating background fluorescence from most of the agarose pad which sits behind.

Despite my desire to use TIRF in this study, the version of the NanoImager (ONI) microscope I was using did not have an objective capable for performing TIRF. Unfortunately, this did not become clear until after the completion of this work and therefore, imaging was performed in HILO with an illumination angle of incidence of either 52.5° (which was mistakenly thought to be the TIRF setting) or 51°. See 3.4.3 for further discussion.

3.2 Materials and Methods

3.2.1 Growth for microscopy

Prior to imaging, a single colony of WS8N was picked from an LB + Kan plate and grown at 30°C in a shaking incubator overnight in 5ml Sux + Kan. On the day of experiment, this colony was used to start another sub-culture in 5ml of Sux + Kan at an optical density at 700 nm (OD_{700}) of 0.05. This sub-culture was grown at 30°C to an OD_{700} of 0.3-0.4 in a 50ml conical flask to

ensure aerobic growth conditions were maintained. OD_{700} is used in place of OD_{600} because photosynthetic pigments in photoheterotrophically grown *R. sphaeroides* absorb light at 600 nm. Whilst this theoretically should not matter for these imaging experiments which use aerobically grown cells, using OD_{700} ensures consistency with other experiments in this thesis and previous work in *R. sphaeroides* (Shah *et al.*, 2000; Potter, 2021; Khoo, Miller and Armitage, 2022).

3.2.2 Labelling techniques

For this study, the organic dyes JF669-SNAP, JF646-Halo and JF549-Halo were used. These dyes feature a high extinction coefficient and quantum yield, which results in high fluorescence signal levels when combined with an appropriate illumination source and imaging system. This in turn gives higher signal to noise ratios when imaging. Finally, because these dyes are excited in the red and green parts of the spectrum, they induce less phototoxicity effects in the sample. It should be noted that, if *R. sphaeroides* was being imaged following photoheterotrophic growth, there would be considerable auto-fluorescence at these wavelengths, however, under aerobic growth conditions, this is not present because the cells do not feature the photosynthetic pigments.

The dyes are bound to a HaloTag (Los *et al.*, 2005, 2008) or SNAP-tag (Keppler *et al.*, 2003) ligand which is designed to bind covalently to a HaloTag or SNAP-tag protein, respectively. The HaloTag is derived from haloalkane dehalogenase and is engineered to specifically and efficiently bind a chloroalkane linker. Unlike the wild type enzyme, the HaloTag cannot regenerate after binding the ligand, meaning the covalent bond between the two is maintained (Los *et al.*, 2005, 2008). The SNAP-tag is derived from human DNA repair protein O6-alkylguanine-DNA alkyltransferase modified to specifically and irreversibly bind ligands containing an O6-benzylguanine group rather than damaged DNA (Keppler *et al.*, 2003).

To label the proteins of interest with the dye, a C-terminal HaloTag or Snap-tag fusion protein is created by inserting the DNA to encode for the tag protein downstream of the gene which encodes the protein of interest, with a 6 amino acid linker placed between the two. The fusion protein is then able to bind the ligand-tagged dye.

Since a functional genomic FtsZ fusion has yet to be demonstrated in α-bacterium, FtsZ-Halo was expressed from the expression vector pIND using the leaky Plac promotor. This results in wild type levels of FtsZ present in the cell with a small number of FtsZ-Halo proteins, allowing us to observe the behaviour of FtsZ.

To label the FtsZ-Halo proteins, 1ml of cells at 0.3-0.4 OD_{700} were spun down and resuspended in 100µl of sample and 1µl of 100µM of dye was added to it and mixed gently. This was incubated at 30°C for 20 minutes (Eppendorf Thermomixer 5350) before washing 5 times by pelleting at 4000 xg prior to resuspending in fresh Sux. This process is to ensure that any unbound dye is removed from the sample.

3.2.3 Sample mounting

A pad of Sux with 1% agarose was prepared by heating the mixture, ensuring all of the agarose had dissolved and then pipetting 30 µL onto a coverslip. It was then flattened to give a pad thickness of around 0.8mm, and subsequently allowed to solidify.

The sample pellet was resuspended in 50µl of Sux and 1µl was deposited onto the pad. A second 50 x 24 #1.5H coverslip was then placed onto the sample. Prior to sample preparation, the coverslips were pretreated by heating to 500 °C in a furnace for 1 h to remove fluorescent background particles.

3.2.4 Imaging protocol

Images were taken using an ONI Nanoimager featuring a 1.4 NA oil immersion objective (Olympus) and ORCA-Flash 4.0 V3 CMOS camera (Hamamatsu).

Prior to the fluorescence time series being captured, a single frame brightfield image was taken using the 532 nm transmission illumination LED at an exposure of 50 ms.

For the fluorescence time series, a 640 nm and 532 nm laser (as appropriate) were used to illuminate the sample simultaneously with 2 channel detection at 665-705 nm and 550-620 nm. An illumination angle setting of 52.5° was used.

120 images were captured with a 50ms exposure and a delay of 2 seconds between each image. The delay of 2 seconds was chosen as a compromise to allow imaging over longer time periods without significant photobleaching, whilst also providing a high enough temporal resolution to observe the dynamics not visible in previous work. To prevent unnecessary photobleaching, the laser was turned off between exposures.

3.2.5 Image analysis

Brightfield images were overlayed with fluorescence images of the same field of view (FoV) using the FIJI code included in Appendix 7.1 (Schindelin *et al.*, 2012), allowing the cell morphology and protein of interest's position to be analysed within the same image (Figure 13). The minimum and maximum values for the lookup tables were optimised so fluorescence and bright field were both visible. A line was drawn manually connecting the poles of the cells (a) and across the fluorescence of the cell (b). This was done for every cell in the field of view, ignoring any cells which were part of a cluster larger that 4 cells.

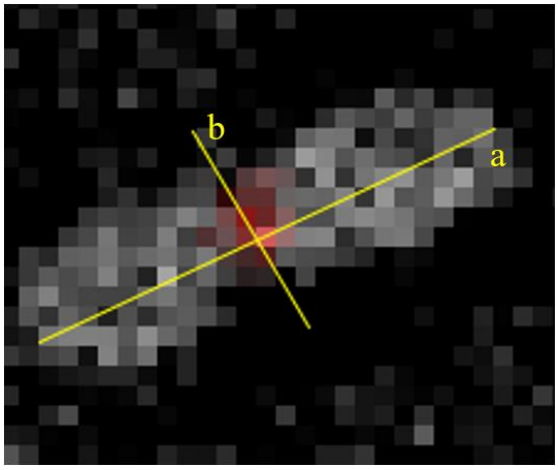


Figure 13 – Image of R. sphaeroides with line overlays along the length (a) and the fluorescence (b) of the cell

Line (a) was used to measure the cell length, which was used as a classifier to group the results. Line (b) was used to create a kymograph for that cell using KymographBuilder (Mary, 2022).

As growth of *R. sphaeroides* cannot be synchronised, cells were sorted into groups of: a < 2μm, 2μm ≤ a ≤ 2.5μm and a > 2.5μm to observe timepoints across the cell lifecycle, where shorter cells are the younger and long cells are the older cells, closest to division. These limits were chosen on the basis of typical cell length for a recently divided cell, an elongated cell and a cell where invagination has started to occur in previous data (not shown).

Kymographs were analysed by calculating the centroid of each line and connecting these centroids with a line which ran down the kymograph. This was achieved using the code in 7.7. This line was smoothed using a rolling average over 40s and then the difference between each point on this line was used to calculate a velocity profile.

3.2.6 Control experiments

For each strain used it is important to verify that the behaviour of the modified strain is consistent with that of the wild type. As both MipZ and FtsZ are associated with cell division, cell length and growth rates are good indicators of whether adding a tag to genomic MipZ, or introducing tagged FtsZ at a low copy number from pIND, in addition to the wild type copies has changed the behaviour of these strains.

As nalidixic acid (Nal) causes clumping of cells during growth, WS8N + pIND was used instead of wild type for negative controls. As pIND infers Kan resistance on cells, Kan which does not causing clumping, can be used in place of Nal to prevent contamination during growth.

3.2.6.1 Cell Morphology

Brightfield images were recorded for each FoV during the fluorescence imaging experiments. The lengths of a representative subset of these cells were recorded and are compared in Figure 14. It shows similar distributions for all 3 strains indicating the growing behaviour of mutant strains is similar to that of the WS8N + pIND wild type. A student t-test demonstrates this with p-values of 0.402 and 0.176 when SM0020 and SM0050 respectively are compared to WS8N + pIND. These are greater than 0.05, below which the difference would be statistically significant.

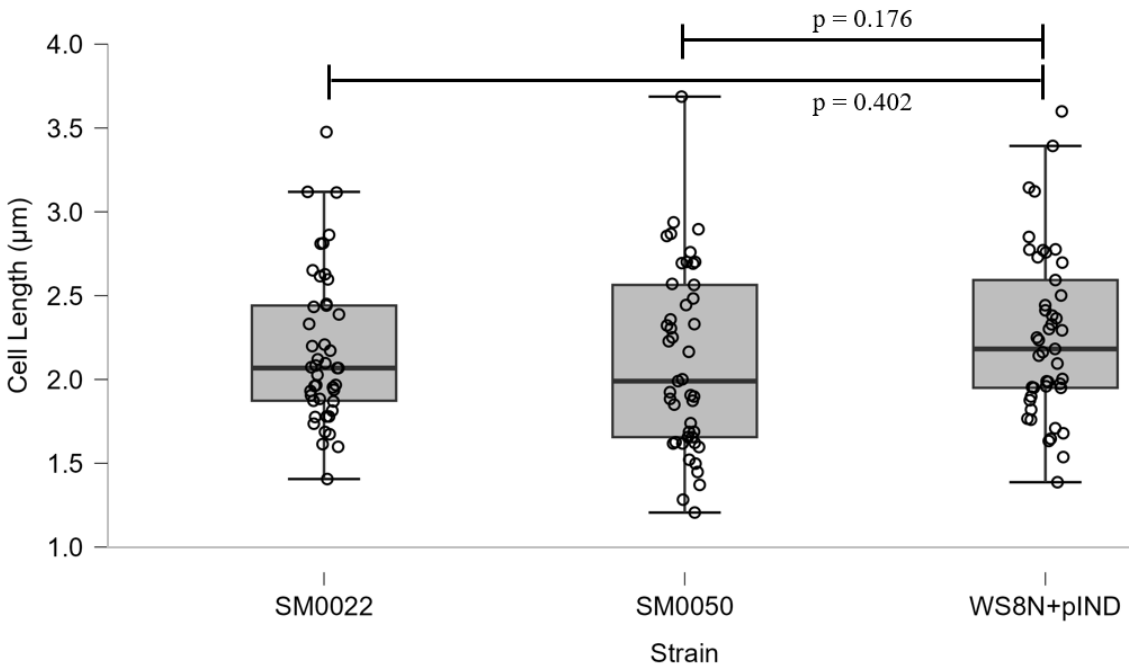


Figure 14 - Comparison of R. sphaeroides cell lengths of 45 cells of each mutant, SM0020, SM0050 and the wild type WS8N + pIND. Boxes indicate interquartile range with median, whilst whiskers indicate 1.5x interquartile range.

3.2.6.2 Growth curves

Samples were grown overnight from single colonies, and then sub-cultured to OD_{700} 0.05. 150µL of each sample was deposited into a 96 well plate (Costar 96, Corning). Samples were grown in the CLARIOstar plate reader (BMG Labtech) at 30°C, shaking at 200 rpm. Growth rate was monitored using OD_{700} at 327 s time intervals, averaged across 12 locations in the well. 199 readings were taken, meaning growth was tracked over a period of around 18 hours. Unfortunately, due to data corruption, only the mean values of the 12 locations were available to be analysed, preventing any statistical testing.

The results shown in Figure 15 demonstrate that the growth rate of each of the three strains used in this study is roughly the same, suggesting that the modifications made to create SM0022 and SM0050 have not changed the growing behaviour of the strain.

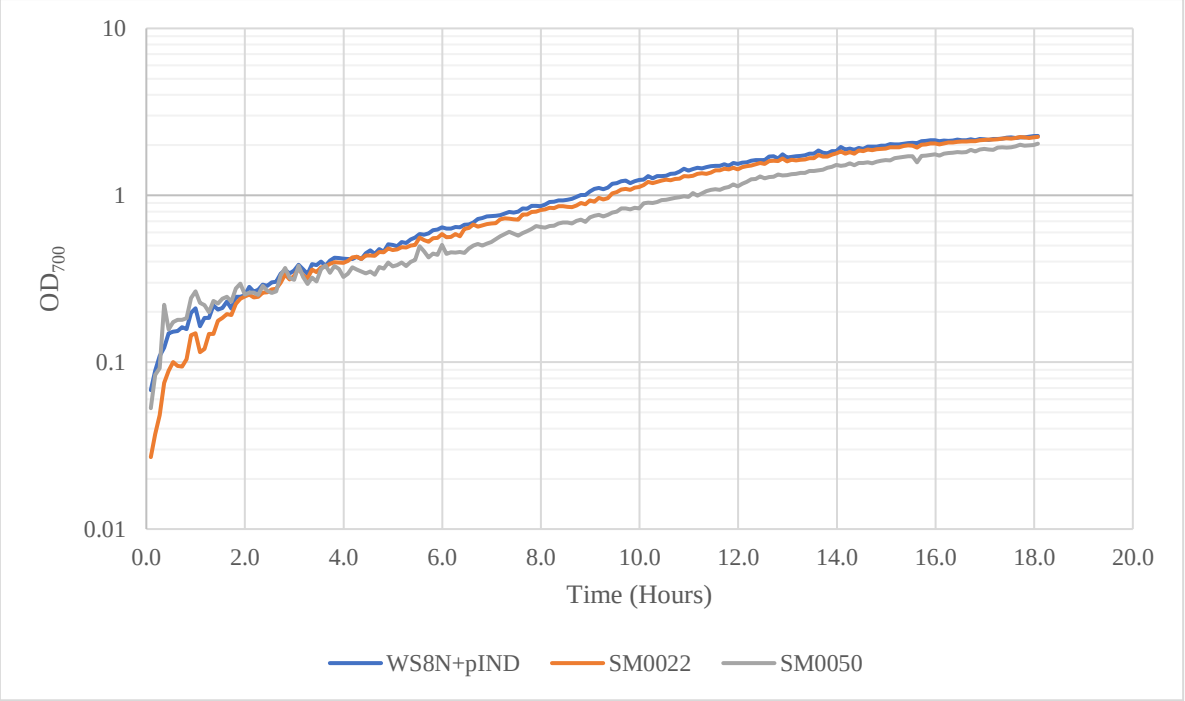


Figure 15 – OD_{700} of the three strains of R. sphaeroides used in this experiment over time. Readings are relative to the starting OD of the lowest reading on the plate. This was used in place of a blank due to some suspected contamination.

3.2.6.3 In-gel fluorescence

To ensure that the proteins of interest were correctly labelled, in-gel fluorescence was used. Figure 16a shows the band for FtsZ-Halo is clearly visible at around 92 kDa and a faint band for MipZ-SNAP is visible at 49 kDa. I can be confident that these bands are associated with the proteins of interest due to them only being present in the one lane, indicating they are not due to a native protein and are close to the predicted molecular weights of FtsZ and MipZ. The dark lower molecular weight bands are likely the result of loading dye not properly running off the gel. The cause is unlikely to be non-specific binding of the dye to native protein, as the bands appear identically in both lanes of the gel, despite them using different labelling systems. The faint band for MipZ-SNAP is likely due to the fact that the laser and filter set on the Amersham Typhoon is optimised for Cy5 with an excitation wavelength of 635 nm and emission filter pass band of 655 nm to 685 nm, which does not align well with the λ_{EX} = 674 nm and λ_{EM} = 685 nm of JF669 dye.

The JF646 dye on the other hand aligns much better, with a λ_{EX} = 655 nm and λ_{EM} = 667 nm. This is shown by the difference in area under the respective curves in Figure 16b.

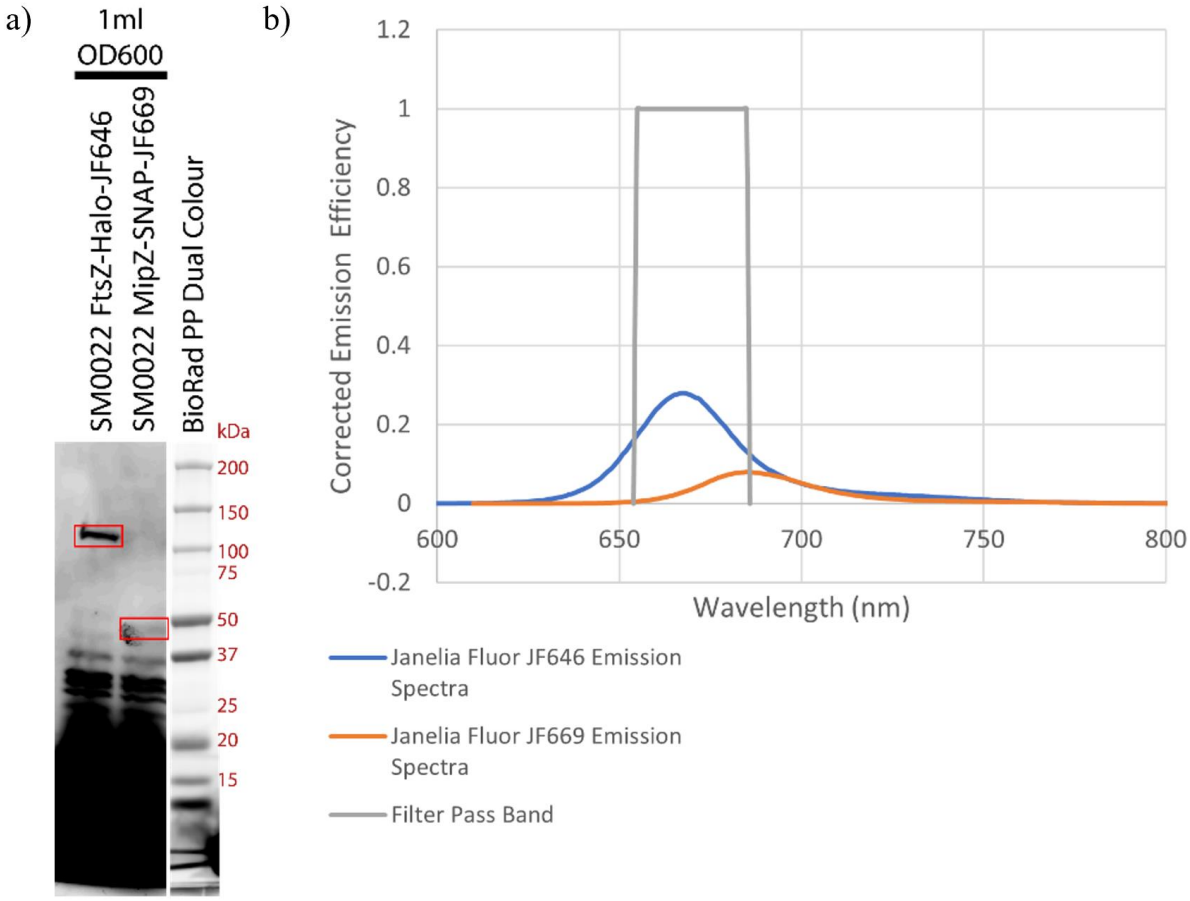


Figure 16 – In-gel fluorescence results. a) In-gel fluorescence of SM0022 with Halo-tag labelled FtsZ and SNAP-tag labelled MipZ. b) Graph of emission spectra for JF646 and JF669, corrected for excitation efficiency at 635nm, and the quantum yield and excitation coefficient of each dye (Lambert, 2019).

3.3 RESULTS

3.3.1 Dual Colour Imaging of MipZ and FtsZ

To understand how the dynamics of FtsZ and MipZ interact, it is important to image both proteins simultaneously, so that their positions can be understood relative to one another. To achieve this, SM0022 expressing native FtsZ and MipZ-SNAP from the chromosome and FtsZ-Halo at leakage

levels from the expression plasmid pIND were labelled with JF549-Halo for FtsZ and JF669-SNAP for MipZ. For simultaneous 2 colour channel imaging, I used the protocol detailed in 3.2.4.

During imaging, dye molecules were observed diffusing within the confines of the cell (Figure 17) forming no foci. To ensure that this behaviour was not an artifact due to free dye in the cell, further wash steps and incubation were carried out, however dye molecules were still observed diffusing within the cell, which suggests that this observation was either genuinely unexpected behaviour of MipZ, or the SNAP-tag was binding to another, native protein in the cell. Expanded material on this is found in 3.3.2 and is discussed in 3.4.1.

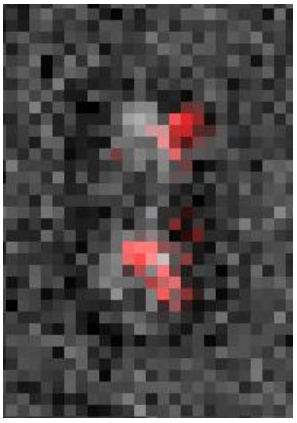


Figure 17 - Examples of JF669 dye distributed across the cell, which was not expected behaviour for MipZ.

3.3.2 SNAP-tag Ligand Binding to Native *R. sphaeroides* Protein

To test if the SNAP ligand was binding to a native protein in *R. sphaeroides*, I ran an in-gel fluorescence experiment to see if another protein was binding the SNAP-tag ligand and dye. SM0022, the WS8N mutant with SNAP-tag encoded on the genome at the C-terminal of MipZ, was run with JF669-SNAP dye, with and without Carbonyl Cyanide m -Chlorophenylhydrazone (CCCP) (Merck) which reduces active transport of dye out of the cell. WS8N + pIND was used as a negative control as this does not encode for the SNAP-tag protein.

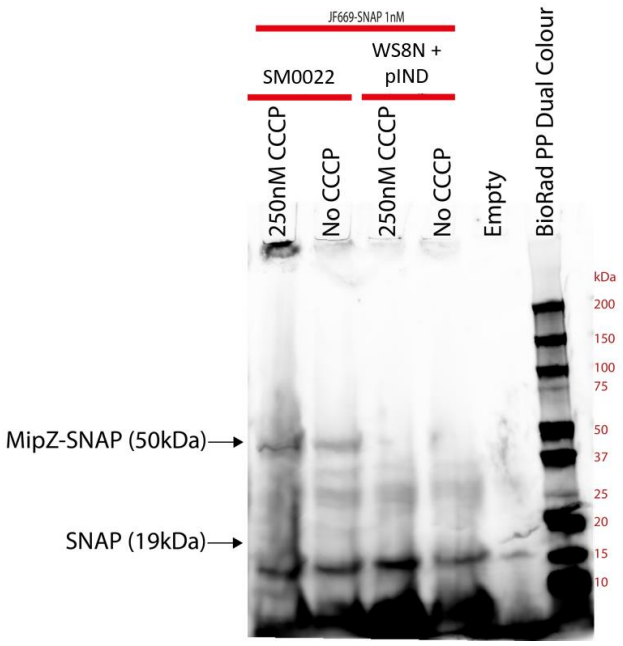


Figure 18 - In-gel fluorescence image of SM0022 and WS8N+pINDlabelled with JF669-SNAP.

While Figure 18 shows a clear band at the estimated size for MipZ-SNAP (50 kDa), there was a darker band at around 15 kDa, in both mutant and wild type. This has to be the result of the dye binding to a native protein or an auto-fluorescent native protein. Further controls which could have helped with this are discussed in 3.4.1. The weaker band in the empty lane is likely due to cross contamination when filling the wells.

To predict what this protein might be, BLASTp was used to compare the SNAP-tag protein against the *R. sphaeroides* WS8N genome (*Rhodobacter sphaeroides* – taxid: 992186). Methylated-DNA-protein-cysteine methyltransferase, predicted to be 15.5 kDa, was found to be similar, meaning it is highly likely that this protein is binding the SNAP-tag ligand. SNAP-tag binds to an active cysteine (Cole, 2013) as highlighted in pink in Figure 19.

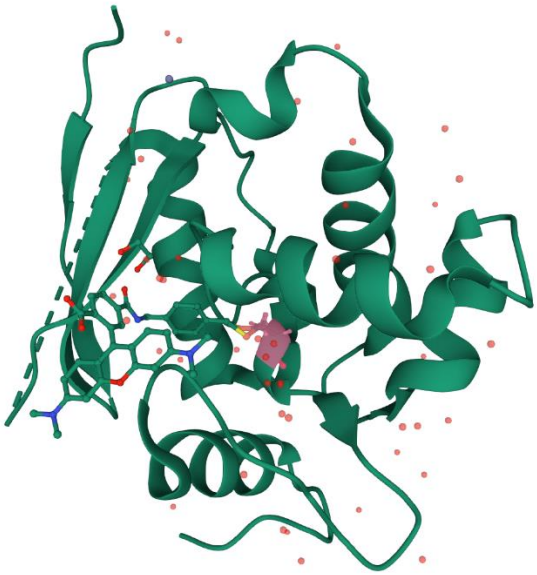


Figure 19 - Structure of SNAP-tag protein with corresponding ligand bound at the active cysteine highlighted in purple. PDB ID: 6Y8P (Berman *et al.*, 2000; Sehnal *et al.*, 2021; Wilhelm *et al.*, 2021)

The amino acid sequence of the area surrounding the binding site of the SNAP ligand was aligned with the proteome of some species where the SNAP-tag system has been shown to work: *E. coli* (Landgraf *et al.*, 2012) and *F. johnsoniae* (Kjaer, 2022). In each case, there is strong alignment between part of the Methylated-DNA--protein-cysteine methyltransferase protein in each species, and the SNAP-tag ligand binding site in the SNAP-tag protein.

Of the three species, WS8N has the strongest alignment in this section, with 13 consecutive amino acids matching or having equivalence. In particular, the proline highlighted in green in Table 10 is only present in WS8N.

SNAP-tag	KTALSGNPVPILIPCHRVVQGDLDV
WS8N *(taxid: 992186)*	A NP+PIL+PCHRV+ G +
F. johnsoniae (taxid:986)	+A NP+ I +PCHRV+ D +
E. coli (taxid:1403831)	A NP+ I++PCHRV+ + +

Table 10 – Amino acid alignment of the section surrounding the active site (purple) in SNAP-tag protein against sections of Methylated-DNA--protein-cysteine S-methyltransferase in WS8N, F. johnsoniae and E. coli.

When the AlphaFold prediction of the structures of methylated-DNA--[protein]-cysteine S-methyltransferase from WS8N and *F. johnsoniae* are compared (Figure 20), there appear to be no significant differences between the two. However, there are some differences between the disordered regions, which could affect the accessibility of the active cystine.

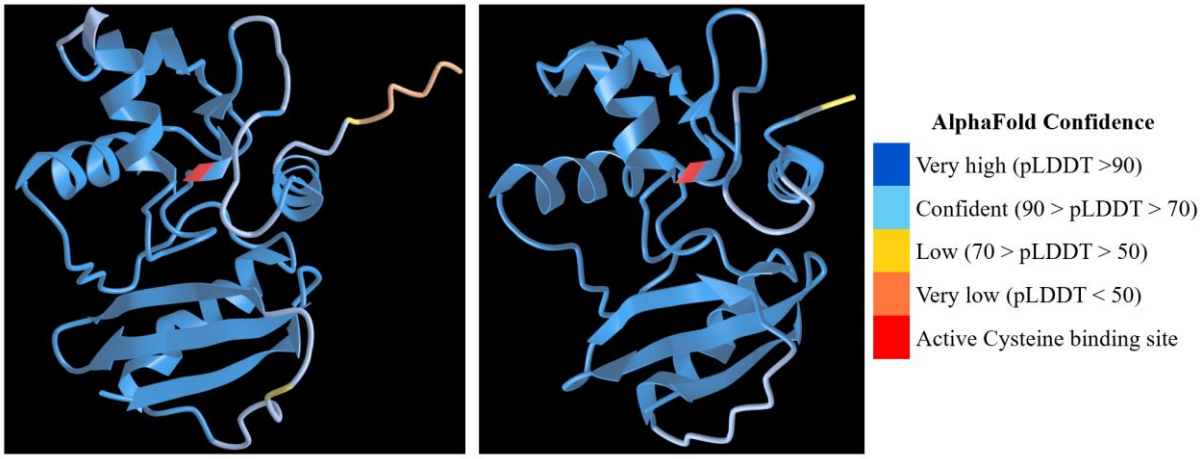


Figure 20 - AlphaFold predictions of Methylated-DNA--protein-cysteine S-methyltransferase structures from both F. johnsoniae (left) and WS8N (right) where the active Cysteine binding site has been highlighted in red. Both models are predicted with a reasonably high degree of confidence as shown by the high predicted local distance difference test (pLDDT) where a maximum score of 100, predicts the highest confidence in the location of that amino acid.

3.3.3 Single colour imaging

It was clear from the work presented in the sections above that the SNAP-Tag could not be used. However, there was not enough time to re-label with an untested tag, and therefore I focused

experiments on imaging FtsZ and MipZ dynamics individually using a C terminal Halo-tag on both proteins. Whilst not as conclusive as dual labelling, the dynamic behaviour of MipZ and FtsZ can be compared to determine the potential link between the two.

Using SM0022 and SM0050, both labelled with JF646-Halo as described in 3.2.2, cells were imaged using the red channel of the NanoImager (ONI).

Of the cells imaged, 34% exhibited fluorescent foci at mid-cell and 2% featured disperse fluorescence across the cell. In cells with fluorescence at mid-cell, the FtsZ foci were either dynamic as demonstrated in Figure 21a, or static, as shown in Figure 21b.

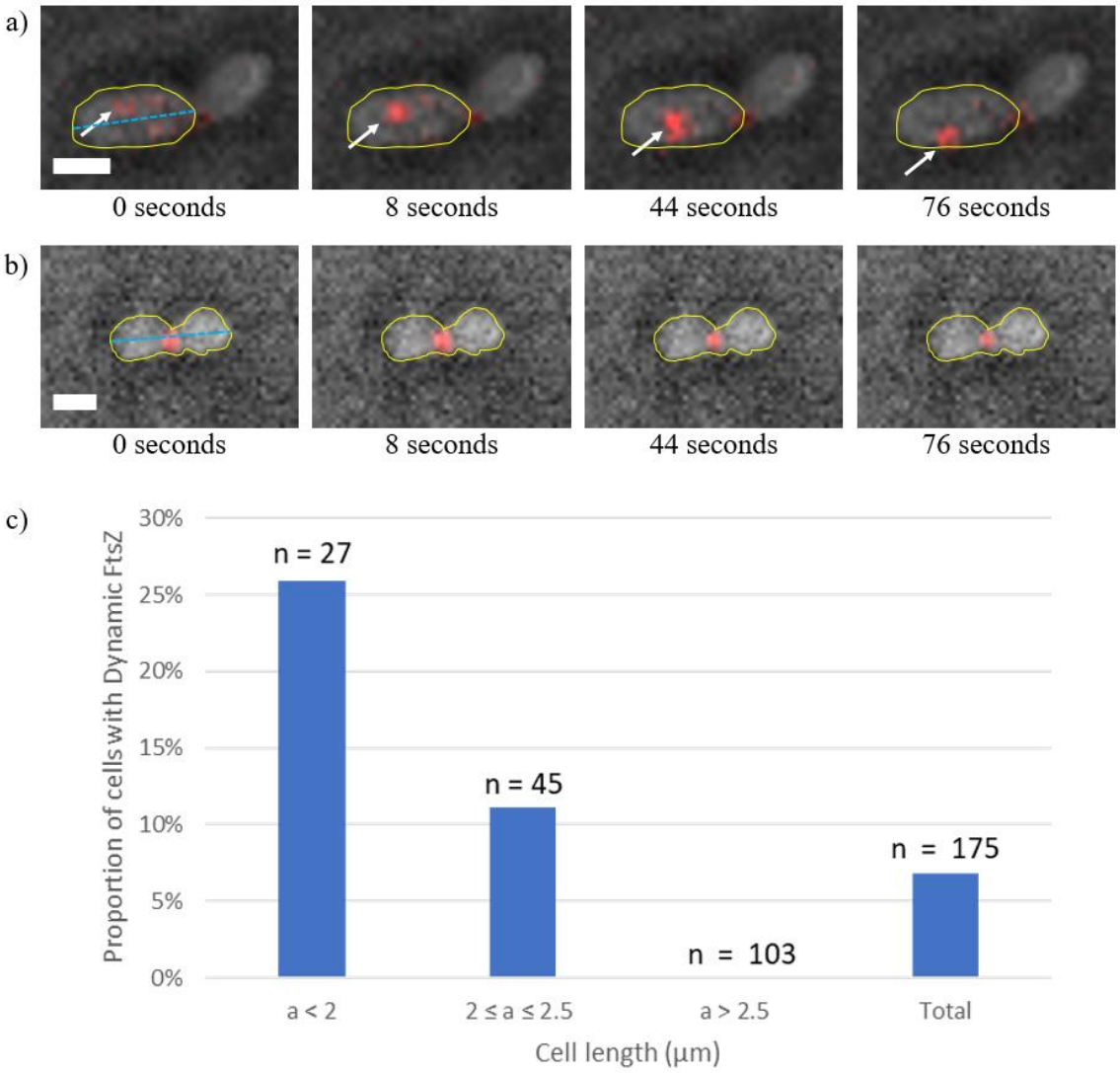


Figure 21 – a) HILO image of SM0022 where a < 2 µm showing FtsZ moving across the mid-cell region highlighted by the white arrow. Scale bar 1 µm; blue dotted line is measured length. b) HILO image of SM0022 where a > 2.5 µm showing stationary FtsZ location. Scale bar 1 µm; blue dotted line is measured length. c) Proportion of cells with fluorescence at the septum where FtsZ exhibits dynamic behaviour for each the three cell classes.

Following classification by length as described in 3.2.5, the kymograph of each cell was analysed manually, and where the profile varied from top to bottom, the cell was classed as having dynamic foci, otherwise, the foci was classified as static. The 175 cells with static or dynamic foci at mid-cell were counted and plotted in Figure 21c. This shows 7% of them exhibited dynamic behaviour and that this behaviour is mostly observed in the shorter classes of cell, with 26% below 2µm and

16% of between (inclusive of) 2 and 2.5 μm. Of the 103 cells longer than 2.5 μm there are none exhibiting dynamic behaviour.

With this experimental design, this is expected behaviour as the shorter cells are further in time from their next division and this period is associated with dynamic spots of FtsZ (Chiu *et al.*, 2013). As the cell elongates and approaches division, the FtsZ structure becomes denser and has a constricting diameter, which means that fluorescence from multiple FtsZ filaments combine into one structure, and movements are much smaller. Constriction may also mean that the entirety of the ring enters the effervescent field (see 0), meaning that fluorescence from the entire ring can be observed simultaneously. Unfortunately, from the present experiment I cannot conclude whether the static behaviour observed is genuinely static or whether, as is suggested by other work (Bisson-Filho *et al.*, 2017; Wagstaff *et al.*, 2017; Whitley *et al.*, 2021), FtsZ at mid-cell is treadmilling.

3.3.4 Kymograph analysis of FtsZ data

FtsZ motion from each *R. sphaeroides* cell with fluorescent foci away from the poles was plotted onto a kymograph for further analysis, with each row of pixels representing the pixel intensity along line b (see 3.2.5) at a single time point. This allows us to examine the dynamics along line b across the 240 s movie. Figure 22 and Figure 23 show selected kymographs typical of dynamic FtsZ foci in *R. sphaeroides* cells with lengths below 2 μm, and between 2 μm and 2.5 μm. Whilst there is clear movement across the circumference of the cell, it is not at a constant velocity, sometimes appearing stationary, before moving. In some kymographs, the fluorescence appears to change direction in a more sinusoidal manner.

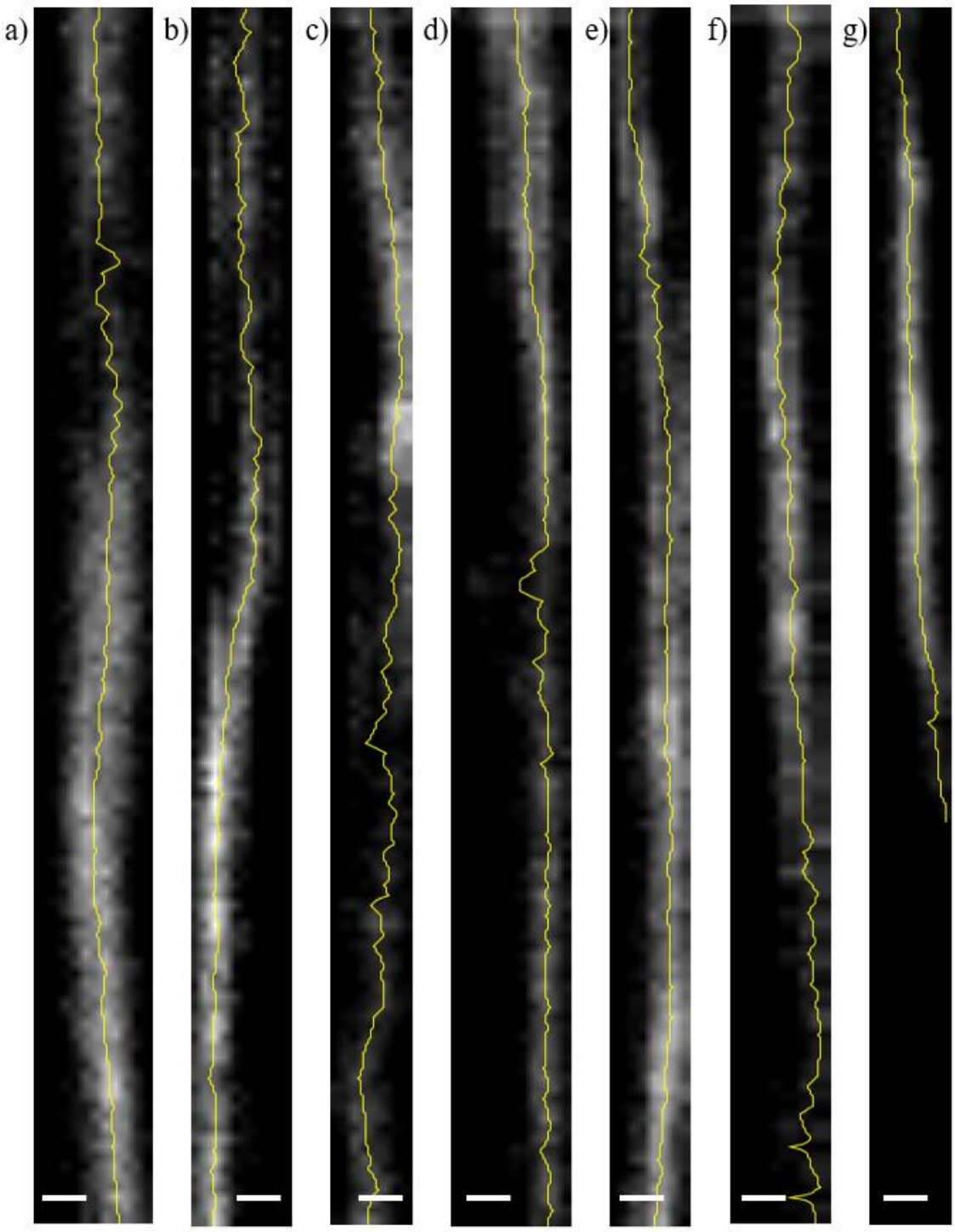


Figure 22 - Kymographs from R. sphaeroides cells under 2 µm in length with dynamic FtsZ. Centroid at each line marked and connected in yellow. Length: 240 seconds, Scale bar: 500µm

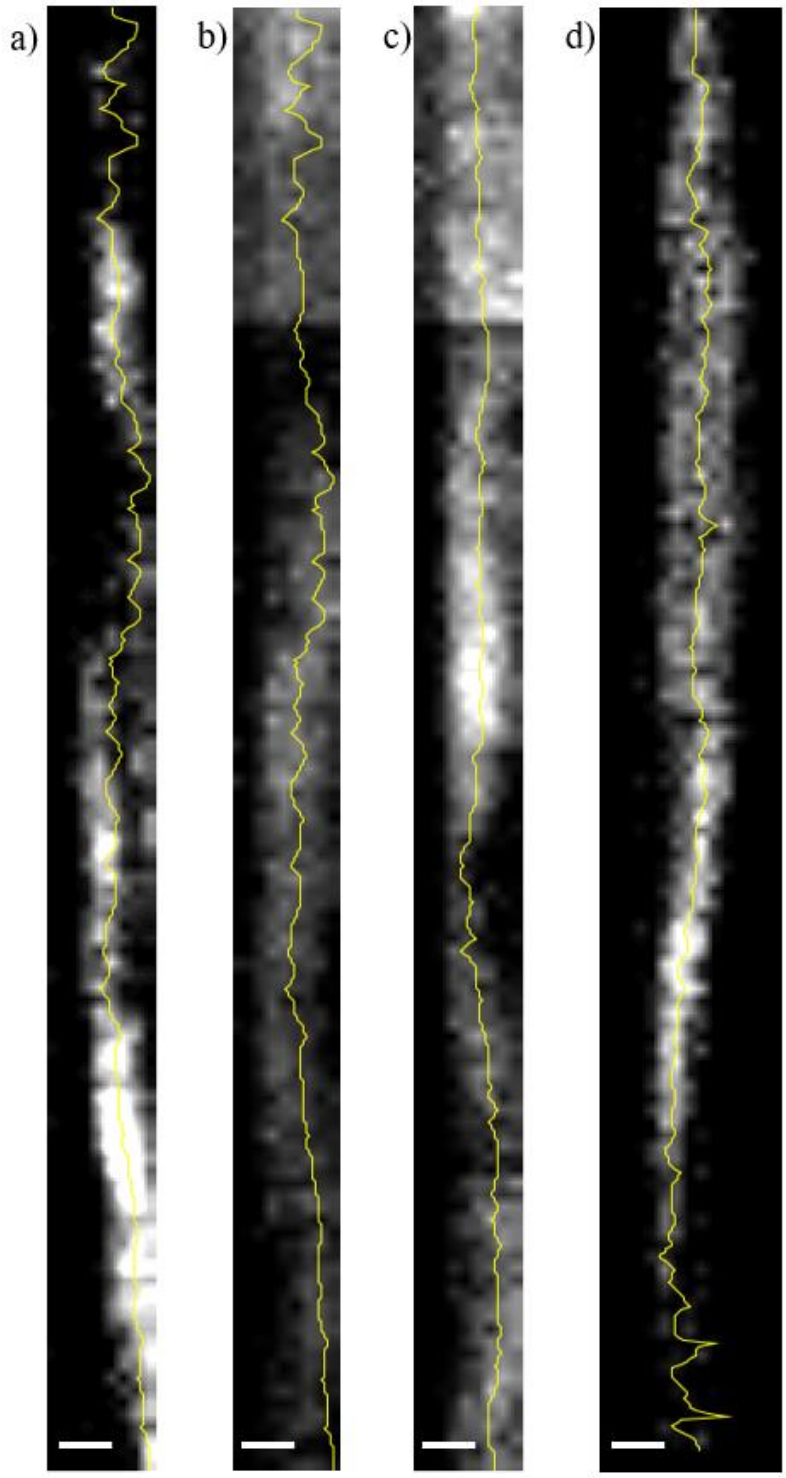


Figure 23 - Kymographs from R. sphaeroides cells between 2 and 2.5 µm in length with dynamic FtsZ. Centroid at each line marked and connected in yellow. Length: 240 seconds, Scale bar: 500µm

To investigate the velocity of FtsZ across the cell, the centroid of each line of the kymograph was used to calculate the velocity across the kymograph and these are shown in Figure 24 & Figure 25. Whilst these plots show velocities ranging from 0 to 12.28 nm/s, Figure 24 a) and f) stand out as profiles without a significant stationary population. In both of these results, the median velocity is recorded at 2.9 nm/s.

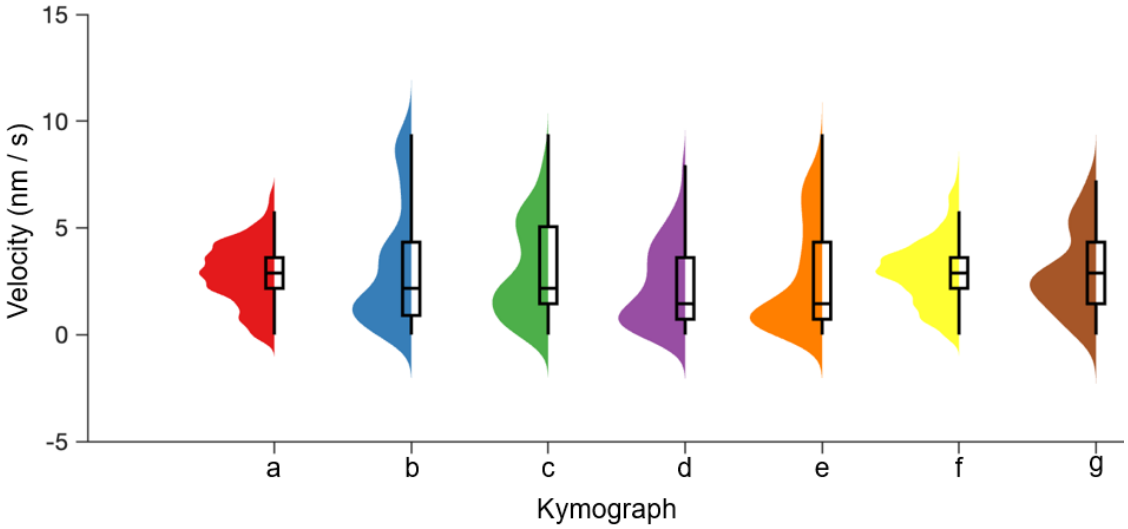


Figure 24 – Velocity profiles of dynamic FtsZ across kymographs in Figure 22 a-g. Boxes indicate interquartile range, with median whilst whiskers indicate 1.5x interquartile range.

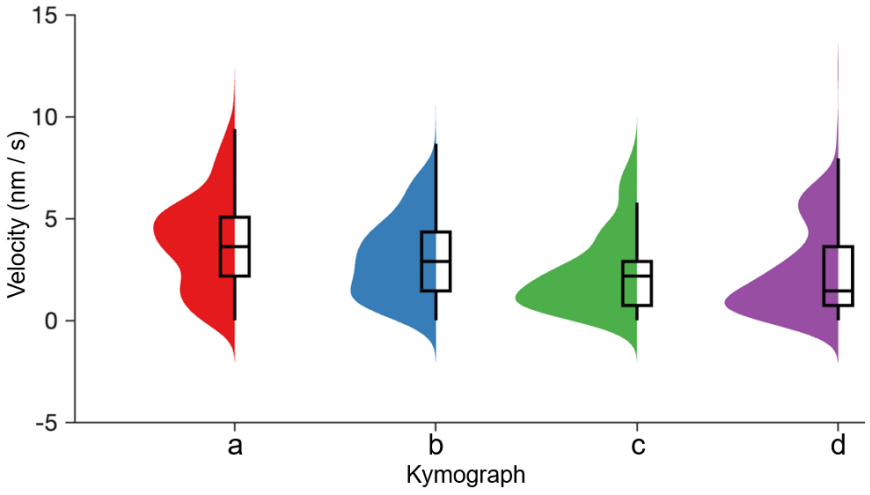


Figure 25 - Velocity profiles of dynamic FtsZ across kymographs in Figure 23 a-d. Boxes indicate interquartile range, with median whilst whiskers indicate 1.5x interquartile range.

3.3.5 MipZ Imaging

When imaging MipZ, the fluorescence levels using 52.5° illumination angle were very weak. Therefore, a less inclined illumination angle of 51° was used instead as previous work (Dubarry *et al.*, 2019) suggests that the MipZ ring is smaller and therefore further from the coverslip surface. This approach proved to be more successful and of the 721 cells images, 380 were observed to have significant levels of fluorescence. In these cells, MipZ was observed to be highly dynamic along the length of the cell but when an average value T-projection was formed by taking the average value of each pixel across the time series, three foci became clearer at the poles and mid-cell (Figure 26a). By plotting average relative intensity readings of these frames across the time series, as shown in Figure 26b, it is clear that labelled molecules are moving between these three locations: when one of the areas in the chart is at its maximum, one of the others is at a minimum. It also appears that the mid-cell foci become more dominant across the time series, suggesting that the MipZ concentration in the cell is moving from the poles to mid-cell.

To view the behaviour at a population level, cells were manually classified as having either no foci, foci at the poles only, foci at both mid-cell and poles or mid-cell only. 267 cells did not feature any foci but for the 113 which did, the cell length was measured as a proxy for lifecycle stage (See Section 1.2). When the cell lengths for each classification are plotted (Figure 26c), a clear pattern can be observed, where, as cells move through their lifecycle and grow, MipZ foci move from being exclusive to the poles, to both poles and mid-cell, and finally mid-cell only prior to division. A student t-test is used to show the statistically significant difference ($p < 0.05$) in cell length between the consecutive stages of this process. This is in agreement with Figure 26b and Dubarry *et al (2019)* where the model in Figure 7b shows MipZ ehibiting this behavior.

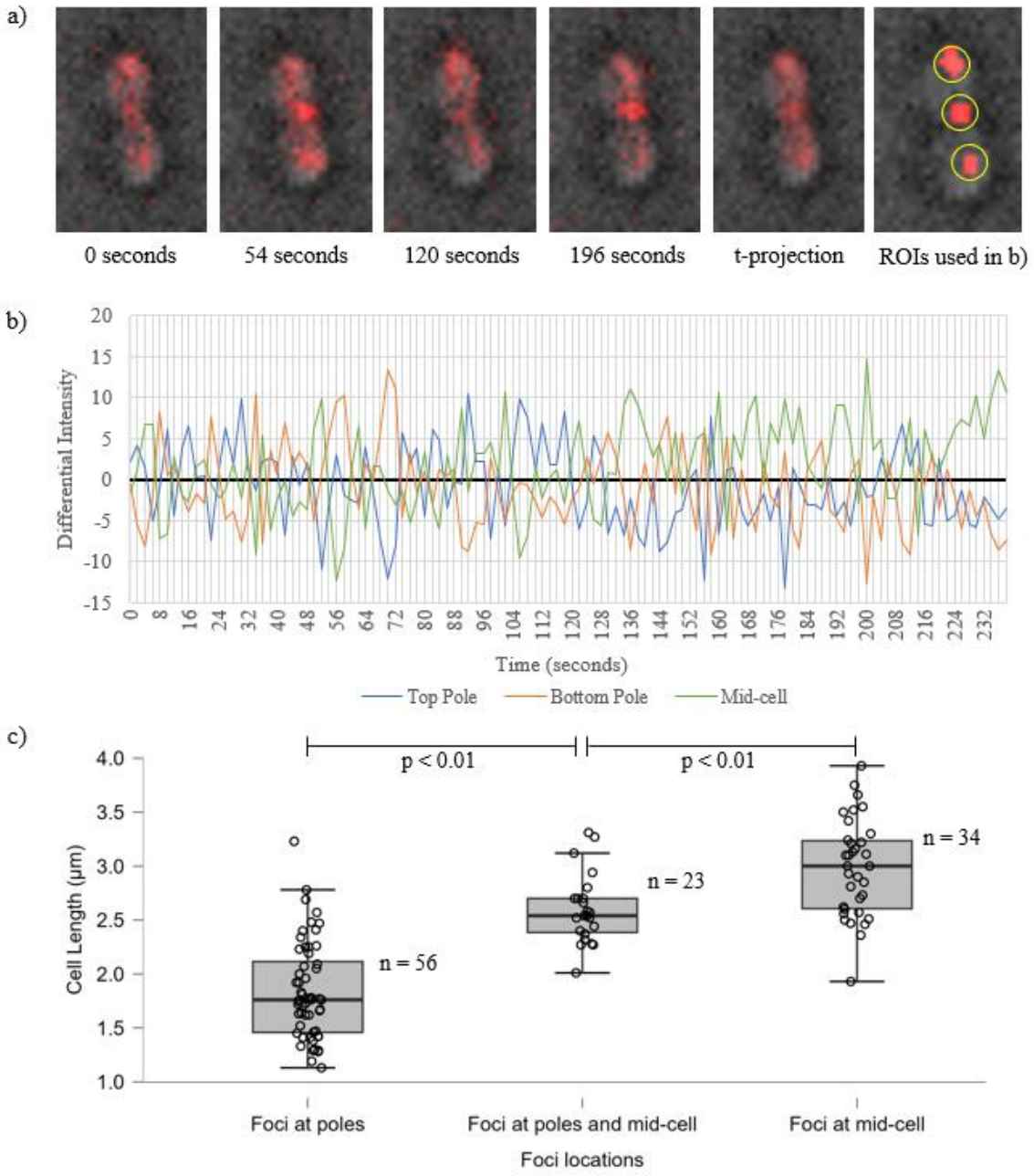


Figure 26 – MipZ imaging of R. sphaeroides. a) HILO images of SM0050 showing highly dynamic MipZ forming foci at both poles and at mid-cell at different time points, along with the average intensity t-projection showing the foci preset in all 3 locations. The right most image highlights the Regions of Interest (RoI's) analysed in (b) with a threshold of >3.35 % to highlight the foci locations. b) Intensity at top pole, bottom pole, and mid-cell relative to the average of all three at each time point. c) Boxplot with jitter of the lengths of 113 cells with foci at both poles only, both poles and mid-cell and mid-cell only. Boxes indicate interquartile range, with median whilst whiskers indicate 1.5x interquartile range.

3.4 DISCUSSION

In this chapter I imaged both MipZ and FtsZ separately using a labelling technique novel to *R. sphaeroides*. I found that SNAP-tag labelling system appears to be incompatible with to *R. sphaeroides* and observed dynamic behaviour in both MipZ and FtsZ, confirming findings of previous studies. A more detailed discussion of these findings is given below.

3.4.1 Snap-tag labelling

The binding of the SNAP-tag ligand to a native *R. sphaeroides* protein was an unexpected result and one which raises some interesting possibilities.

The reason for the SNAP-tag to behave differently in WS8N to any other strain remains unclear. There is a strong degree of similarity between the structural predictions for both *F. johnsoniae* where SNAP-tag has been shown to work and WS8N but there are some differences, particularly in the disordered regions which could explain the difference in behaviour. Mollwitz *et al.*, (2012) demonstrated how the human DNA repair protein O6-alkylguanine-DNA alkyltransferase (hAGT) was mutated through directed evolution to create SNAP-tag which has 52 fold higher reactivity with BG derivatives such as the SNAP-tag ligand. The area covered by Table 10 is conserved in all of the mutations shown, meaning it sheds no lights on whether these differences are the likely cause of the change in binding behaviour.

Whilst there is compelling evidence to suggest that SNAP-tag is binding to Methylated-DNA-protein-cysteine methyltransferase, further work could be carried out to get further clarity on this. In Figure 18, a control of the wild type WS8N+pIND with no dye should have been completed as part of this experiment, to prove that this band is not the result of an auto-fluorescent native protein. The next logical step would be to cut out this band from the gel and send it for analysis by mass spectrometry to ensure the identity of the protein is correct. Isothermal Titration Calorimetry could be used to assess the binding properties of this protein from different species with the SNAP-tag ligand and compare the results. Further microscopy could also be carried out

to quantify the diffusion speed of the molecule, and track its trajectory around the cell using software such as trackpy (Allan *et al.*, 2024).

3.4.2 Labelling Efficiencies

Looking at the number of cells exhibiting fluorescence and the behaviour of those cells which exhibited fluorescence, the labelling efficiency using HaloTag appears to be very low. I was only able to detect fluorescence from 36% of FtsZ labelled cells and 52% of MipZ labelled cells. This suggests that in the cells with fluorescence, it is highly unlikely that all the molecules have been labelled. In MipZ, the weak signal levels observed in the foci, and the fact that foci were not present in all frames, suggests that only a few molecules were actually labelled, despite every MipZ molecule being tagged with the HaloTag protein. Given that this is to the best of my knowledge, the first time HaloTag has been used with an α-proteobacteria, it is likely that this labelling system is not very compatible with *R. sphaeroides*.

For FtsZ, the problem is twofold, as this protein cannot be labelled genomically and therefore relies on labelling those few FtsZ-Halo molecules expressed from the plasmid. It is therefore unsurprising that a lower proportion of cells in the FtsZ experiment exhibit fluorescent foci.

3.4.3 Imaging modality

In this chapter for work it was intended that all of the FtsZ imaging would be carried out using TIRF illumination. However, following the completion of these experiments, I learned that the objective on the NanoImager (ONI) in the Micron Facility at the University of Oxford has an NA of 1.4, making it unsuitable for TIRF. This was not expected as I had been informed by Micron staff, the Micron website (Micron Oxford, 2021) and the colleague who instructed me on how to use the system that this NanoImager was suitable for TIRF illumination.

Whilst a 1.4 NA objective would make TIRF theoretically possible, in all practical terms it is not realistic to achieve this, and a 1.45 NA objective is needed.

3.4.4 FtsZ Dynamics

The results presented in this chapter clearly demonstrate that FtsZ in *R. sphaeroides* is concentrated at mid-cell in the later stages of the cell cycle. They also provide strong evidence of dynamic behaviour of FtsZ foci as reported in Chiu *et al.*, (2013). As the cell elongates, these move to mid-cell and movement around the circumference of the cell can be observed. Whether this is a single spot moving round the circumference or a treadmilling process is less clear. Kymographs of treadmilling behaviour should display a series of parallel diagonal lines, where the angle indicates the velocity of treadmilling. These are created by labelled FtsZ molecules moving across the profile. This is not the case in Figure 22 and Figure 23 where lines slowly oscillate or bend down the length of the kymograph.

If this is treadmilling, the velocity of 2.9 nm/s recorded is much slower than that of *E.* coli where treadmilling velocities of 37 nm/s have been logged (Bisson-Filho *et al.*, 2017). Due to the substantially different doubling times of these organisms however; 20 minutes for *E. coli* and 3 hours for *R. sphaeroides*, (Duggan, Parker and Phillips-Jones, 2000; Gibson *et al.*, 2018) this is unsurprising.

Unfortunately, dynamic behaviour at mid-cell once constriction began could not be observed, likely due to the limitations of the experiment. Given the behaviour in other strains (Bisson-Filho *et al.*, 2017; Wagstaff *et al.*, 2017; Whitley *et al.*, 2021), FtsZ treadmilling behaviour would not be surprising, however this has yet to be observed in any of the alphas (Lariviere and Goley, 2022), even though it is assumed to be the case in some studies (Corrales-Guerrero *et al.*, 2022).

Due to the issues around labelling efficiencies and illumination highlighted above, it is hard to draw further conclusions from the present work, as it is difficult to precisely assess what is being observed. The apparent shifts in location of foci observed in the kymographs could be due to several labelled molecules treadmilling and shifting the foci location as one binds to the leading end of the filament, and another unbinds from the training end. Alternatively, this could simply be a single labelled molecule slowly diffusing around the cell.

Clearly the next step would be to repeat the same experiment with a bright photostable fluorescent protein such as mNeonGreen and using a microscope capable of TIRF. In TIRF, only the FtsZ closest to the coverslip would be visible, meaning that all of the treadmilling would occur in the same direction in the plane of the coverslip. This will make the data much easier to analyse. Treadmilling would be observed as labelled FtsZ molecules join the leading edge within the field of illumination. As the leading-edge advances across the cell, the leading-edge position can be tracked, allowing the rate of treadmilling to me measured. The same can then be done for the trailing edge.

A higher frame rate should be attempted to observe dynamics with higher temporal resolution.

Imaging the cell end-on with a microfluidic support using the VerCINI system developed by the Holden lab (Whitley *et al.*, 2022) would also be a good way to assess whether there is treadmilling behaviour for both FtsZ and MipZ, particularly once constriction has started to occur.

3.4.5 MipZ Observations

Forming a ring at mid-cell was unexpected behaviour when it was observed in previous work (Dubarry *et al.*, 2019) and was not observed previously in other species (Thanbichler and Shapiro, 2006b; Toro-Nahuelpan *et al.*, 2019). Whilst I was unfortunately unable to test the hypothesis that MipZ is treadmilling, I was able to confirm that MipZ forms foci at mid-cell prior to division and at the poles in the earlier stages of the cell cycle. Since the foci are only present in some images, it suggests that labelled MipZ molecules are highly dynamic, but bind for short periods at the cell poles and at mid-cell. These periods at the left of Figure 26b are under 2 seconds (sampling period) but towards the right of Figure 26b as time progresses, these periods extend to beyond 16 seconds. It is likely that what is observed in this work is MipZ monomers, binding at the poles, dimerizing and then binding at mid-cell, before unbinding again to form monomers. The longer binding time at mid-cell in the later stages of the experiment could be as a result of a MipZ structure forming at there.

What the MipZ dimers bind to at mid-cell is still unclear, however, a more recent study (Corrales-Guerrero *et al.*, 2022) shows that MipZ dimers in *C. crescentus* bind to the C-terminal domain of FtsZ filaments, capping the leading end, preventing further binding and ultimately leading to depolymerisation as a result of continued unbinding at the trailing end. In *C. crescentus*, MipZ dimers do not form a ring-like structure at mid-cell, so the mechanism is likely to be slightly different. However, this finding provides a good starting point for further investigation.

The next step would be to conduct a similar imaging experiment with a higher frame rate under single molecule conditions by using a photoactivatable dye. Single molecules could then be tracked, measuring their diffusion rates at different locations to check for binding. Cells could also be imaged end-on (Whitley *et al.*, 2021) and then checked for treadmilling using single molecule tracking.

The structure of MipZ in *R. sphaeroides* could also be compared to that of MipZ in *C. crescentus* to see if there are substantial changes to the C-domain where FtsZ is binding. Further to that, the FtsZ-MipZ complex could be purified and the Hydrogen/Deuterium eXchange Mass Spectrometry (HDX-MS) experiments in Corrales-Guerrero *et al.* (2022) could be run on this system to highlight areas which are not exposed following MipZ-FtsZ binding.

4 *IN VITRO* EXPERIMENTS

Designed to complement the *in vivo* imaging in Chapter 3, this chapter focusses on experiments conducted to observe the behaviour of the proteins MipZ and FtsZ *in vitro*. This allows the concentration of MipZ and its mutants to be varied, allowing investigation of its role in controlling FtsZ polymerisation. To allow me to perform these experiments, I modified expression plasmids, and used them to produce and purify wild type and mutant variants of FtsZ and MipZ.

4.1 INTRODUCTION

Whilst conducting experiments *in vivo* is always preferable, some experiments simply are not possible within the confine of the cell. One *in vitro* experiment which can be conducted when investigating MipZ and FtsZ is a sedimentation assay (Thanbichler and Shapiro, 2006b; Goley *et al.*, 2010; Sundararajan *et al.*, 2015; Toro-Nahuelpan *et al.*, 2019). These assays allow one to quantify the amount of protein which has formed higher order polymers, in this case FtsZ. This type of experiment works by the principle that high order polymers are heavier than low order polymers or monomers, and therefore these high order polymers sediment more quickly. The polymers in the pellet are then broken down into monomers by an SDS running buffer, resulting in more monomers present for proteins which had a higher degree of polymerisation, and therefore a darker band in the SDS-PAGE gel. Because the experiment is taking place *in vitro*, conditions which would normally prevent cell growth can be tested, such as only having a MipZ mutant present.

In this chapter I aim to:

- Investigate whether MipZ is capable of forming higher ordered structures in the absence of FtsZ, and if these structures exist, whether they form exclusively by the MipZ dimer or both monomer and dimer.

- Investigate if the monomer-locked variant of MipZ is binding to FtsZ polymers confirming what was observed *in vivo* in Dubarry et al., 2019.
- Verify that MipZ is limiting FtsZ polymerisation, and that it is only the dimer exhibiting this behaviour, confirming what was observed *in vivo* in Dubarry et al., 2019.
- Confirm that ATP and GTP are required for dimerization of MipZ and polymerisation of FtsZ, respectively.

4.2 Materials and Methods

4.2.1 Buffers for protein purification

The buffers used are listed in Appendix 7.1. Where buffers differ from those listed, the change will be made clear in the results section.

4.2.2 Protein Expression Strains

For the expression of MipZ, MipZ G12 and MipZ D40, strains have been created previously, which use the expression plasmid pet303 in the BL21 strain of *E. coli*. These cells expressed MipZ or one of its mutants with a non-cleavable 6xhis tag attached to the C-terminal of the protein. This strategy is described in Thanbichler and Shapiro (2006b).

For FtsZ, no expression strain existed. Using Gibson assembly, I inserted FtsZ into the expression vector pet15B with a TEV cleavable N-terminal 6xhis tag to create the plasmid pSM0004. This was transformed into *E. coli* strain BL21 to create strain SM0015. Later the same plasmid was transformed into Rosetta2 *E. coli* to create SM0021.

The details of each of the proteins that were produced are listed in Table 11.

Protein	Description	Length (Amino Acids)	Estimated molecular weight (kDa)	Estimated isoelectric point (pI)
6xhis-TEV-FtsZ	Wild type FtsZ from WS8N with an N-terminal 6xhis tag and TEV cleavage site	567	60.5	4.94
FtsZ	Wild type FtsZ from WS8N	552	58.7	4.66
MipZ WT-6xhis	Wild type MipZ from WS8N with C-terminal 6xhis tag	278	30.8	6.97
MipZ G12-6xhis	Monomer locked MipZ mutant	278	30.8	6.97
MipZ D40-6xhis	Dimer locked MipZ mutant	278	30.8	6.97

Table 11 – Summary of strain information

4.2.3 Protein Expression and lysis

The protein expression and lysis method used was adapted from Thanbichler and Shapiro, 2006b. Cultures were started in 2 L baffled conical flasks with 500 ml of LB + Amp using overnight cultures grown from single colonies to an OD_{600} of 0.05. Cultures were incubated at 37°C in a shaking incubator (180 rpm, 2" stroke) and grown to OD_{600} 0.6 which took around 2 hours. After 2 hours, cells were induced using IPTG to a final concentration of 0.5mM and incubated overnight with the temperature reduced to 20°C.

Cultures were decanted into 1L centrifuge bottles and spun down at 7500xg for 10 minutes before the supernatant was poured off, and resuspended in FtsZ or MipZ lysis buffer at a volume of 7 ml/g of pellet. The culture was homogenised in a Dounce homogeniser before running the sample through the cell disruptor (Constant Systems) at a pressure of 30 kPSI twice at 4°C with the collection bottle sat in ice.

4.2.4 Protein Purification

The method used for protein purification was adapted from Thanbichler and Shapiro, 2006b. After the cell lysate was spun down at 38,400 xg for 1 hour at 4°C, the supernatant was filtered through a 0.45 µm syringe prior to being pumped through a Ni Sepharose (HisTrap FF, Cytiva) column on loop overnight using a peristaltic pump (AgnThos) at 4°C.

The column was eluted using the protocol for gradient elution included in Appendix 7.2 with UV concentration detection (ÄKTA, Cytiva). Buffer A was FtsZ / MipZ buffer and buffer B was FtsZ/MipZ Elution Buffer. Fractions were collected and ran on an SDS-PAGE gel for analysis.

Selected fractions containing the protein of interest were dialysed overnight at 4°C into FtsZ / MipZ buffer to reduce imidazole concentration.

Dialysed protein was subsequently concentrated to 5ml volume using a centrifugal concentrator (Amicon Ultra, Millipore) with a molecular weight cut-off (MWCO) of 10kDa for MipZ and 50kDa for FtsZ. The concentrated protein was then injected onto a Size Exclusion Chromatography column (HiLoad 16/60 Superdex 75, Cytiva), initialised with FtsZ / MipZ buffer, and ran using the protocol detailed in Appendix 7.4 with UV detection (ÄKTA, Cytiva). Fractions were collected and run on SDS-PAGE gel, followed by Western Blot for analysis.

If protein was to be stored, selected fractions of MipZ were dialysed overnight into MipZ storage buffer before, like FtsZ, being plunge frozen in aliquots of 100 µL and stored at -80°C.

4.2.5 TEV Cleavage

To remove the 6xhis tag from the N-terminal of FtsZ and restore functionality, the purified protein was cleaved at the TEV protease recognition site, indicated by the red arrow in Figure 27.

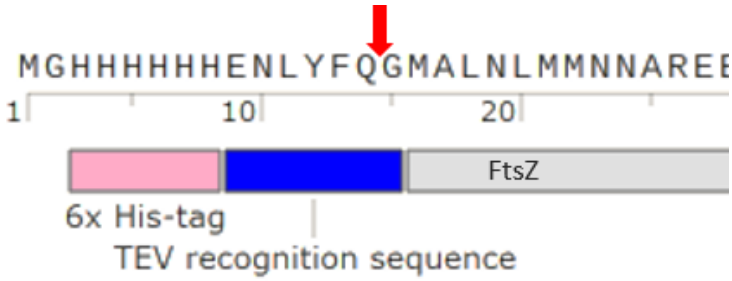


Figure 27 – Start of 6xhis-TEV-FtsZ Amino Acid Sequence. Created using: SnapGene software (www.snapgene.com)

Protein concentration was quantified using a UV spectrophotometer (NanoDrop 2000, Thermo Scientific) and for every 15 µg of protein, 5 µL TEV Buffer (New England Biolabs) and 1 µL

TEV Protease (New England Biolabs). H_2O was added to make the reaction up to 45 µL. The mixture was then incubated at room temperature for 1 hour.

As both the TEV protease and the cleaved protein contained 6xhis tags, these were removed with a gravity column with Ni-NTA Agarose beads (QIAGEN). First the column was washed with 70% ethanol, H_2O and FtsZ buffer. An appropriate amount of bead solution was then deposited into a 10 ml Falcon Tube, washed and pelleted by centrifugation at 3500 xg twice with water and once with buffer before being resuspended in protein solution and incubated on rotary mixer at 4°C.

The mixture was then transferred to the cleaned gravity column, and the flow-through, which should contain the untagged FtsZ, was collected. The column was then washed with FtsZ buffer and then eluted with FtsZ Elution buffer. Flow-through, wash material and elution were analysed by SDS-PAGE to ensure effective cleavage.

4.2.6 Sedimentation Assay

The sedimentation assay was adapted from Toro-Nahuelpan et al., 2019. FtsZ samples were thawed on ice and dialysed into MipZ storage buffer overnight at 4°C. GTP and ATPγS, a non-hydrolysable ATP analogue, were diluted in MipZ buffer without glycerol. Sample concentration was measured using a UV Spectrophotometer (NanoDrop, Thermo Scientific) and samples were combined in a centrifuge tube according to experimental plan as listed in Table 12, with volumes and levels of glycerol normalised across all samples. The reaction was mixed by pipetting up and down, and samples were then incubated for 15 minutes at room temperature before being spun down at 368,600 xg for 15 minutes (Optima-XP, Beckman Coulter) at 20°C. Tubes were removed and the supernatant was removed carefully to avoid disturbing the pellet.

The pellet was resuspended in 250 µL in 1x SDS loading buffer with DTT, transferred into a microcentrifuge tube and boiled for 5 minutes. Samples were run on an SDS-PAGE gel and results were analysed.

4.3 RESULTS

4.3.1 Purification issues with FtsZ

When running *in vitro* experiments such as sedimentation assays, it is essential to have pure and homogeneous protein samples, so the effects can be correctly attributed to the proteins being studied. When purifying FtsZ, two bands appeared on the gel in Figure 28a, which both also bound to the α-6xHis tag antibody in the Western blot in Figure 28b. Whilst two bands have been observed *in vitro* for FtsZ in other studies (Toro-Nahuelpan *et al.*, 2019), this finding nonetheless warranted further investigation. After repeating the expression and purification steps, the same two bands were observed and the lower one was sent for sequencing by Liquid Chromatography with tandem mass spectrometry (LC-MS-MS). The results showed that the protein was missing a large section of the C-terminal end, as shown in red in Figure 29. The complete section of this protein is estimated to be 48 kDa which is approximately its position on the gel.

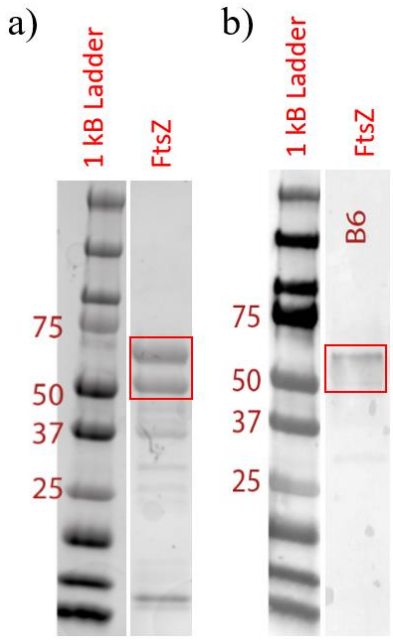


Figure 28 – a) SDS-PAGE gel and b) Western blot using α 6xHis tag (MA1-21315, Invitrogen) of 6xHis-TEV-FtsZ following elution from Ni affinity column. FtsZ highlightd by red box. Ladder: Dual Colour 1kB ladder, BioRad.



Figure 29 – Sequence of 6x His-TEV-FtsZ with the section identified as missing highlighted in red.

Two possible reasons for this observation are that the protein may have been cleaved by an enzyme, or that this was a result of insufficient levels of some transfer Ribonucleic acids (tRNA) in the BL21 cell line to translate the entire protein for every copy. To check for possible causes of cleavage, the amino acid sequence was run through Peptide Cutter (https://web.expasy.org/peptide_cutter/), but no single cutting site enzymes were identified for the final amino acid F451. To mitigate against the risk of low copy number tRNA's, pSM0004 was transformed into *E. coli* cell line Rosseta2 to create SM0021 as this features a larger array of tRNA's.

To test the effect of the change in cell line, and optimise growth conditions, small scale protein expression was performed by growing 50 ml of SM0021 and SM0015, and inducing the SM0021 at different points and for different lengths of time at different temperatures. 1 ml of culture at normalised to OD_{600} 1 was taken, boiled and loaded onto an SDS-PAGE gel as shown in Figure 30a. The results indicate that there is little difference between any of the strains or conditions, with none of them exhibiting the extra band at approximately 48 kDa. To test this further, the

same growth protocol was followed, and SM0021 cells were lysed in 3 different buffers using an ultrasonic probe (50% power for 5 minutes with 10s/10s on/off pulses). Samples of the supernatant and pellet were run on an SDS-PAGE gel as shown in Figure 30b. Lysis buffer conditions also appeared to make no difference to the sample.

Following these tests, a full expression and purification protocol (see 4.2.3 and 4.2.4) was run using SM0021, before the TEV cleavage protocol (see 4.2.5) was performed on the purified protein. The purified protein sample had some degraded product in there but not at the quantities which were observed previously. All of this suggests that the presence of the lower molecular weight band is a function of a later step in the purification process rather than being the result associated with the cell line or lysis buffer conditions.

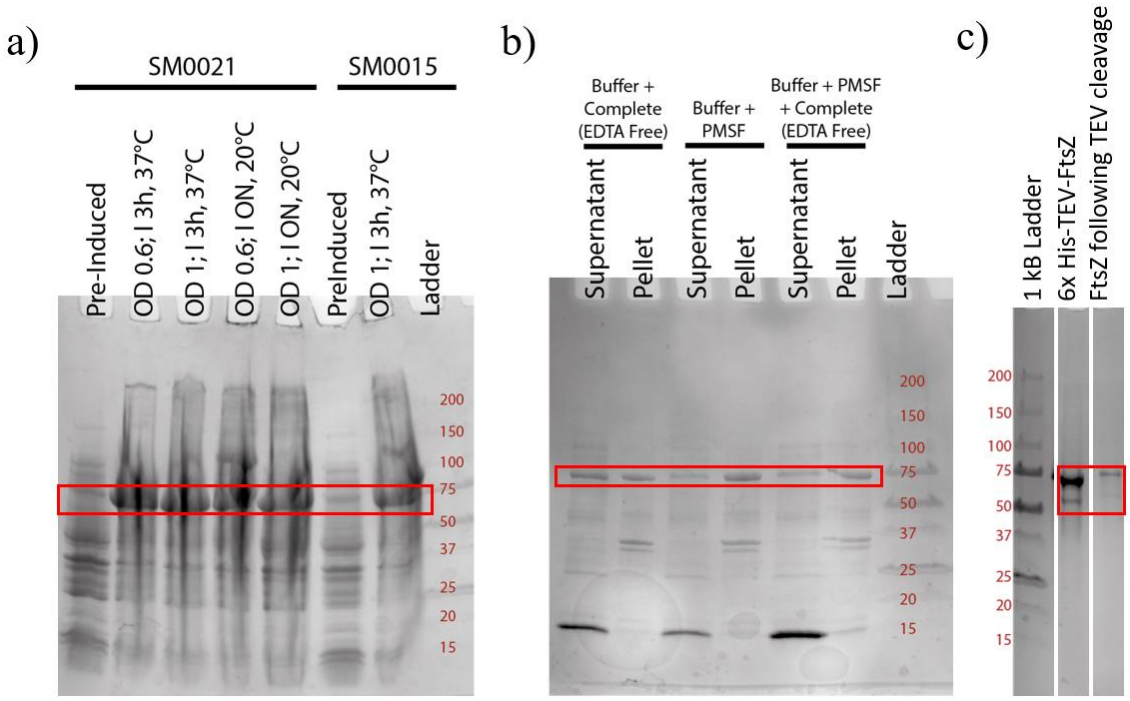


Figure 30 – SDS-page gels with FtsZ highlighted in red box showing: a) SM0021 and SM0015 strains grown under different conditions. OD is the OD_{600} value at which the cells were induced, 3h / ON indicates whether the culture was induced for 3 hours or overnight, and the temperature indicates the temperature the cells were induced at. b) Supernatant and pellet samples from SM0021 lysis using different lysis buffer conditions. c) Result of full preparation before and after TEV cleavage. Ladder: Dual Colour 1kB ladder, BioRad.

4.3.2 Sedimentation Assays of MipZ and FtsZ

To address the questions posed in 4.1, an experimental plan was developed (Table 12) to test different combinations of MipZ (and its mutants), FtsZ, ATPγS and GTP. Experiments were grouped into 10s to fill one centrifuge rota.

The resulting gel images are faint and difficult to interpret, however there is enough signal to make some observations. Firstly, it would be expected that a darker band was present for reaction 2 when compared to reaction 1, as GTP is present in reaction 2. Unfortunately, in both gels, the band in reaction 2 is lighter than that of reaction 1, indicating that there is a problem with the experiment. For MipZ, there should be no substantial difference caused by the presence of ATPγS, as it is likely the highest order structure formed by MipZ is a dimer. The fact there is no significant difference in band intensity between Reaction 3 and 4 could be an indicator that MipZ is not capable of forming polymers alone, however more work is required to investigate this hypothesis. Quantities of materials were based on Toro-Nahuelpan et al., 2019.

Concentration in µM	FtsZ	MipZ WT	MipZ G12	MipZ D40	ATPyS	GTP	Justification
Reaction 1	3				1000		-CTRL for FtsZ and is FtsZ polymerisation dependent on presence of GTP?
Reaction 2	3				1000	2000	
Reaction 3		3				2000	-CTRL for MipZ and is MipZ forming higher order structures without FtsZ?
Reaction 4		3			1000	2000	
Reaction 5			3			2000	-CTRL for MipZ monomer locked and is MipZ forming higher order structures without FtsZ?
Reaction 6			3		1000	2000	
Reaction 7				3		2000	-CTRL for dimer locked, and is this capable of showing higher order structures without MipZ?
Reaction 8				3	1000	2000	
Reaction 9	3	3			1000	2000	This combination should reduce FtsZ in the pellet
Reaction 10	3		3		1000	2000	Has this combination resulted in less FtsZ in the pellet and how much MipZ G12 has been co-sedimented with it? This would indicate that MipZ Monomers in the ring at mid-cell
Reaction 11	3			3	1000	2000	Has this combination resulted in less FtsZ in the pellet and how much MipZ D40 has been co-sedimented with it?
Reaction 12	3	1			1000	2000	Confirming the relationship between MipZ concentration and FtsZ polymerisation
Reaction 13	3	2			1000	2000	Confirming the relationship between MipZ concentration and FtsZ polymerisation
Reaction 14	3	3			1000	2000	Confirming the relationship between MipZ concentration and FtsZ polymerisation
Reaction 15	3	4			1000	2000	Confirming the relationship between MipZ concentration and FtsZ polymerisation
Reaction 16	3	5			1000	2000	Confirming the relationship between MipZ concentration and FtsZ polymerisation

Table 12 - Sedimentation Assays plan.

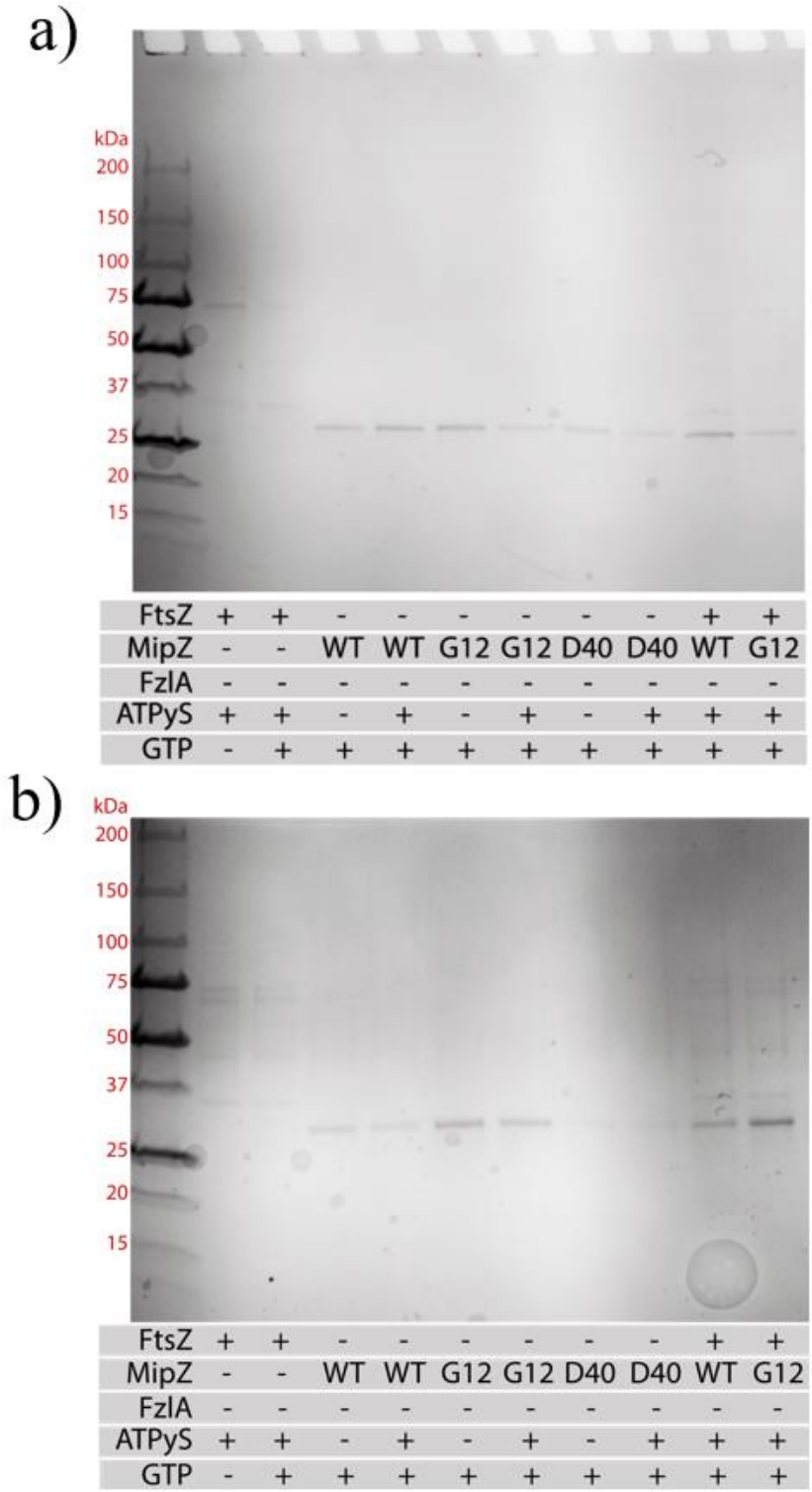


Figure 31 - a) and b): Repeats of the SDS-PAGE gel from the sedimentation assays detailed in Table 12. Ladder: Dual Colour 1kB ladder, BioRad.

Following these repeats, more protein was required, but during the next round of purification, problems with MipZ D40 also became apparent. Multiple bands formed around 30kDa as shown in Figure 32a, but this behaviour Figure 32 is unexpected with only one of the lanes indicating the protein has bound to the α 6xHis tag (MA1-21315, Invitrogen) used.

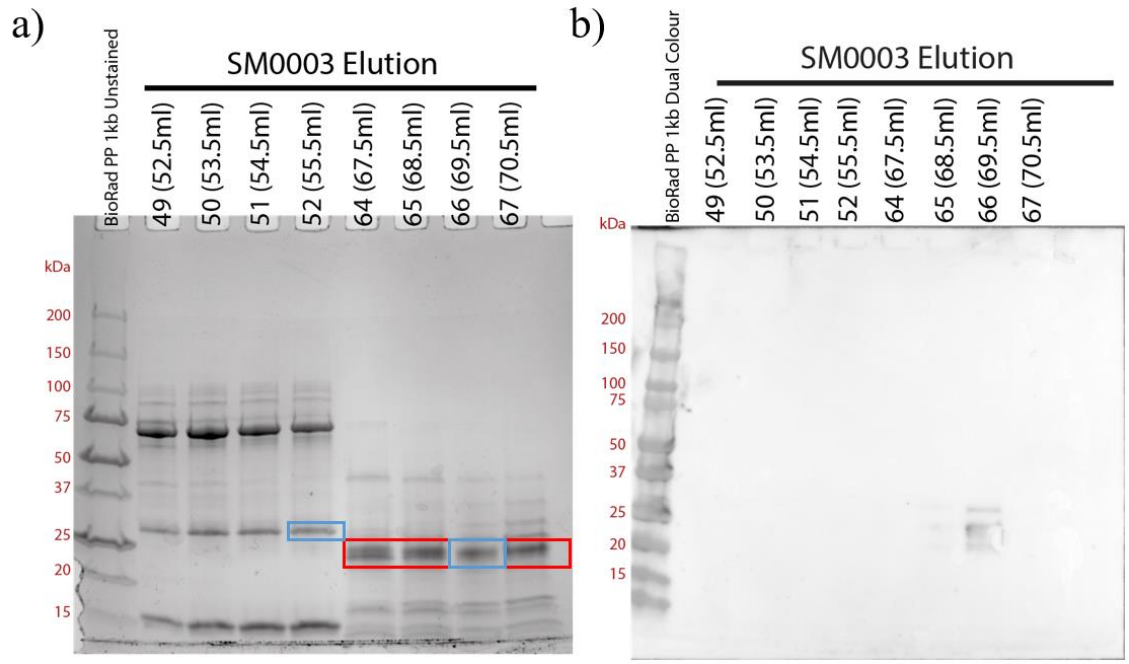


Figure 32 - a) SDS-PAGE gel with suspected MipZ bands highlighted in red and bands sent for LC-MS-MS analysis in blue. b) Western blot using α 6xHis tag (MA1-21315, Invitrogen) of MipZ-6xHis. Ladder: Dual Colour 1kB ladder, BioRad.

Following LC-MS-MS analysis of the bands highlighted in blue in Figure 32 revealed that the band in fraction 52 comprised of only *E. coli* proteins and in fraction 66, some MipZ D40 was detected but high levels of *E. coli* were also detected.

Due to this issue and the likely problem with the FtsZ sample indicated by the lack of polymerisation in the presence of GTP, the decision was taken to stop this work here and focus on other areas of this DPhil project.

4.4 DISCUSSION

4.4.1 Double FtsZ band

Figure 28 shows that two bands are present when FtsZ from *R. sphaeroides* is purified, which is consistent with the findings of Toro-Nahuelpan et al., (2019) in *M. gryphiswaldense*. They state that this is due to "a long unstructured C-terminal region that is very prone to proteolysis" (Personal communication, M. Thanbichler). This would be a logical explanation for the 2nd band observed this study due to the similar size differences between the bands in both studies.

4.4.2 Reflections and further work

The main result from the work described in this chapter is the small indication that MipZ cannot form a ring alone. Unfortunately, the lack of pure protein samples held back this work and were I to attempt this again, I would aim to speed up the purification process and focus less on getting the largest possible yield. A way to speed up the purification protocol would be running the sample over the column for a shorter period and trying to reduce the required number of dialysis steps. Not only would doing this speed up the process, allowing more conditions to be tested, but this would also limit the time the protein is exposed to unusual conditions such as those found in the Ni affinity column.

To gain further insight into the behaviour of MipZ, the incubated mixtures of MipZ and FtsZ could be imaged with a transmission electron microscope using the protocol in Toro-Nahuelpan *et al.*, 2019. This would not only provide an orthogonal method for verifying the existence of FtsZ polymers with different concentrations of MipZ, but it would also allow quantification of the chain length.

Further understanding could then be gained using Hydrogen-Deuterium-eXchange Mass Spectrometry (HDX-MS) which has been used in other studies to detect the binding regions of two proteins (Corrales-Guerrero *et al.*, 2020, 2022). It could be that MipZ is able to bind to FtsZ

in two places, one to form the ring-like structure, and another to perform the filament capping role which causes FtsZ filament degradation (Corrales-Guerrero *et al.*, 2022).

To obtain more knowledge on the polymer structures being formed, a native technique such as Mass Photometry (Young *et al.*, 2018) could be used to quickly quantify the lengths of each polymer by measuring each assembly's mass on a single particle basis. The 30kDa mass of the MipZ monomer is at the limit of detection for a commercially available mass photometer (Two^{MP}, Refeyn), however, the dimers and everything above this size would be well resolved.

5 MICROSCOPE BUILDING

5.1 INTRODUCTION

5.1.1 Objective

Structured illumination microscopy (SIM) and Solid Immersion Fluorescence (SIF) are two techniques which have been developed to increase the spatial resolution of fluorescence imaging. Whilst the characteristics of these two techniques and their relative advantages when compared to other super-resolution techniques such as PALM, STORM and STED are well aligned, therefore making them a potentially useful partnership. Neither technique requires single molecule fluorescence, which means that standard fluorophores can be used. Furthermore, neither requires high illumination intensities which can cause phototoxicity in live samples, and both techniques are theoretically compatible with live cell imaging as only a single frame in SIF and 9 frames in SIM are required to produce a single image. The 9 frames required to create one SIM frame, are made up of 3 orientations of 3 phase steps which are required to reassign the information captured from the three Fourier space components (see 5.1.2).

The disadvantage of both techniques is that the improvement in spatial resolution is modest when compared to techniques like PALM or STORM. This disadvantage can be ameliorated slightly by combining SIM with a Solid Immersion Lens (SIL): this setup has been shown to provide a 2x resolution enhancement when compared to a widefield fluorescence system with a 1.45 NA objective (Wang, 2010). However, this resolution enhancement was only demonstrated on a fixed non-biological sample of fluorescent beads. This aim of this work was to create an optimised, multi-colour channel live cell compatible SIM/SIL microscope, through an enhanced SIL design, through use of a spatial light modulator and improved SIL mounting.

5.1.2 Structured Illumination Microscopy Theory Overview

SIM works by doubling the bandwidth of frequencies detectable by the microscope. In a widefield microscope, the image generated *D(r)* is the result of the convolution of signal from the sample *E(r)* and the Point Spread Function (PSF) H(r) of the optical system.

$$D(r) = E(r) \otimes H(r) \qquad \textit{Equation 13}$$

The Fourier transform of the PSF is the Optical Transfer Function (OTF) *O(k)*, therefore Equation 13 becomes the following in Fourier (k) space:

$$\tilde{D}(k) = \tilde{E}(k)O(k) \qquad \textit{Equation 14}$$

This means that spatial frequencies are attenuated according to the OTF and those that fall outside of the OTF are not seen in the image. This effect is illustrated in Figure 33.

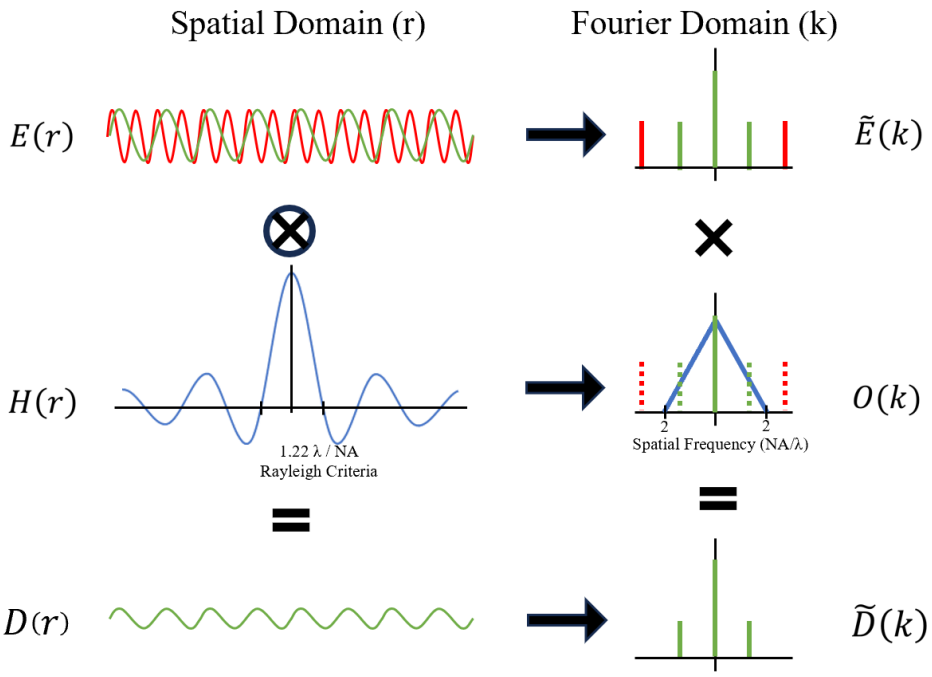


Figure 33 - High frequency (red) and low frequency (green) signals present in the sample are imaged by the microscope optical system, represented by the PSF in the spatial domain and the OTF in the Fourier domain. The signals are convolved and multiplied by the PSF and OTF respectively to give the imaged output. Only the low frequency signal is within the bandwidth of the microscope and is therefore visible in the output image. However, the remaining signal is at a reduced amplitude.

In fluorescence microscopy, the signal from the sample *E(r)* is composed of the illumination intensity distribution *I(r)* and the distribution of fluorophores in the sample *S(r)*. This means that:

$$E(r) = S(r)I(r)$$ *Equation 15* (Hall and Dobbie, 2022)

And in the Fourier domain:

$$\tilde{E}(k) = \tilde{S}(k) \otimes \tilde{I}(k)$$ *Equation 16* (Hall and Dobbie, 2022)

By substituting Equation 16 into Equation 14:

$$\widetilde{D}(k) = O(k)\left(\tilde{S}(k) \otimes \tilde{I}(k)\right)$$ *Equation 17* (Hall and Dobbie, 2022)

The equations above imply that the spatial frequency of the sample illumination can be used to convolve the frequency information in the sample into the bandwidth of the microscope Figure 34.

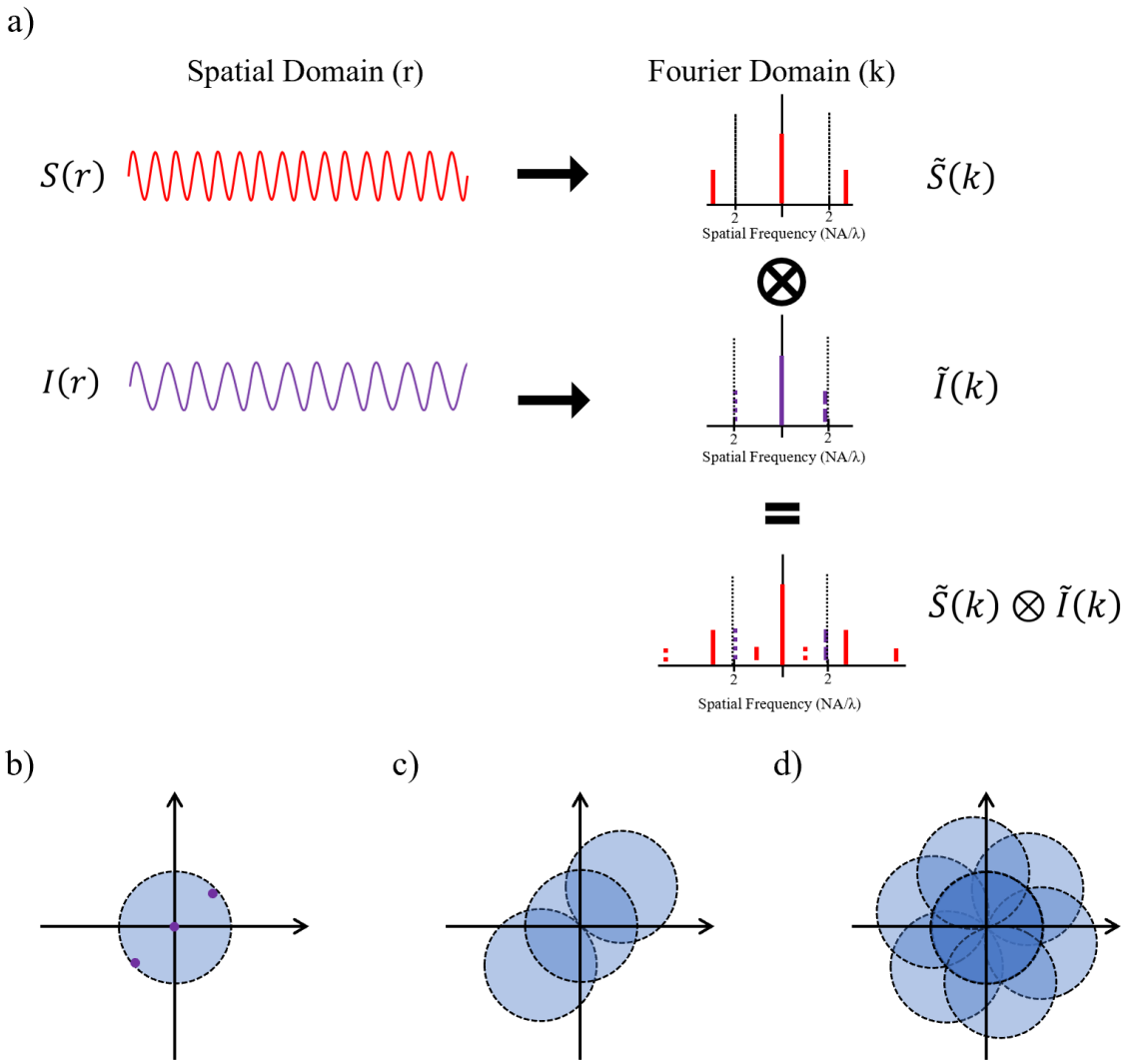


Figure 34 – a) Convolution in the Fourier domain of signal $\tilde{S}(k)$ and structured illumination $\tilde{I}(k)$, demonstrating how the signal is modulated into the microscope bandwidth indicated by the dotted black lines. b) Bandwidth of the microscope in two dimensions indicated by the blue circle, and 2D Fourier transform of the illumination pattern shown by 3 purple dots. c) Through the use of structured illumination, phase shifting the pattern at least 3 times, and reassigning the information captured, twice the bandwidth can be captured in one dimension. d) By rotating the structured illumination pattern by 120° and 240°, the resolution enhancement can be achieved in all directions.

For instance, if the sample has a frequency of 2.5 NA/λ, this will fall outside the bandwidth of the system, as shown in Figure 34a. Through convolution with an illumination pattern with a frequency of 1.9 NA/λ, this means using the convolution equation:

$$\tilde{S}(k) \otimes \tilde{I}(k) = \int_{-\infty}^{\infty} \tilde{I}(r)\tilde{S}(k-r)dr$$

Equation 18 (Hall and Dobbie, 2022)

None zero values of $\tilde{I}(l)$ occur when l = 0, +1.9 and -1.9 and non-zero values of $\tilde{S}(k-l)$ occur when $(k-l)$ = 0, 2.5 and -2.5. This means that non-zero values of $\tilde{S}(k) \otimes \tilde{I}(k)$ occur when k = -4.4, -2.5, -1.9, -0.6, 0, +0.6, +1.9, +2.5, 4.4. Of the sidebands generated at -4.4, -0.6, 0.6 and 4.4, those at -0.6 and +0.6 are within the bandwidth of the system and are captured.

By applying the illumination pattern at, for example, phase shifts of 0°, 90°, 180° and 270°, allows these sidebands to be reassigned to their correct position in k-space, resulting in twice the amount of k-space being captured in one dimension (Figure 34c). By rotating the illumination pattern by 120° and 240°, this resolution improvement can be achieved in all directions.

5.1.3 Solid Immersion Lens Theory Overview

The numerical aperture (NA) of a lens is defined by the equation:

$$NA = n \cdot \sin\alpha$$

Equation 19 (Sanderson, 2019)

Where n is the refractive index of the immersion medium and α is the half angle of light acceptance. As the maximum value for sin(α) = 1 for e.g. α = 90°, the numerical aperture is limited to a maximum of n. In reality, it is impractical to achieve α = 90° so the actual NA will be less than n. If the immersion medium is air, n ≈ 1, then accordingly the highest NA which can be achieved is around 0.95. NA can be improved by increasing the refractive index of the immersion medium by placing a drop of water (n ≈ 1.3) or oil (n ≈ 1.51) which increases the maximum NA to around 1.2 and 1.5 respectively. To move beyond this using liquid immersion media, special coverslips and oils are required which are more difficult to work with but are commercially available to provide an NA of up to 1.7 (APON100XHOTIRF, Olympus). To increase the NA further, a Solid Immersion Lens (SIL) can be used.

SIL replaces the immersion medium such as oil or water and the coverslip with a lens on which the sample is mounted, meaning the sample is mounted directly on the lens which is then used in combination with a conventional objective. There are two main types of SIL, Hemispherical SIL (HSIL, Figure 35a) and Aplanatic SIL (ASIL, Figure 35b) (Terris *et al.*, 1994).

The NA of a combined HSIL and objective is:

$$NA = n \cdot NA_0$$

Equation 20 (Terris et al., 1994)

Where n is the refractive index of the SIL and NA_0 is the numerical aperture of the conventional objective the SIL is paired with. For an ASIL, the NA is defined as:

$$NA = n^2 \cdot NA_0$$

Equation 21 (Terris et al., 1994)

For both HSIL and ASIL, as is the case for all other lenses, the NA is still limited to the refractive index of the SIL, and for HSIL, this means that the maximised NA is not practically achievable due to the maximum NA of the conventional objective being around 0.95. For an ASIL however, the square term in Equation 16 means that it is practical to attain the maximum theoretical NA of n. This is illustrated in Figure 35, where the light acceptance half angle of the conventional objective α_0 is smaller than the acceptance half angle for the system α. This is considered in more detail in 5.2.3.

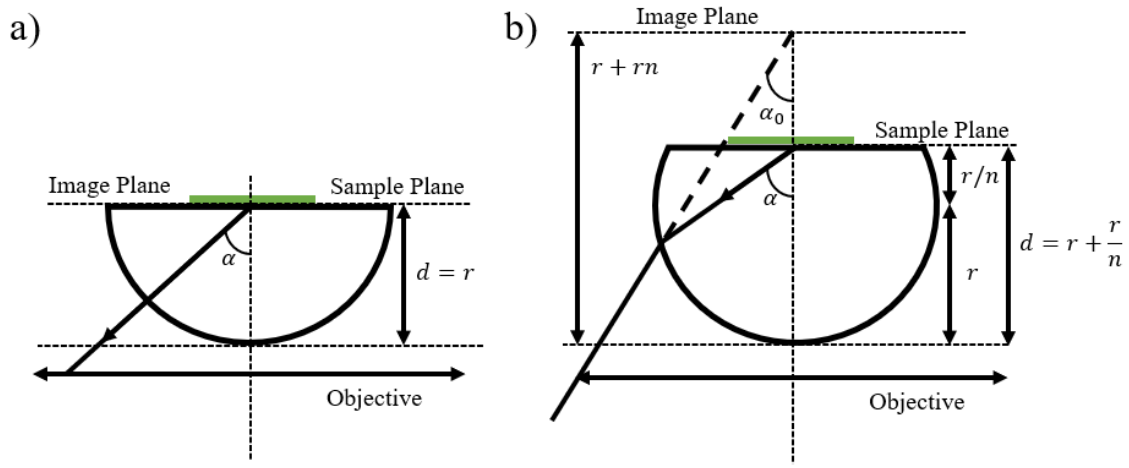


Figure 35 - a) Hemispherical SIL where d, diameter along optical axis, is the equal to the radius r and b) Aplanatic SIL where d is a function of r and SIL refractive index, n.

To make the most of these NA enhancing capabilities, SILs are generally created using high numerical aperture materials such as high refractive index glasses like S-LAH79 (Zhang *et al.*, 2006; Wang, 2010; Darafsheh *et al.*, 2014) or other high refractive index materials such as Zirconia (Wang *et al.*, 2012, 2019).

Since the resolution increase that can be achieved using SILs is mainly realised through the high refractive index material the SIL consists of, it is important to note that the resolution enhancement is only present near to the SIL's surface. As a sample moves away from the surface, the refractive index of the material the sample is immersed in becomes the limiting factor. For a 1 mm zirconia ASIL, increasing the imaging depth from 10 nm to 50 nm resulted in a 24% degradation of resolution (Wang *et al.*, 2019).

Both HSIL and ASIL image the sample at points free of spherical aberration on the optical axis, however, the ASIL images the sample at the aplanatic point, meaning that off-axis imaging is also free of spherical aberration (Wang, 2010). The positions of this aplanatic conjugate pair are shown in Figure 35b relative to the point at which the curved surface of the lens meets the optical axis, which is also a point free of spherical aberration.

5.1.4 Total Internal Reflection Fluorescence with SIM/SIL

For a bacterial sample on a zirconium ASIL with a refractive index of 2.17 and using Equation 7 the critical angle is only 40°. This means that for any reasonable implementation of SIM/SIL, the sample will be illuminated with an evanescent field as the two beams which interfere to create the structured illumination will be inclined at an angle greater than this.

Further, using Equation 9, with an illumination wavelength of 636 nm and an illumination angle of 66°, the penetration depth can be calculated to be 35 nm and provides the theoretical illumination profile shown in Figure 36. Because the SIL resolution degrades with imaging depth, using TIRF illumination is ideal as it eliminates illumination of the sample at depths where the resolution will be degraded.

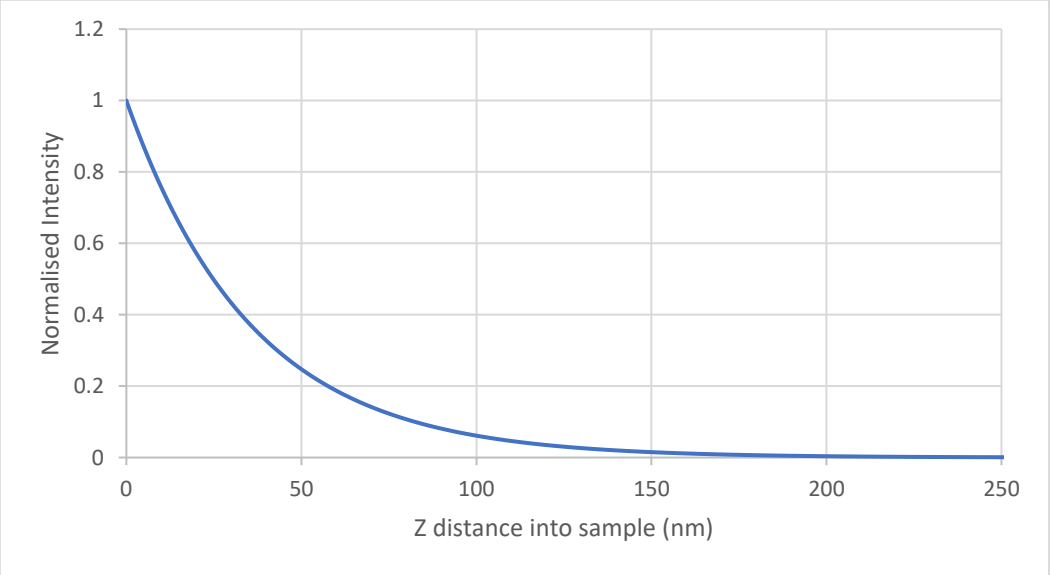


Figure 36 – Illumination profile in Z of a bacterial sample on a zirconium ASIL, with an illumination wavelength of 636 nm and illumination angle of 66°, simulated using Equation 9.

5.2 Apparatus

The spatial light modulator and SIL objective described below apply to both the incoherent and coherent designs.

5.2.1 Spatial Light Modulator Selection

The spatial light modulator is what creates the structured illumination in a SIM system and is therefore a critical part of the microscope design. Most SIM systems use a diffraction grating at a conjugate sample plane to achieve the characteristic striped structured illumination pattern. (Heintzmann and Cremer, 1999; M. G. L. Gustafsson, 2000). This grating must then be transposed to create the necessary phase shift and rotated to achieve near isotropic resolution doubling. These mechanical transformations of the grating add time between each frame meaning that the time to create each SIM frame is increased and with that the time to acquire a measurement. For fixed samples, this is not a problem, but for live cells, where dynamic behaviour is observed, movement between frames in a single SIM frame creates imaging artifacts. To increase the speed of transformation and thus minimise these artifacts, different forms of spatial light modulators, such as Liquid Crystal on Silicon (LCoS) (Fiolka, Beck and Stemmer, 2008), Digital Micromirror Device (DMD) (Chakrova *et al.*, 2015) and acousto-optic deflectors (Gliko, Brownell and Saggau, 2009) have been utilised. Of these three options, LCoS is the most commonly used in practise. However, because a DMD is the only spatial light modulator which has been shown to work with an LED light source (Dan *et al.*, 2013), I opted for this option in the present work (Table 13). A DMD also comes with the advantage of being considerably cheaper due to its adoption in digital projectors, but does come with the drawback of acting as a blazed diffraction grating, meaning that the angle of illumination requires careful optimisation if used with a coherent light source. However, for an LED light source this is not a concern.

For the DMD I chose to use the DLP6500 (Texas Instruments) for its excellent evaluation board, high fill factor of 92% and high reflectivity across the visible spectrum. The evaluation board allows a series of images (structured illumination patterns) to be uploaded to the board's internal memory, which can then be changed through an internal and external trigger line, allowing the system to be triggered with the camera.

Property	Value
Array width	1920 mirrors 14.5 mm
Array height	1080 mirrors 8.16 mm
Mirror pitch	7.56 x 7.56 µm
Mirror tilt angle	± 12°
Pattern rate	11.574 kHz
Diffraction Efficiency	86%

Table 13 – DMD properties

5.2.2 SIL Selection

A SIL has 3 properties which can be adjusted to suit the specific application: Shape, size and material. For this microscope, I chose to use the 1mm zirconia ASIL (Knight Optical). Below I will explain the reasoning behind the choice of SIL for this project.

As introduced earlier in this thesis, there are two shapes of refractive SIL commonly deployed, the hemispheric SIL (HSIL) and the aplanatic (ASIL) (Terris *et al.*, 1994). The ASIL has the advantage of having a larger aberration free imaging area and can potentially offer a higher NA, depending on the NA of the conventional objective chosen. For this reason, the ASIL was the preferred choice.

When choosing the size of the SIL, the ease of handling and larger field of view found in larger SILs must be balanced against the levels of chromatic aberration of smaller SILs. Using structured illumination means that chromatic aberration will affect the effective NA of both the excitation and emission, meaning that minimising aberration is particularly critical.

Finally, when considering the material, the principal factors which must be considered are refractive index, which determines the NA, and dispersion, which causes chromatic aberration.

Additionally, factors such as cost and manufacturability must be considered. As SIL development and manufacturing is a timely process, a commercially available SIL is highly preferable.

Based on the criteria above, a 1mm zirconia ASIL (Knight Optical) was chosen. Its refractive index is 2.17, meaning that it is possible to create a system with an NA significantly higher than that of the best performing oil immersion objectives. Unlike diamond, which has an even higher refractive index, it is cheap and relatively easy to machine. The major drawback of cubic zirconia is the high dispersion, which I mitigated through the use of a relatively small ASIL. Finally, within our research group there is expertise in using this type of ASIL, which added to the feasibility of the project (Wang *et al.*, 2019).

For this SIL, the maximum usable field of view (FoV) is 60 x 60 μm (Wang *et al.*, 2019). However, to ensure that field curvature would not be an issue, a FoV significantly lower than this will be targeted.

5.2.3 Pairing conventional objective with solid immersion lens

To utilise the full potential of the ASIL, meaning that the full (theoretical) 90° of the collection cone can be utilised, it is critical that an appropriate conventional objective is chosen to partner it. The conventional objective must have a high enough NA to satisfy the condition:

$$NA_{conv} \geq \frac{1}{n_{SIL}}$$

Equation 22
(Wang, 2010)

Where NA_{conv} is the NA of the conventional objective, and n_{SIL} is the refractive index of the SIL at the emission wavelength. A second constraint is that the working distance of the objective must be sufficiently large to achieve focus under the SIL. To do this it must satisfy the condition:

$$W.D._{conv} \gg r \cdot (n+1)$$

Equation 23
(Wang, 2010)

Where r and n are the radius and refractive index of the SIL respectively.

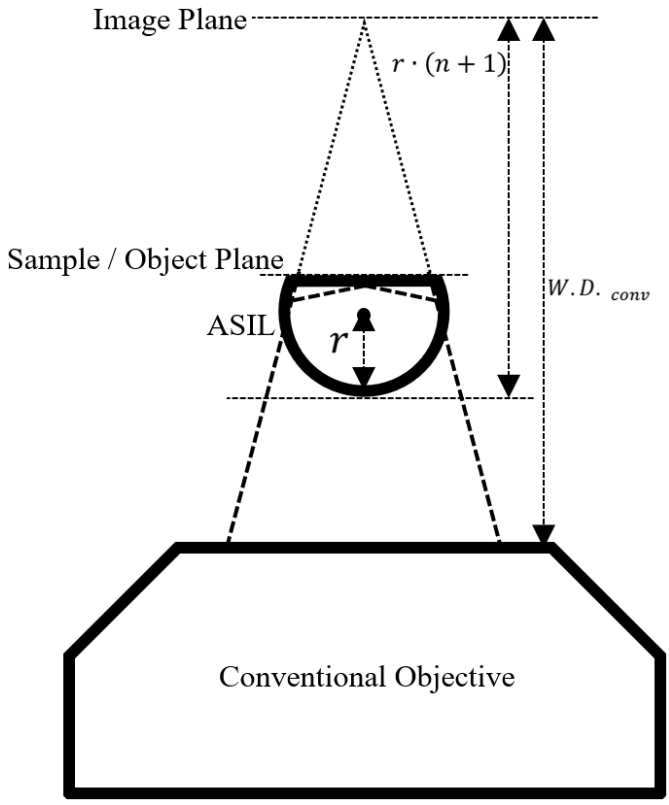


Figure 37 - Diagram showing the optical configuration of the ASIL with radius r, and the conventional objective with working distance W.D. $_{conv}$. Samples are placed on the truncated surface of the ASIL at the Object Plane which creates a virtual image at the Image Plane, at a distance of r(n+1) from the curved surface of the ASIL, where n is the refractive index of the ASIL.

For this choice of ASIL, this means that the conventional objective must have an NA of at least:

$$\frac{1}{2.17} = 0.46$$

And a working distance significantly greater than:

$$0.5 \cdot (2.17 + 1) = 1.585mm$$

At time of the microscope development, there were several objectives which fulfilled these criteria from major brands. I opted for the LD C Epiplan-Apochromat 50x/0.6 DIC (#422672-9800-000, Zeiss) with a working distance of 7.6 mm to complement the chassis used in the initial development (see 5.3.2). The magnification of this system is defined by:

$$m = m_0 n^2$$

Equation 24
(Wang, 2010)

Where m_0 is the magnification of the conventional objective (50x), and n is the refractive index of the ASIL (2.17). This means that this pairing, when combined with a 164.5 mm tube lens, will result in a magnification of 235.45x.

Similarly, the focal length of the ASIL objective is calculated using the equation:

$$f = \frac{f_0}{n^2}$$

Equation 25
(Wang, 2010)

Where f_0 is the focal length of the conventional objective and n is the refractive index of the ASIL. Combining a 3.28 mm focal length conventional objective with this ASIL results in a combined focal length of 0.7 mm.

The properties of the SIL objective are summarised in Table 14.

Property	**Value**
Theoretical Numerical Aperture	2.17
Magnification (with 164.5mm tube lens)	235.45x
Focal length	0.70 mm
Diffraction limit (Abbe limit @ λ = 636 nm)	146.5 nm

Table 14 – Properties of combined SIL objective

5.3 INCOHERENT SIM DEVELOPMENT

5.3.1 Incoherent SIM

Most structured illumination systems use coherent light from a laser source to create a striped interference pattern using diffraction (Wu and Shroff, 2018). Previous work suggests that this can also be achieved using an incoherent source such as an LED (Dan *et al.*, 2013). The advantages of such a system are the cost of components and lower administrative burden due to not featuring

a laser. The latter was a major practical consideration at the onset of this project, due to the lab space that was available to me at the time. For this reason, a large part of my DPhil project was devoted to developing an incoherent SIM system. Unfortunately, as time went on, a number of issues with this approach became apparent, and these are detailed below.

5.3.2 Optical Design

The initial optical design for the system was based on the design in Dan *et al* but adapted to utilise a commercially available microscope chassis (Axio Observer Z1, Zeiss). This was to provide a stable alignment for the high magnification optics and to provide precise stage movements in X and Y for aligning the objective to the SIL and movement in Z for focus.

The microscope design is detailed in Figure 38. To illuminate the DMD in a uniform manner marginally underfilling the DMD, a hexagonal optical integrator (OI in Figure 38) was used. Using L1 (16 mm Aspheric Condenser, Thorlabs) and L2, (40 mm Achromatic Doublet, Thorlabs), an image of the LED source (SOLIS-470C, Thorlabs) was projected onto the front surface of the OI. Through the process of total internal reflection, this uniformly illuminates the back surface of the integrator which was imaged onto the digital micro-mirror device (DMD, Figure 38) through L3 (75mm Achromatic Doublet, Thorlabs), L4 (100mm Achromatic Doublet, Thorlabs), and the TIR Prism.

The DMD must be illuminated at 24° to produce a projected beam which is orthogonal to the DMD itself, due to the fact that the mirrors of the device in the off position are angled at 12° relative to the desired output beam angle. This means that it is difficult to space the illumination and projection optical paths in a way which is space efficient. To get round this issue, a TIR prism was deployed (Dan *et al.*, 2013). The illumination beam intersects with the interface between the glass and air gap between the two prisms at beyond the critical angle, meaning it is reflected towards to DMD. The projected beam from the DMD then intercepts the glass air interface at a non-critical angle, meaning that the beam is transmitted through into the second prism.

Due to the incoherent nature of the illumination, the diffracted light from the DMD is more spread that it would be for a coherent system. This means that it was not possible to spatially filter the central diffraction order at the Fourier plane, as is the case in Dan *et al.*, 2013 and the higher orders are blocked by the back focal plane of the objective. The system is very much like a projector, where the pattern on the DMD is demagnified onto the sample rather than magnified onto a screen.

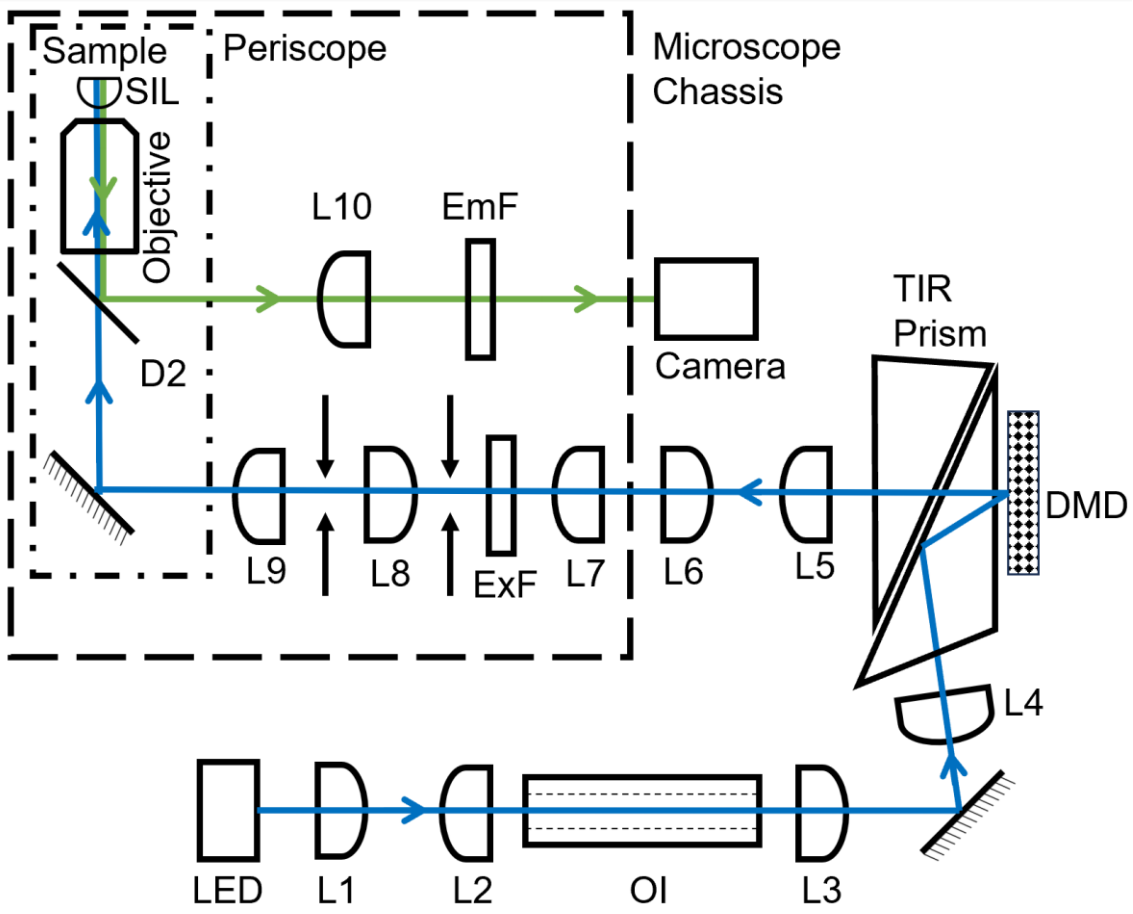


Figure 38 - Optical layout of incoherent structured illumination microscopy design

Two more lenses, L5 (50 mm Achromatic Doublet, Thorlabs) and L6 (30 mm Achromatic Doublet, Thorlabs) were used to adjust the magnification prior to entering the microscope chassis. The epi-illumination beam path was used for illumination and featured a slider for excitation

filters (Chroma HQ500/20), a conjugate sample plane, and conjugate back aperture plane, both of which had slots for irises.

L7-9 were fixed into the system and for that reason could not be identified. Therefore, bulk optical properties of these lenses had to be obtained experimentally.

Rather than immediately trying to integrate the SIL, I used a Zeiss 100x objective (Zeiss) for testing.

Finally, a detector was chosen to fulfil the Nyquist requirements for this optical system with both objective types. For the SIL objective, the maximum spatial resolution achievable is 120 nm assuming a fluorescence at 521 nm, and with a 235.45x magnification. This means the smallest resolvable feature at the detector is 28.3 μm and sets the maximum pixel size meeting the Nyquist criteria at 14.2 μm.

Performing the same calculation for the standard 100x, 1.4 NA objective, the smallest resolvable feature at the detector is 18.6 μm and meaning the maximum pixel size which meets the Nyquist criteria is 9.4 μm.

5.3.3 Decision to move to a coherent design

During use, the contrast achieved with the incoherent optical design always degraded as the projected frequency approached those suitable for SIM. Initially, I made several improvements to the design, most notably using the TIR prism, which allowed the 200 mm focal length L4 to be replaced with a 100 mm focal length lens, doubling the numerical aperture of the DMD illumination path. This is because the NA in air is approximately equal to the entrance pupil diameter (which was not changed) divided by the focal length which was halved. The illumination source was also upgraded from 440 mW to 3 W to improve the signal strength.

Despite these changes and other minor modifications, it became apparent that the contrast degradation effect was always present at higher frequencies, and that this is predicted by the Modulation Transfer Function for incoherent light, where the modulation strength (or contrast) is

drastically reduced at the frequencies required for SIM (Figure 39). This means that SIM, when using an incoherent source such as an LED, will always be subject to low pattern contrast and therefore is prone to poor quality reconstructions (Lal, Shan and Xi, 2016; Li *et al.*, 2020).

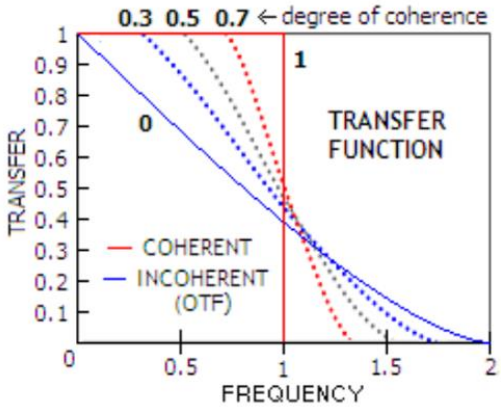


Figure 39 - Optical transfer function at different degrees of coherence. Image Credit: (TelescopeOptics.net, 2006)

In addition to this technical issue, the COVID-19 pandemic also had severe impact on the development of this system, as access to the equipment at the Harwell research campus was limited to a maximum of one day a week for over a year which made continuing work on this system nearly impossible. As new lab space was found in Oxford, the decision was taken to move to a laser light source so a more conventional SIM design could be set-up. The administrative requirements of using lasers in the new lab were not prohibitive of this approach. In the next section, I will detail the development of this coherent SIM system.

5.4 Coherent SIM Development

The optical design used for this system is based on a design by Sandmeyer and colleagues which utilises the same DMD as the one available for this DPhil (Sandmeyer *et al.*, 2019). Therefore, the majority of the same optical and electronic design could be utilised as described in Sandmeyer et al., (2019).

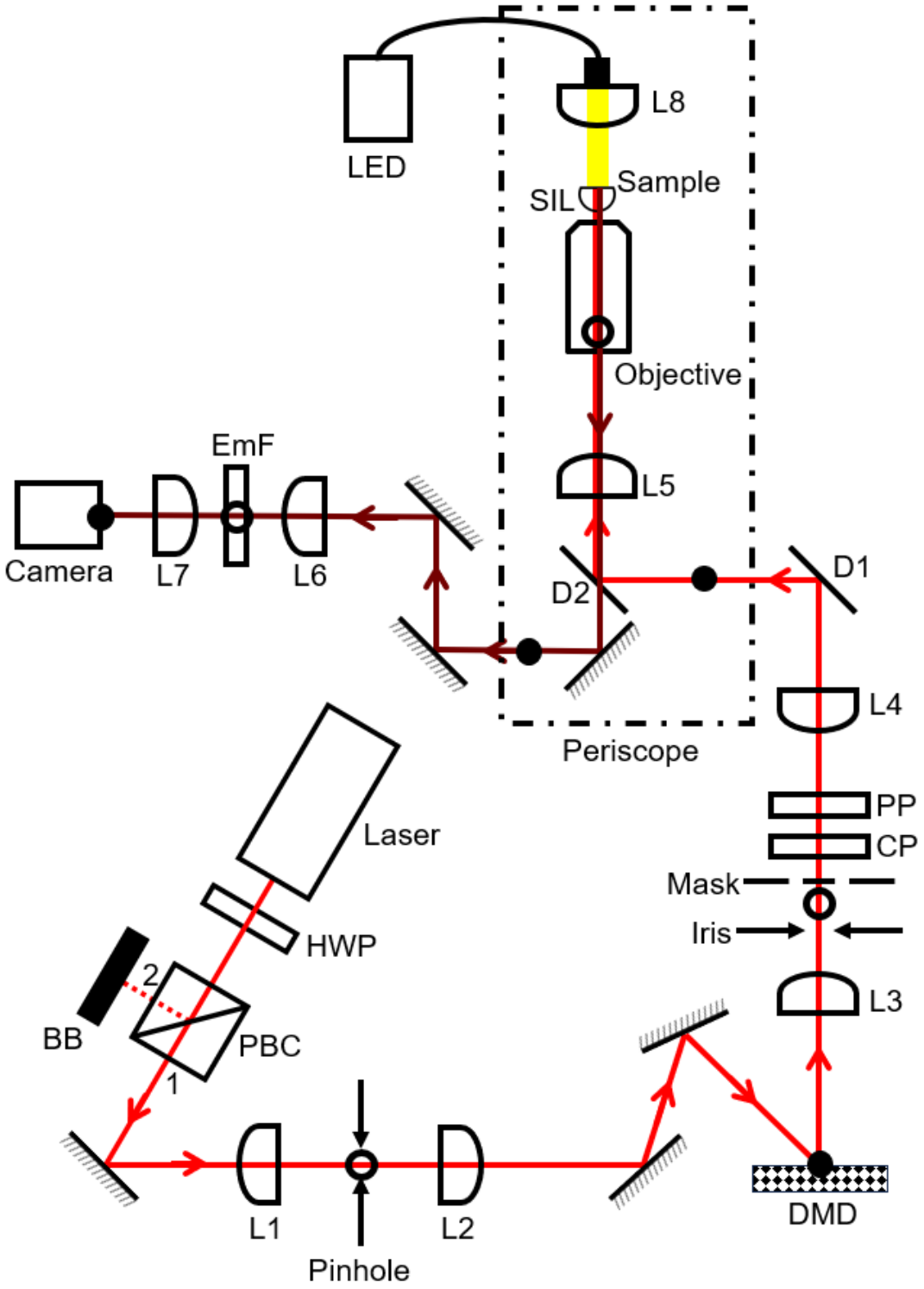


Figure 40 – Diagram of the coherent structured illumination microscopy optical layout. Key conjugate sample planes and conjugate back focal planes have been identified with spots and circles, respectively.

The beam from the laser light source (5.4.2) was then expanded through a Keplerian beam expander formed of L1 and L2 (5.4.9), before being steered into the DMD (5.4.3) (Figure 41a). The DMD was rotated by 45° (Figure 41b), so the title angle of the mirrors was orthogonal to the table. The light from the DMD was collected in L3 (5.4.4) and passed through an iris and mask (5.4.5) to remove all but the 1st order side bands (Figure 41c), ensuring that a sine wave pattern was created at the sample through 2 beam interference. Immediately following the mask was a circular polariser (CP) and pizza polariser (PP), an optical component made up of 6 segments of linear polariser material (see 5.4.6), were positioned. Together, these served to S-polarise the side orders of each structured illumination angle (Sandmeyer *et al.*, 2019), preventing depolarisation through the objective. L5 then focussed to a conjugate sample plane between two identical dichroic mirrors D1 and D2 (5.4.7), which steered the beam parallel to the table and then orthogonally into the periscope section (Figure 41d). The periscope section contained the tube lens and SIL objective (5.2.3). The SIL itself (or coverslip during testing) was placed on a motorised X, Y, Z stage with piezo Z control for precise focussing (5.4.1).

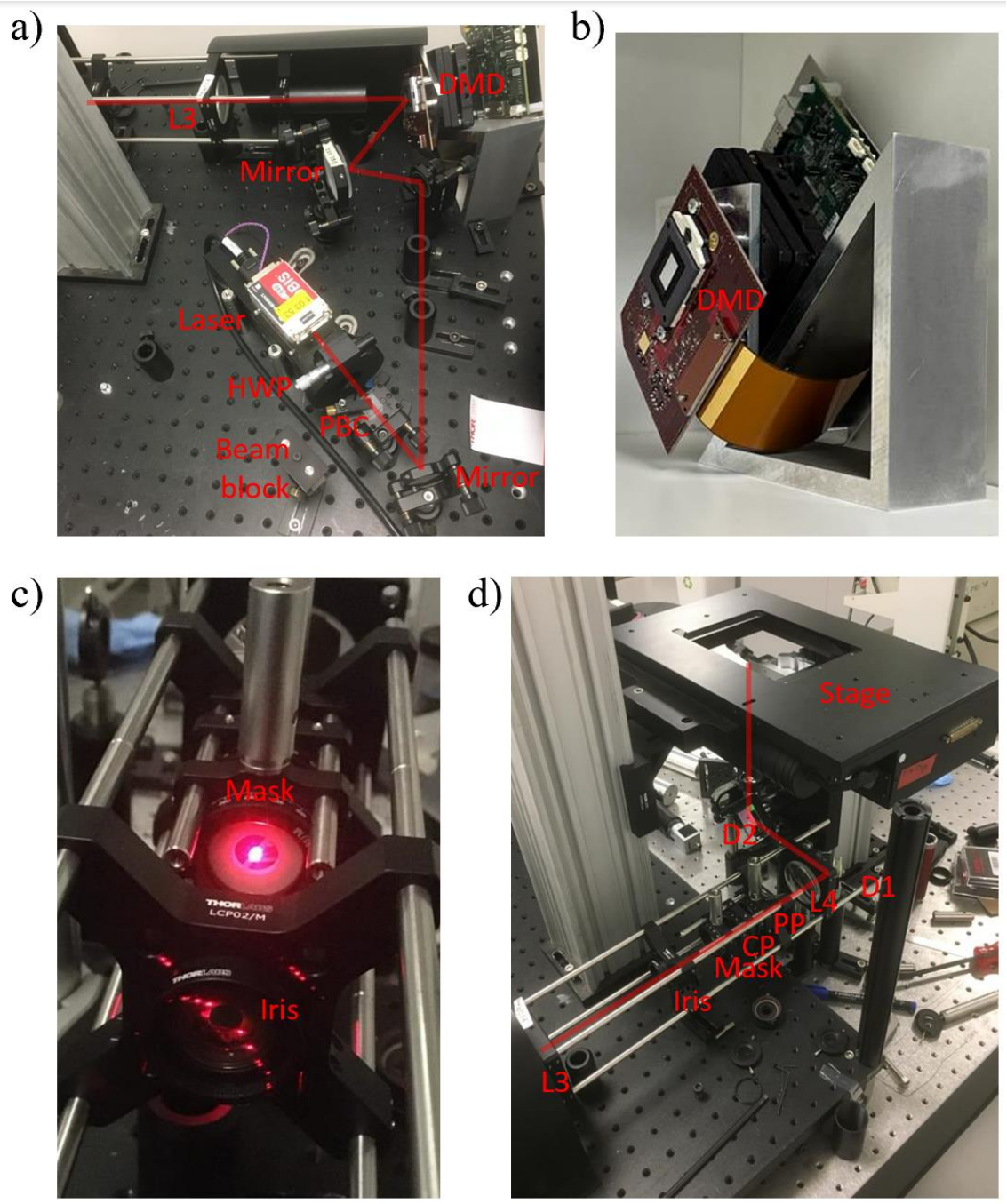


Figure 41 – Images of the coherent SIM illumination path. a) Illumination path from laser to L3 with beam path superimposed (L1 and L2 not shown) b) Custom bracket to support DMD at 45° with tip/tilt stage.. c) diffraction pattern from DMD, with high orders blocked by the iris and fundamental blocked by the mask. d) Illumination path from PP to objective with the beam path superimposed.

Fluorescence from the sample located on the SIL was transmitted back through the SIL objective, tube lens and D2 before being steered out of the periscope and into the detection path through three mirrors. The detection path consisted of means for further magnification through L6 and L7, and an emission filter at the conjugate back focal plane to remove any of the excitation wavelength and reduce chromatic aberration from the SIL. Finally, the detector was positioned at the conjugate image plane following L7 (5.4.8).

A transillumination system was added consisting of a fibre coupled LED and a collimating lens L8 to aid the positioning and focussing of the SIL lens.

Details on each of these optical sub-systems follow below.

5.4.1 Optomechanics

As a lab move was required during the development of the system, the illumination system between the light source and the D1 was built as a module on an optical breadboard, allowing it to be moved as a single unit.

All mirrors were placed in kinematic mounts to facilitate alignment of the system. L3 to L4 were integrated into a cage system to ensure that those components remained concentric. The periscope section was mounted to an optical rail for stiffness with carriages to allow movement along the optical axis for focussing, as shown in Figure 42. The custom objective mount was attached to the carriage through a z-stage for course focus.

To align the sample or ASIL together with the sample with the conventional objective, a motorised XY stage was used (H117, Prior Scientific) with a piezo z-stage (QGSP400-D1, Prior Scientific).

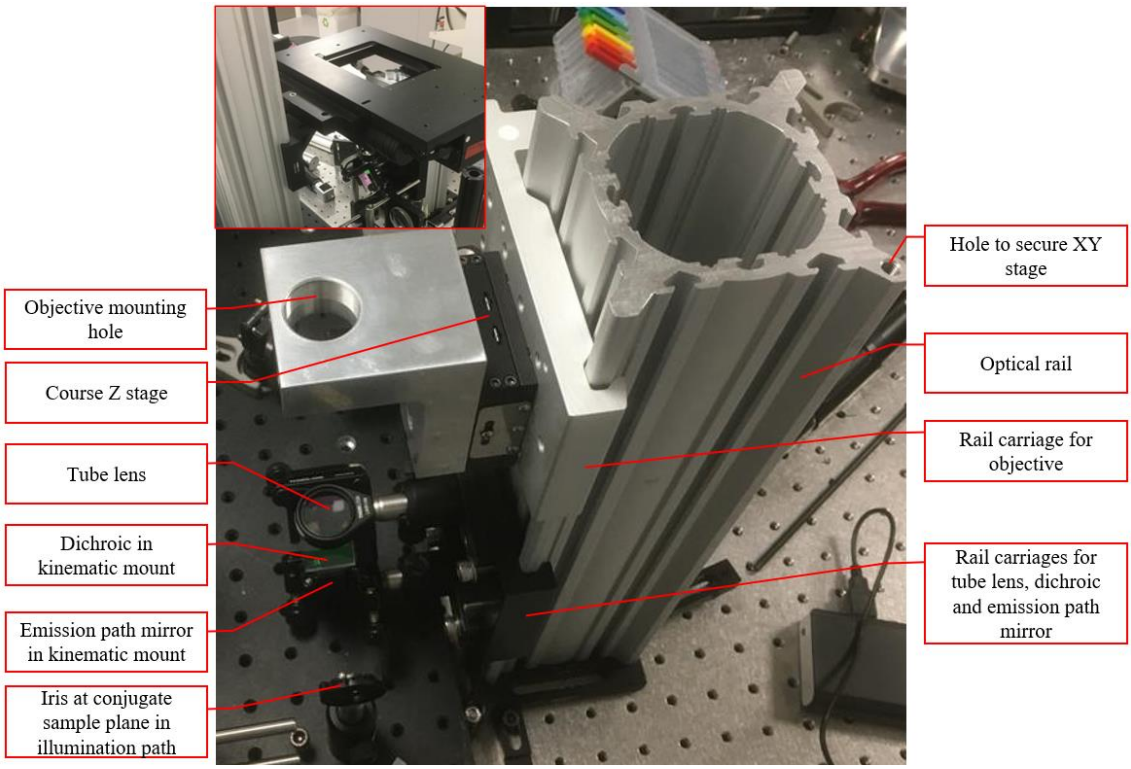


Figure 42 - Periscope section of the system without stage. Stage mounting shown in inset.

5.4.2 Light Source

The OBIS LX 640 nm 100 mW Laser (Coherent) was chosen as the light source (Table 15). The wavelength was chosen to match that of the light source used in Chapter 3 so that the same labelling regime and dyes could be used. The power of the laser used was 100mW, as used previously by Sandmeyer *et al.* Finally, this laser driver also came with an external interlock connection which meant that it could be integrated and approved by the laser safety officer quickly.

Property	**Value**
Actual wavelength	636 nm
Power	100 mW
Beam diameter at the 1/e2 point	0.8 mm

Table 15 – Laser properties

Immediately following the laser, a rotating half wave plate (HWP) (AHWP05M-600 mounted in PRM1, Thorlabs) and beam polarising beam splitter cube (PBC) (PBS251, Thorlabs) were positioned. This allowed for easy attenuation of the laser beam by rotating the HWP, changing the direction of polarisation which varied the proportion of the laser power at each output of the PBC. Changing the power output of the laser using the laser controller can affect some of the beam properties such as coherence length. The power was measured at output 1 of the PBC to verify the performance of the attenuator, results of these measurements are included in Table 16.

Laser Controller Power	Max Power		Min Power	
mW	mW	%	µW	%
1.00	0.85	85.00	0.54	0.05
50.00	46.10	92.20	19.40	0.04

Table 16 – Laser power measured at output 1 of the PBC at different laser intensities and attenuation.

5.4.3 DMD and Blaze angle

Using the DMD as described in 5.2.1, the smallest period which can be created is 30.24 µm due to the fact that at least 4 mirrors are required to create a period which can be phase shifted at least 3 times (in this case 4, 1 micromirror (90°) phase steps). The reason 3 micromirrors cannot be used is due to the binary nature of the mirrors. To achieve a digital representation of the sine wave, a duty cycle (on/off ratio) of 50% must be maintained, which cannot be achieved with only 3 mirrors. A 6 micromirror period (45.36 µm/cycle) is the smallest period which can be used with 3 (2 micromirror, 120°) phase steps. To provide flexibility, an initial period of 12 micromirrors (90.72 µm/cycle) was chosen. This allowed the use of either 90° or 120° phase steps as well as providing the ability to make the pattern period smaller or larger had it become necessary. A 4, 90° phase step was chosen initially as it is considered superior for cancelling phase shift errors (Wang, 2010).

As the DMD structure acts as a blazed diffraction grating, it is important to set the illumination angle correctly. This ensures that the desired diffraction orders have the highest and an even

intensity. The illumination angle varies with both illumination wavelength and DMD specification, so it must be optimised for each pairing. To find the optimum angle, an adapted version of an experiment in Sandmeyer *et al.* was carried out (Figure 43).

First, the 0° line was set by aligning the beam through an iris positioned on the grid system on the table. This beam was then reflected off the protective window on the DMD back through the iris and into the centre of the laser as shown in Figure 43a. The tip/tilt stage on which the DMD was mounted was used to perform this alignment.

A goniometer was then used to rotate the laser around the central axis of the DMD so it could be illuminated at different values of α as shown in Figure 43b. For α intervals of 1° between 14° and 55° the intensity of the 0^{th} (M) and 1^{st} (A-D) diffraction orders was measured using a laser power meter (Fieldmaster, Coherent).

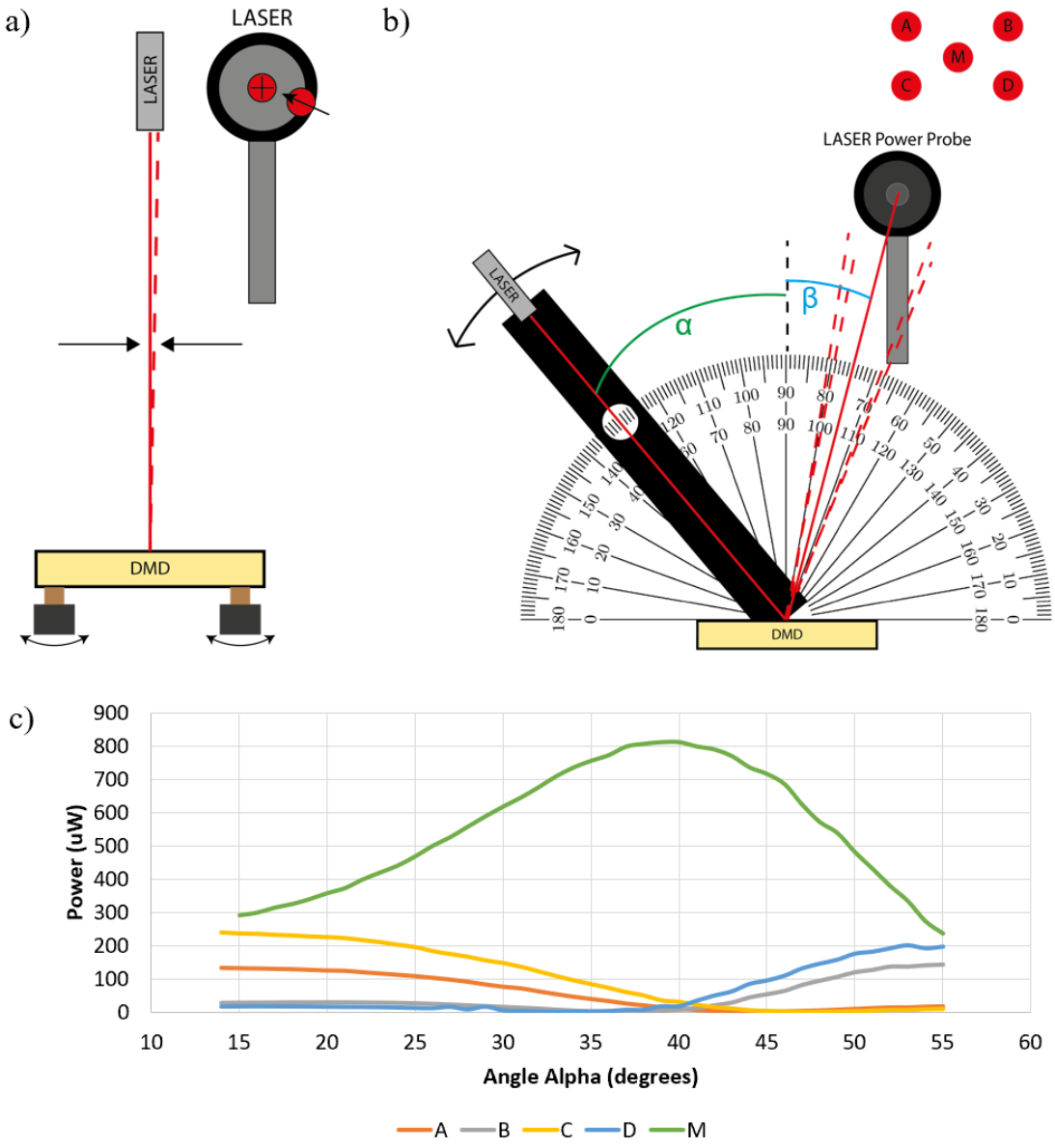


Figure 43 – Experiment to optimise the illumination angle of the DMD. a) Aligning the DMD with the 0° line. b) Experimental set-up showing the goniometer which revolved the laser around the centre of the DMD so the power of diffraction orders could be measured. c) Results of the experiment, showing the intensity of M is maximised at 39°. Protractor image obtained from and https://maths.prideaux.id.au/ on 29-12-2023.

The optimal illumination condition for the DMD is achieved when the 0^{th} diffraction order is maximised, and side bands are minimised. The reason for this is that this diffraction pattern is formed by the underlying structure of the DMD. By applying the striped pattern to the DMD, side bands are modulated onto each of the diffraction orders resulting from the underlying structure.

The two diffraction orders I want to utilise will be modulated onto the 0^{th} order from the fundamental structure, hence this is the one to maximise. The results depicted in Figure 43c show that the 0^{th} order, M, was maximised at 39°, and so this was used as the illumination angle (Table 17).

Property	Value
Illumination angle	39°
Period	12 micromirrors 90.72 μm/cycle
Phase Stepping	3 micromirrors 90°

Table 17 – DMD Illumination

5.4.4 Structured Illumination magnification

The structured illumination was created by interfering the two 1^{st} order components from the pattern applied to the DMD with the 0^{th} order component blocked. This means that with a 1x magnification, the period would be half that of the period applied to the DMD.

To ensure the sinusoidal pattern produced at the sample is close to the theoretical Abbe resolution limit of the SIL objective, an appropriate demagnification had to be applied. A 100 mm tube lens (AC254-100-A-ML, Thorlabs) was selected and after being paired with the SIL objective, gave a magnification of 0.00714x (demagnification of 140x). This means that the chosen DMD pattern would have produced a pattern of 324 nm/cycle at the sample, meaning another 0.5x magnification would reduce the period at the sample to 162nm/cycle, close to the Abbe resolution limit of 147 nm. As another conjugate back focal plane is required for the filtering and polarisation of the diffraction orders, both of these requirements could be fulfilled by using a 200 mm lens (ACT508-200-A, Thorlabs) for L3 and a 100mm lens (AC508-100-A, Thorlabs) for L4, in a 4f configuration. The 200 mm focal length was chosen for L3, as it was the shortest focal length

which could be used without impeding the 39° illumination angle for the DMD while providing enough separation to spatially filter the diffraction orders.

As the DMD size is 8.16 mm, this means that the maximum short axis of the FoV which can be illuminated on the sample is 29.1 μm.

As the system was tested with and without the SIL, the values for the structured illumination system with and without the SIL are summarised in Table 18.

Property	**Value with SIL Objective**	**Value with conventional objective only**
Magnification of Objective and Tube Lens	0.00714x (Demagnification of 140x)	0.0328x (Demagnification of 30.4x)
Magnification of L3 and L4	0.5x (Demagnification of 2x)	0.5x (Demagnification of 2x)
Structured Illumination Magnification	0.00357 (Demagnification of 280x)	0.0164 (Demagnification of 61x)
Theoretical pattern period at sample	162 nm/cycle 111% of Abbe Limit	744 nm/cycle 140% of Abbe Limit
Maximum Illumination Area at sample	29.1 μm x 29.1 μm	133.8 μm x 133.8 μm

Table 18 – Structured illumination system properties

5.4.5 Spatial filtering

To filter out the diffraction orders which were not required for illumination, two stages of filtering were applied near to the conjugate back focal plane between L3 and L4. Firstly, an iris was used to filter out the higher orders, and this being an iris meant that the filtering could be tuned. Theoretically, this would not be strictly necessary, as any higher orders should be blocked at the

back focal plane of the objective. However, it seemed prudent to block as many of the "stray" beams as possible, and this feature also proved useful for aligning the system.

The second stage was a custom 3D printed mask (shown in Figure 44), which ensured that the pattern was formed using 2 rather than 3 beam interference. The mask had a 1" outer diameter to allow it to be held in a rotating cage mount (CRM1T/M, Thorlabs) and a 2 mm central circle to block the beam. Space around this allowed the 1st order diffraction beams to pass unimpeded at all 3 illumination orientations. The diagonal support was positioned so it did not interfere with either beam in the three orientations. A simpler way of achieving this may have been to use a glass support and stick the block to the centre of it.

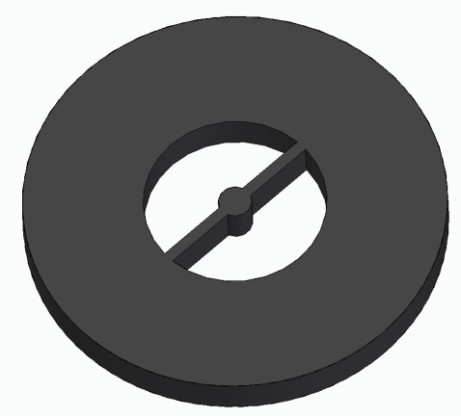


Figure 44 - Mask or Fourier filter to block the 0th diffraction order. (Designed and rendered in Solid Edge, Siemens).

5.4.6 Illumination Polarisation

To achieve the highest structured illumination contrast, it is important that both interfering beams have the same polarisation (Gustafsson, Agard and Sedat, 2000). At the same time, it is also important to ensure that this polarisation is maintained through the high NA objective. To ensure that the latter is the case, beams should have S polarisation (O'Holleran and Shaw, 2012). I followed the approach of Sandmeyer *et al.* who achieved this using a combination of a circular polariser, which consists of a linear polarising film followed by a quarter wave plate, followed by

a pizza polariser. The pizza polariser is made up of 6 segments of linear polariser material, to S-polarise each of the three pairs of beams (Figure 45).

For this design a circular polariser designed for 633 nm was selected (CP1L633, Thorlabs). Two options were available for the pizza polariser, one targeted at the visible spectrum (colorPol® VIS 038 BC3 CW01, CODIXX) and one targeted for the red to infrared part of the spectrum (colorPol® VISIR CW02,CODIXX). Due to the latter having a contrast (parallel vs perpendicular transmittance) of 900,000:1, this option was chosen over the former which had a contrast of 30,000:1.

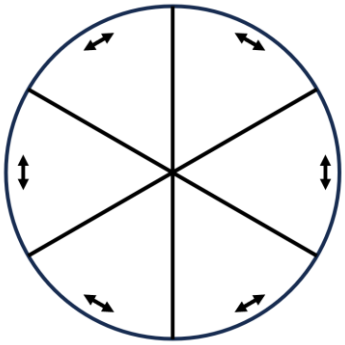


Figure 45 - Diagram of pizza polariser with arrows showing direction of polarisation.

5.4.7 Dichroic Mirrors

Dichroic mirrors are an important part of any fluorescence microscopy set-up, where they are used to separate the excitation light and the emission light, both of which must pass through the objective. Dichroic mirrors exploit the fact that emission wavelength is red shifted from the excitation wavelength by the Stokes shift of the fluorescent molecule being used. This means that when a properly designed dichroic mirror is placed at 45 degrees to the excitation beam, it will reflect it at 90 degrees, towards the objective. Meanwhile, the emission beam from the objective is transmitted through the dichroic mirror and towards the detector. Chroma ZT375/488/532/635rpc (Chroma) was selected as D2 to suit the properties of the wavelength and dye chosen for this work, with high transmission at peak emission and high reflectance at the excitation wavelength. This is shown in Figure 46.

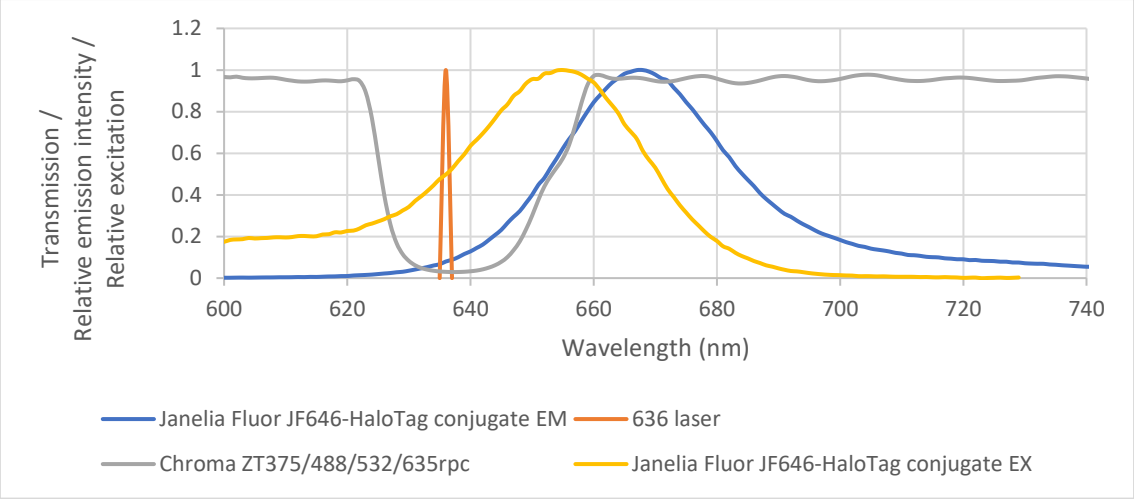


Figure 46- Dichroic spectra shown in grey with spectral position of the laser line marked in orange, and the excitation and emission spectra of JF646 shown in yellow and blue respectively. Plot generated using FPBase (Lambert, 2019).

For high quality structured illumination, it is essential that the polarisation angle set by the pizza polariser is maintained through to the sample. Dichroic mirrors can cause depolarisation when the incoming beam is not linearly polarised either parallel or perpendicular to the tilt axis of the mirror. Due to SIM illumination requiring at least 3 illumination polarisation angles (see 5.4.6), depolarization is certain to occur at the dichroic and the effects of this need to be managed.

One way to counteract depolarisation is to use a second dichroic mirror from the same batch, and place it in the beam path in an orthogonal orientation relative to the initial dichroic mirror (Lu-Walther *et al.*, 2015; Sandmeyer *et al.*, 2019). This means that any depolarisation which occurs at the first dichroic mirror is corrected for at the second. To test the effectiveness of this method, a small experiment was set up using the pizza polariser (PP), a linear polariser (P1) a broad-spectrum LED light source and detector. As illustrated in Figure 47, the camera (ace acA1920-40um, Basler) was set-up with the pizza polariser in front of it and the LED light source was set up with a linear polariser in front of it. These two sub-assemblies were then aligned with one another via varying configurations of dichroic mirrors (Figure 47a-d). In each configuration, the path length was kept the same, and the polarisers were rotated to minimise the pixel values for

dark sections of the pizza polariser. The pixel values for both dark sections of the pizza polariser were recorded and summarised in Figure 47e.

In a perfectly polarised system, no light would be observed in the dark sections of the pizza polariser where the lines are at 90° to the linear polariser. This is what is observed in Figure 47a where there are no dichroics in the set-up, and therefore no depolarisation. When polarised light is reflected off one dichroic mirror from a horizonal or vertical plane into the detector, the pixel values for the dark segments are increased by 36-43x as the light is depolarised by the single dichroic mirror. By compensating for this effect using 2 orthogonal mirrors from the same batch, it is possible to correct for this effect and this greatly reduces the intensity of the dark segments to only 6x the value with no dichroics. Clearly, this solution was not perfect, but given the results from Sandmeyer *et al*, this set-up is likely to be sufficient.

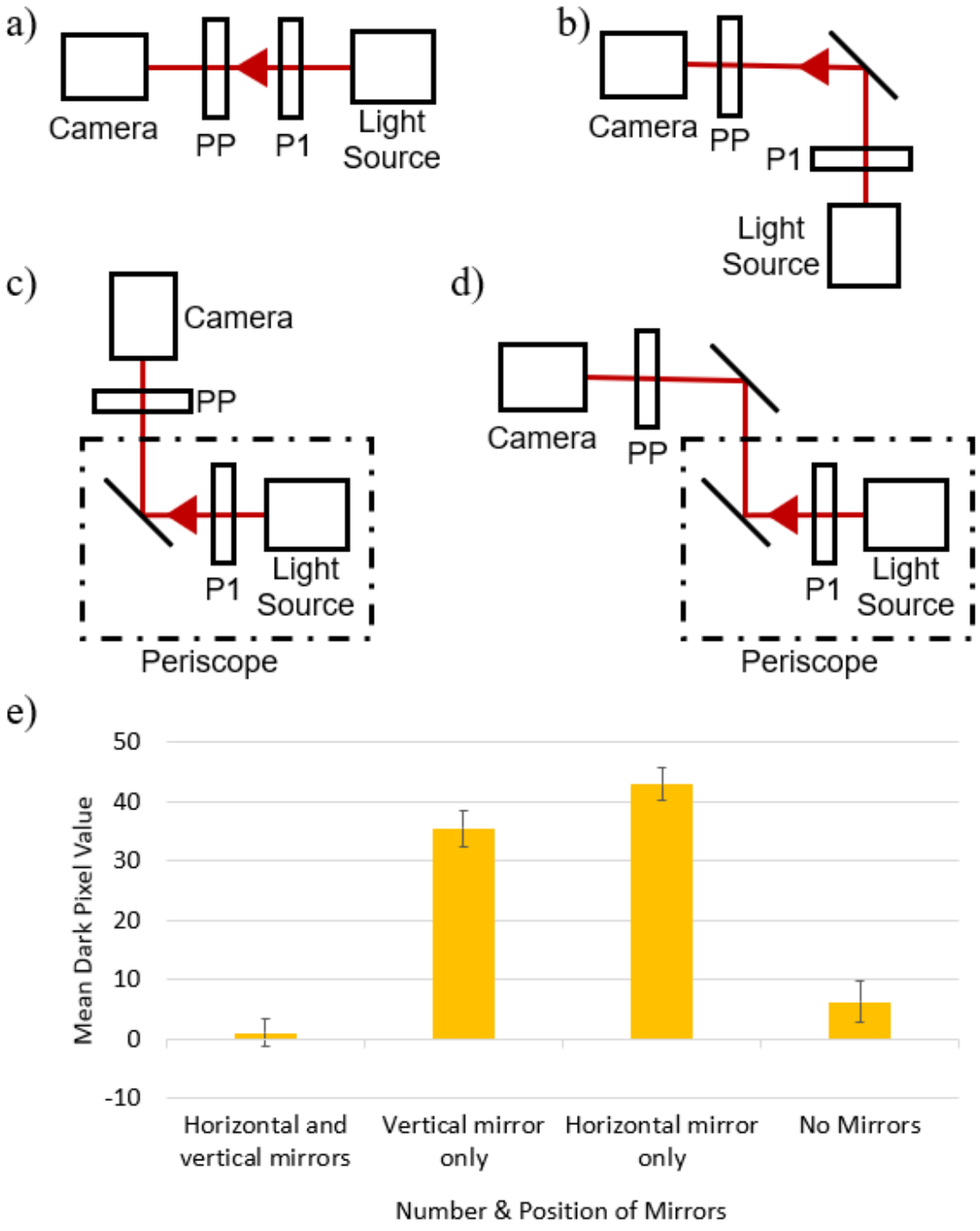


Figure 47 – Demonstration of depolarisation resulting from 0 dichroic mirrors (a), 1 horizontal dichroic mirror (b), one vertical dichroic mirror (c) and 2 dichroic mirrors, one of which is horizontal, and the other is vertical (d). The results (e) show the mean +/- standard deviation pixel value in the dark segment of the pizza polariser. n = 49,964.

5.4.8 Detector and magnification

For wide field microscopy, two detection technologies are typically utilised, namely the Electron Multiplying Charged-Coupled Device (EMCCD) and Complementary Metal-Oxide Semiconductor (CMOS). EMCCD is generally considered more sensitive but has slower frame rates, smaller Fields of View (FoV) and is more expensive when compared to scientific CMOS (sCMOS). Unlike other super resolution techniques, where single fluorophore detection is required, SIM does not require such a high level of sensitivity. This therefore means that an sCMOS or even an industrial grade CMOS could be utilised in the present system, analogous as is described in Sandmeyer *et al.* I opted for the ZWO ASI 294MC-Pro as it had shown good performance in internal lab testing for single molecule applications. The key specifications are shown in Table 19.

Property	**Value**
Resolution	4144x2822
Pixel size	4.63 μm
Quantum Efficiency	>75%

Table 19 – ZWO ASI 294MC-Pro Key Camera Specifications

The Nyquist criterion states that the sampling frequency must be at least twice the highest spatial frequency. For this system, the highest spatial frequency is 147 nm and so this makes the Nyquist criterion for a sampling frequency of 73.5 nm at the sample. As the pixel size of this camera is 4,630 nm, this means that at least 63x magnification is required between the sample and detector to satisfy the Nyquist criteria. The maximum sample area which can be illuminated by the DMD is 29.1 μm x 29.1 μm. The reason for this is that the DMD is illuminated by a circular profile laser beam, which underfills the DMD area to avoid scatter from the surrounding electronics and other parts of the device. This means that the detector FoV should be square with edges <20.6 μm at the sample as shown in Figure 48. As the short axis of the detector is 13.1 mm, a magnification of at least 636x is required to ensure the whole FoV is illuminated. As the tube lens and objective

were shared across the illumination and emission paths, this contributes 140x magnification, so a further 4.5x magnification was required. Therefore, a 40 mm lens was chosen for L6 (AC254-040-A, Thorlabs) and a 200 mm lens was chosen for L7 (AC254-200-A, Thorlabs) in a 4f configuration which resulted in a further 5x magnification. Taken together, the resultant is a 700x magnification. As illustrated in Figure 48, this means that the full FoV will be illuminated with a magnification factor that is over 5 fold higher than the Nyquist criteria dictates.

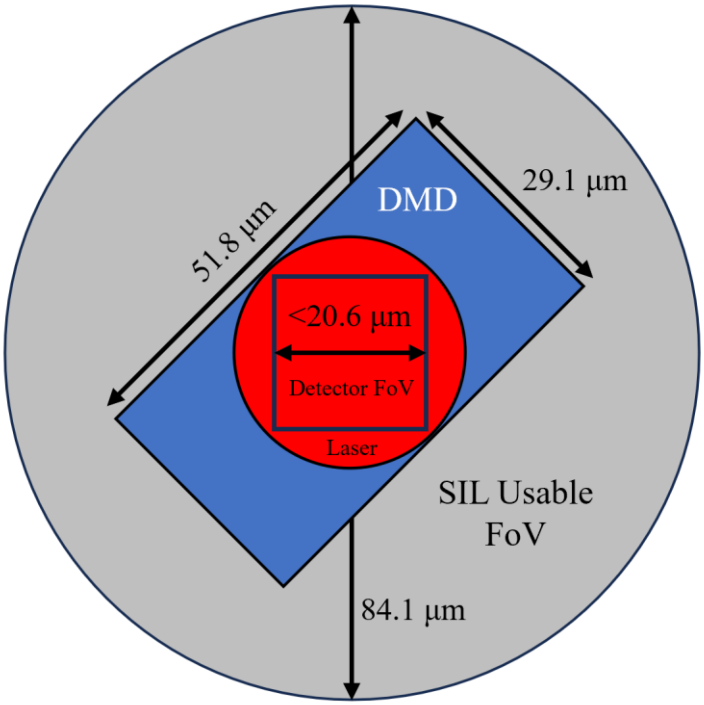


Figure 48 – Size of DMD, laser illumination beam and usable SIL LOD at sample. Constraint on detector FoV at sample is shown.

5.4.9 Emission Filter

Chromatic aberration, caused by materials having different refractive indices at different wavelengths, can affect the microscope performance, creating a blurring effect on the image. When an ASIL with a highly chromatically dispersive material is used, such as zirconia, this is of particular concern. With a structured illumination system where there is high frequency content in both the excitation and emission paths, this effect is even more of a concern. To alleviate this, a smaller ASIL can be used (see 5.2.2) and the spectral width of the light transmitted through the

ASIL can be reduced. In the illumination path, this can be achieved by using a narrow spectrum light source, such as the laser being used here. However, it is more difficult for the emission path where the light is emitted from a dye. Therefore, prior to the detector, I used a narrow band emission filter to limit the wavelengths entering the detector, which means that the imaged light at the detector experienced less refractive index variation through the system. For the previous application of this ASIL (Wang *et al.*, 2019), a 20 nm filter was deemed suitable, so as a first attempt, this was applied here too. This can be reduced if chromatic aberration causes problems as long as the brightness is still sufficient.

The only filter commercially available with a 20 nm bandwidth in this range has a central wavelength at 661 nm (FF01-661/20, Semrock), which is not well centred on the emission peak. The implication of this is that only around 35% of the emitted light will be transmitted to the detector.

5.4.10 Beam Expander

To produce a 'clean' Gaussian illumination beam of the correct size to illuminate the DMD, two appropriate lenses and a pin hole were required. A beam diameter of at least 7.4 mm was required to fill the DMD and the input beam diameter from the laser was 0.8 mm at the $1/e^2$ point. This meant that 9.2x magnification was required, so lenses of 15.29 mm and 150 mm in focal length were chosen for L1 and L2 respectively, which resulted in a beam diameter of 7.85mm at the DMD. An appropriate size pinhole was required to 'clean up' the beam which is around 30% larger than the diffraction limited spot size at the 99% contour (Thorlabs, 2023), given by:

$$D = \lambda \frac{f}{r} \qquad \textit{Equation 26}$$

Where λ is the wavelength of light, f is the focal length of L1 and r is the input beam at the $1/e^2$ point.

For a λ of 636 nm, L1 focal length of 15.29 mm and an input radius of 0.4 mm, this gives 24.31 µm as a value for D, meaning the pinhole should be around 31.6 µm, hence a 30 µm pinhole was chosen.

Unfortunately, due to time constraints, this part of the system was not fully implemented.

5.5 ASIL INTEGRATION

5.5.1 SIL Mounting

In previously published work using this ASIL design (Wang *et al.*, 2019) a disk was incorporated, the external dimensions of which matched a cryo-EM disk. This disk was mounted parallel to the flat face of the ASIL, level with the centre point of the sphere. This set-up was optimal for measuring cryogenically fixed cells but is unideal for imaging live bacteria.

An agarose pad, as used in Chapter 3 of this thesis, is the optimal choice for live cell imaging with *R. sphaeroides.* This required a flat surface for the agarose pad to be mounted on, meaning that the lens cannot protrude from the mounting surface as was the case with the previously reported mounting solution (see Figure 49a). In addition to allowing the mounting of samples by agarose pad, the new design also needed to facilitate the mounting of the ASIL on a microscope stage and as much as possible not obstruct the collection cone of the conventional objective.

To satisfy these requirements, I developed a new assembly where the ASIL was bonded into a coverslip, with the flat surface flush with the coverslip surface, which could then be placed onto microscope.

After several iterations of developing a glueing procedure, I adopted the process illustrated in Figure 49b. Standard #1.5 coverslips were drilled in the centre to create a 1 mm hole b)i) and b)ii).

Coverslips were drilled in piles of 5, with the outer two prone to extensive surface cracking. I experimented with multiple types of drills, but a stainless-steel drill bit (Figure 49c, left) appeared

to work best, producing an accurately sized hole without any surface cracks. This was slightly surprising, as one would expect that the diamond tip would have yielded better results. It may be the surface cracking observed was a function of the specific drill bit or drill used (Figure 49c, right).

After drilling, the coverslip was washed and dried to remove any excess debris and was subsequently placed upon a partially adhesive surface (3M) (b)iii). The flat surface of the ASIL was then stuck to this partially adhesive surface to ensure it remained static during the glueing process and that glue did not flow onto the flat surface of the ASIL, where the sample was to be placed. 2-part epoxy was applied using an eyelash attached to a cocktail stick, filling the small gap between the coverslip and ASIL (b)iv). An inspection microscope was used to ensure accurate placement of the epoxy. Once hardened, the whole assembly could be peeled off from the partially adhesive surface (b)v). Photographs of the final assembly (Figure 49d) show that the ASIL was secured without glue contaminating the flat surface, and with minimal contamination around the curved surface. This whole assembly was then be placed onto a Nickel sheet with dimensions matching those of a microscope slide, and finally secured with magnets (Figure 49e).

Whilst this configuration provides a flat surface for sample mounting, compared to the original design (Wang et al., 2019) this solution also exposes more of the lens to the collection cone of the conventional objective, increasing the NA. In the design described in Figure 49a, the maximum angle achievable was estimated at $\alpha = 56°$, but this design, the collection angle was estimated to be $\alpha = 66°$.

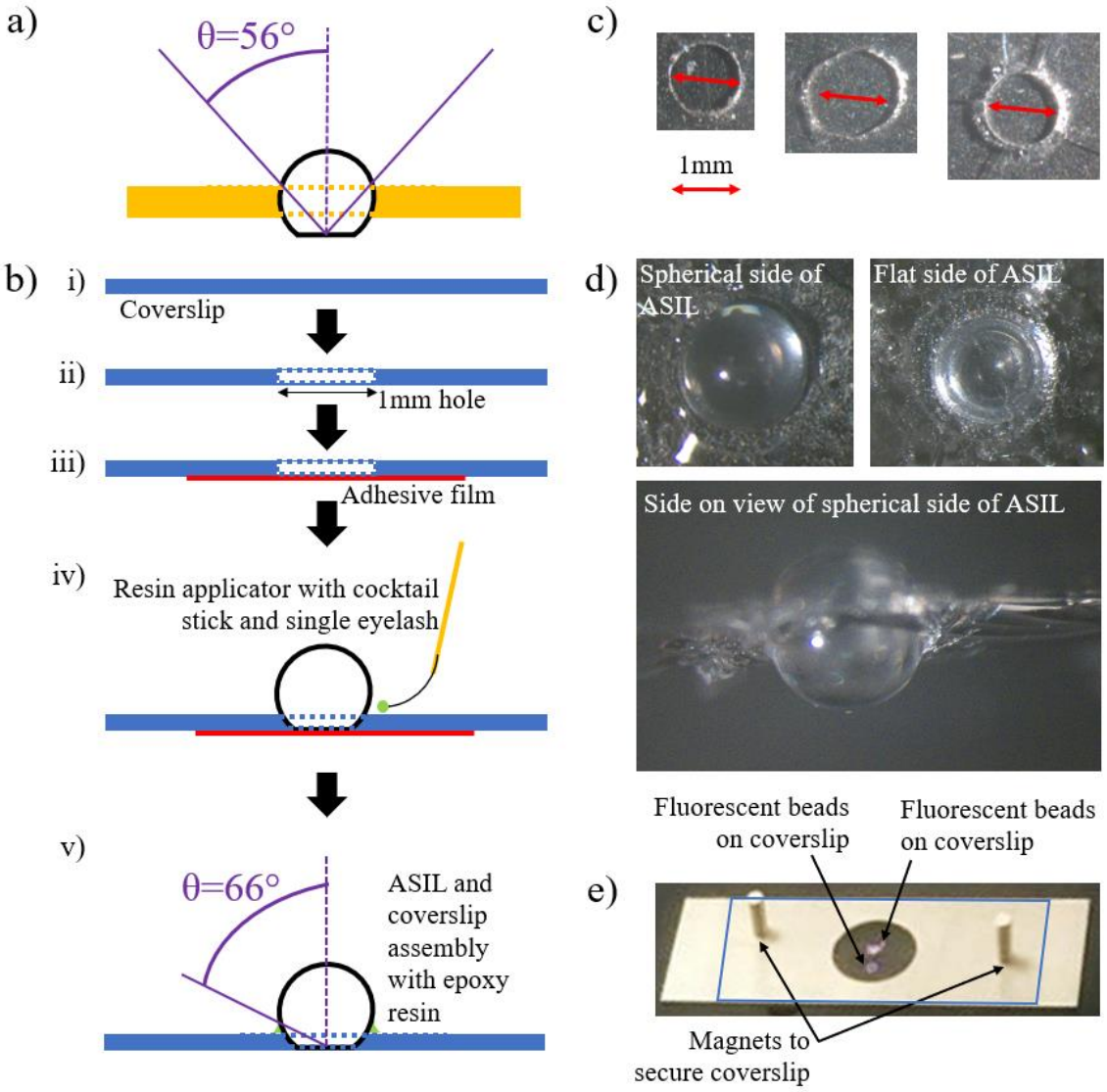


Figure 49 – a) Illustration of the design used in Wang et al., 2019 with estimated half angle of acceptance shown. b) Process for assembling an ASIL (white) into a #1.5 coverslip (blue) using a partially adhesive surface (red) to temporarily secure the SIL whilst the 2-part epoxy (green) is applied and cures. c) 1 mm (represented by red arrows) holes drilled into #1.5 coverslips using a stainless-steel drilling bit (left), an ultrasonic drill (centre), and diamond tipped drill (right). d) Photos of ASIL assembled into #1.5 coverslip taken through a microscope. e) Image of the ASIL/coverslip (edge highlighted in blue) assembly secured with magnets onto a nickel slide, making it compatible with a standard microscope stage. Purple dots are dense sub-diffraction limit fluorescent beads on and off the ASIL so both could be imaged without changing set-up.

5.5.2 Aligning the ASIL

Aligning the ASIL concentrically above the objective is critical to ensure aberration free imaging. This was done by adhering to the following 7-step operating procedure:

1) Turn on the transillumination LED.

2) Roughly align the ASIL above the objective by eye.

3) Course alignment using the camera and XY stage: The detector FoV is covering an area of 59 µm x 37 µm. Whilst this is a small area, the light dispersed by the ASIL covers a wide area and the intensity gradient can be used to adjust the XY stage to centre. As the intensity starts to plateau, adjust the focus tighten the spot, and repeat.

4) Once the small spot (see Figure 50a) is centred in the FoV, adjust the z-stage to focus the objective onto the curved surface of the ASIL. Use the XY stage to get the top of the curved ball as the sharpness maxima (see Figure 50b).

5) Slowly use the course stage at first to move the objective upwards by around 500 µm and then use the fine piezo z stage to bring the scratches on the flat surface into focus (see Figure 50c).

6) Turn off the transillumination LED and turn on the laser and adjust the course focus until the fluorescence signal is in focus.

7) L4 can be moved along the optical axis to refocus the pattern if required.

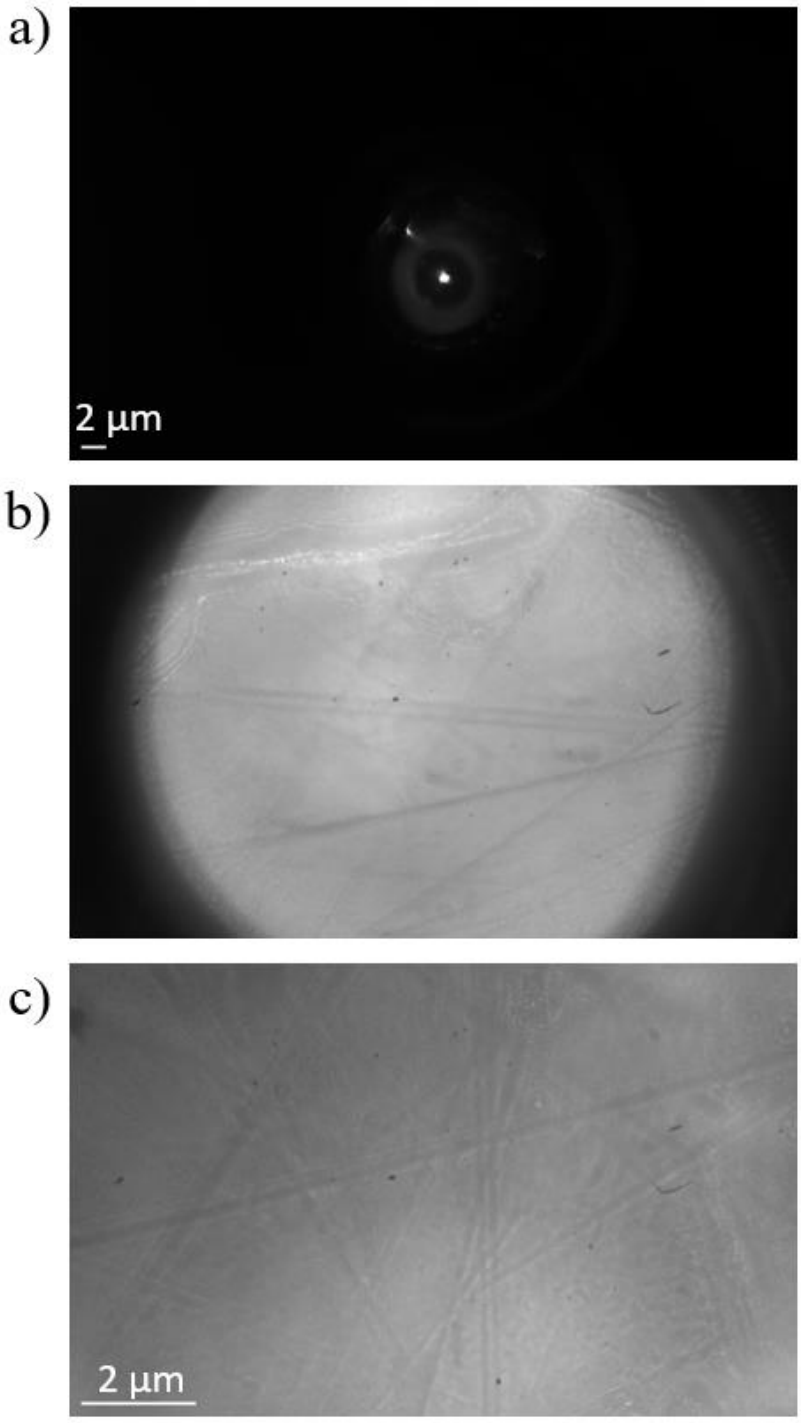


Figure 50 - Transillumination images of the ASIL during alignment: a) Locating the ASIL out of focus, b) finding the centre of the curved ASIL surface, c) focussed onto the flat ASIL surface. Scratches are a result of ASIL manufacturing processes. NOTE: The magnification in b) is not uniform across the image due to the focal plane being inside the ASIL, therefore no scale bar is shown.

5.6 SYSTEM VERIFICATION

5.6.1 Alignment verification

To ensure the SIM diffraction orders were centred on the back focal plane of the objective, the objective was removed and replaced with 2 different lengths of lens tube with an iris screwed into the top as shown in Figure 51a. The Fourier filter mask was removed and the DMD was set to cycle through 3 orientations of a pattern with a period of 12 pixels, fast enough so all patterns were simultaneously visible by eye. A piece of paper was then placed over the top and the laser power was adjusted so the image formed could be viewed safely.

The iris was closed until it started to cut-off the diffraction orders, and if this cut-off was equal for all diffraction orders in both iris positions, then the illumination path was well aligned. This is shown in the inset of Figure 51a.

The DMD was then set to show a static 12 pixel period pattern and power of the diffraction orders were measured using a laser power meter (Coherent), with the results shown in Figure 51b. There was only a 1.2% difference between the two side bands indicating good performance.

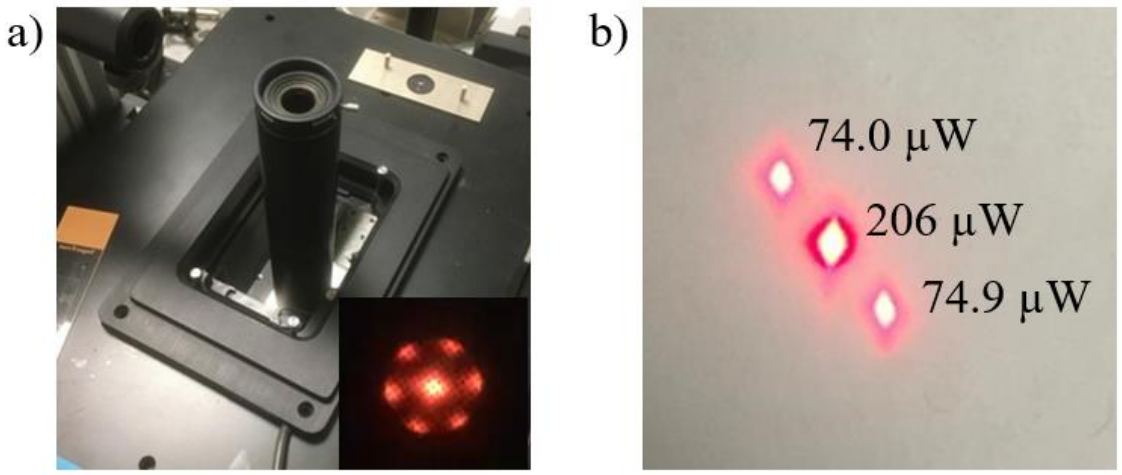


Figure 51 – a) Image of apparatus to test the alignment of diffraction orders with the resulting image as inset, which shows that all 6 1st order beams are blocked by the iris at the same point. b) 3 diffraction orders labelled with their power as measured just above the iris.

5.6.2 Magnification verification

To verify the magnification of the system without the ASIL, a DMD pattern with a 12-pixel period (90.72 μm/cycle) was used to provide structured illumination. The DMD pattern was imaged at the conjugate image plane between the dichroic mirrors D1 and D2 (Figure 52a) using a small CMOS camera (ace acA1920-40um, Basler). At this point, the period should be 22.68 μm/cycle, due to the 0.5x magnification between the DMD and the conjugate image plane and the period being halved by only using the 1st order diffraction beams.

The resulting images were analysed using FIJI with the pixel size set to the actual pixel size in the CMOS camera (5.86 μm). The Fast Fourier Transform (FFT) of the images was calculated (Figure 52b), and bright spots were observed at 22.8 μm, i.e. very close to the expected value of 22.68 μm.

Using a mirror in place of the sample above the conventional objective, the pattern was also imaged at the detector, as labelled in Figure 40 (Figure 52d). The expected pattern size at the image plane was 744 nm due to the further 0.032x magnification applied by the combination of L5 and the objective.

These images were also analysed in FIJI, with the pixel size set to the pixel size at the image plane (30.37 nm) and calculating the FFT (Figure 52e). Bright spots were observed at 730 nm/c, close to the predicted value (744 nm). For this result, I assumed that the detection path magnification was correct at 152.43x, as this was used to set the pixel size.

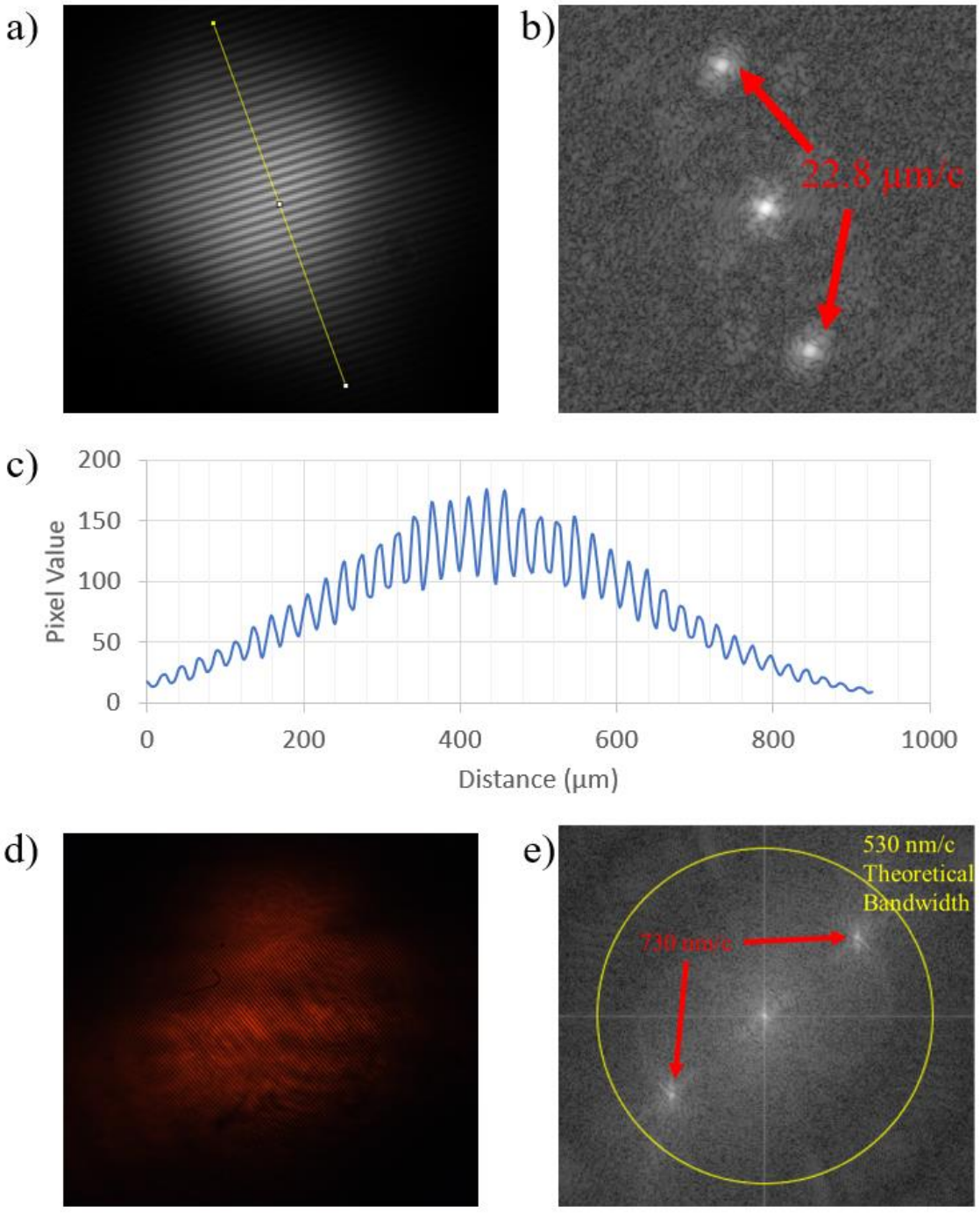


Figure 52 – Pattern magnification verification (without the ASIL) test with a 12-pixel period pattern at the DMD. a) Image at conjugate sample plane between D1 and D2 to test magnification of first 4f system and spatial filtering. b) FFT of (a) generated in ImageJ. c) Intensity profile of yellow line in (a). d) Image at main detector with pixel size set for the image plane where a mirror has been placed to reflect the excitation beam. e) FFT of (d) showing. The theoretical system bandwidth is shown in yellow.

However, when the same experiment was attempted with fluorescent beads and the emission filter in place, the pattern was much less clear, with frequency content at both the expected frequency and half that of the expected frequency. The results of this experiment are show in Figure 53. There was insufficient time to troubleshoot this problem. When focussing in a fluorescent sample, two striped illuminated areas were observed, presumably the contributions from each of the two diffraction orders. They came together in focus, but I suspect that this alignment was never good enough to create the required quality of interference. When attempting to focus into the ASIL, only one of these areas was visible, suggesting that both beams were not passing through the back focal plane.

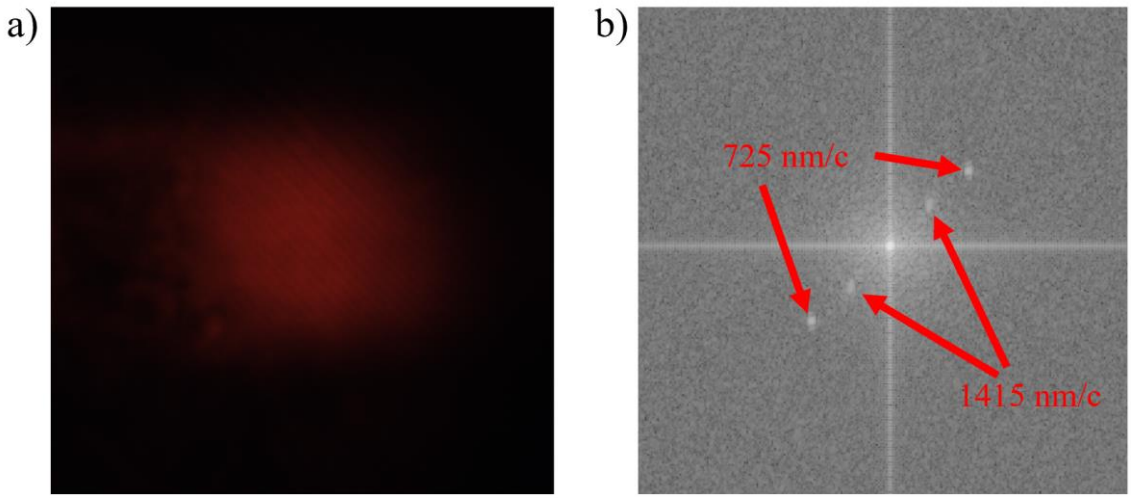


Figure 53 - Pattern magnification verification (without the ASIL) test results using patterns generated with a 12-pixel period pattern at the DMD. a) Image from the system detector from fluorescence. b) FFT of (a).

5.7 Discussion

Whilst time was the constraining factor in completing this work, the initial results are promising. Here I will outline a possible further steps that could be taken for the development of this system.

5.7.1 Future approach to addressing issues encountered using fluorescence

Reviewing the results in 5.6.2, a linear micrometer stage fitted to L4 to allow more accurate and precise focussing of the pattern would be a good first step. Achieving a high contrast SIM pattern at the sample may always be difficult without the TIRF illumination provided by the ASIL as out of focus fluorescence may cloud the image. Nevertheless, it would be expected that reduction of the 2 k-space spots at 1415 nm/c would be achievable with better focus.

I discovered a mistake in the calculation of the pattern size, which caused the observation of only one of the interfering beams being visible using ASIL. In 5.5.1 I concluded that the mounted ASIL has a maximum acceptance angle of around 66°, meaning that the NA would be around 1.98. This means that the maximum resolvable pattern would be 160 nm, and the pattern size used in this study was 161 nm. It was therefore practically impossible to achieve structured illumination with this pattern size and lens configuration. A better approach would be to properly quantify the NA of the ASIL using widefield fluorescence by setting the DMD to all off, and removing the mask and polarisers between L3 and L4. A fluorescence sample with heterogeneous spatial frequency content could be imaged and the NA could be calculated by measuring the system bandwidth from an FFT of the image. Once the bandwidth was known, a new pattern size of around 90% of the maximum detectable frequency could be constructed by changing the DMD period.

5.7.2 Further system quantification

Another key feature which needs to be quantified is the magnification from sample to the detector. This could be achieved simply using transillumination with a standard sample such as USAF 1951 and measuring the feature size at the detector.

Further investigation is also required to quantify the amount of chromatic aberration created by the system. This could be as simple as trying different emission filters with different bandwidths and observing the effect on pattern contrast.

The flat surface of the ASIL must be orthogonal to the optical axis to ensure the focal point is the same across the image. To test the quality of the ASIL mounting in the coverslip, the angle of the flat surface of the ASIL should be measured relative to the flat surface of the coverslip. This could be done by reflecting an inclined laser beam off the surface of the ASIL and detecting the reflection position relative to that of the coverslip in different orientations.

5.7.3 Further Development

Once the system is capable of single structured illumination frames, the next step would be to automate and synchronise the camera triggering and the DMD pattern change. The camera can be triggered using an external trigger input, as can the DMD, which can store all 12 patterns required to make 1 SIM frame in its internal memory. The synchronization would be done using the arrangement in Sandmeyer *et al.* where they use an Arduino Uno as a micro-controller which is internnaly controlled by FairSIM (Müller *et al.*, 2016) and μManager (Edelstein *et al.*, 2014) running on a PC. SIM frame reconstruction would also be carried out using FairSIM.

Sandmeyer *et al*. (2019) also use the microcontroller to turn on and off the laser, but this can cause laser intensity fluctuations, so instead, the sample illumination should be turned off by setting all the mirrors to the ON state.

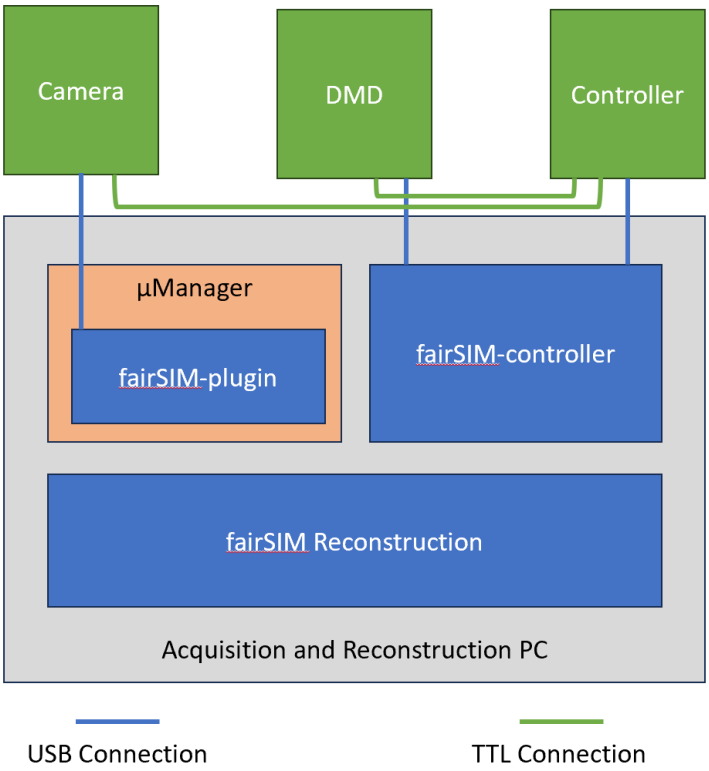


Figure 54 – Architecture of the proposed microscope control system, adapted from Sandmeyer *et al.*, (2019).

5.7.4 Sample Testing

The overall objective of development of a SIM/SIL microscope was to apply the system to the FtsZ 'ring' structure in *R. sphaeroides* (Chapter 1.3). However, the SIM/SIL system developed here may not be the best system to investigate this bacterial phenomenon with, at least initially. The reason for this is that FtsZ is not a membrane protein and therefore will be separated from the ASIL by both the inner and outer membranes, as well as the cell wall. Due to the TIRF illumination and resolution degradation which occurs deeper into samples, it may be that it is simply not possible to image this sample with the enhanced resolution, particularly once constriction starts to occur.

For verifying the performance of the system, synthetic samples such as distributions of fluorescence latex beads or DNA Origami rulers (GattaQuant), which consist of two fluorophores separated by a DNA structure of fixed length, could be used.

For verifying live cell performance, a potential candidate would be MreB in *Bacillus subtilis*, as this has been studied previously using TIRF-SIM (Hussain *et al.*, 2018) and would therefore allow comparison between convention TIRF-SIM and SIM/SIL.

5.7.5 Multicolour microscopy

The initial brief for this work included a requirement to facilitate 2 colour imaging. However, even ignoring time constraints, this would be very difficult to achieve. The high spectral dispersion of the zirconia ASIL and the wavelength dependency of the DMD illumination angle mean that for each colour channel a separate illumination system would have to be constructed. Integrating these channels whilst maintaining the polarisation of the illumination as discussed in 5.4.6 would be very challenging.

One proposed solution would be to use two fluorescent labels which can be excited using the same wavelength, but have Stokes shifts sufficiently different to allow them to be separated in the emission path. However, after having searched for the necessary equipment for this system (including dichroic mirrors, filters and fluorescent labels), it appears that this hypothetical solution cannot currently be realised with commercially available components. It therefore seems apparent that a multicolour SIM/SIL system is not practically achievable, at least when using a DMD Spatial Light Modulator and a zirconia ASIL.

5.8 Conclusions

Whilst the performance of a SIM/SIL system for live cell imaging could not be verified in the time available, there are some useful conclusions which can be drawn from the present work.

The first is that it is possible to adapt SIL to make it suitable for live cell imaging with an agarose pad, without substantially degrading the resolution. It is feasible that further improvements and adaptations could be made to the assembly process to construct the design in a repeatable manner.

Secondly, DMD appears to be a good method to create structured illumination patterns using coherent illumination, in a way where the pattern can be translated and rotated at speeds in excess of what is required for live cell imaging. This indicates that using a DMD with coherent illumination was a sensible approach to take in adapting SIM/SIL for live cell imaging.

Whilst the enhanced resolution of integrating a SIL into a SIM system makes it an attractive prospect, the lack of flexibility holds it back. The fact that the sample is coupled to the optical path preventing movement in X and Y to find a feature of interest, means that it will always be difficult to gather statistically significant data if the system were to be used in research practice. Another advantage of SIM is the flexibility in labelling options it provides, and this flexibility is partially lost due to the fact that the system will likely only feature one illumination wavelength and the fact that much of the emission will be lost due to the narrow band emission filters required to mitigate the chromatic aberration from the SIL.

There are certainly niches in fluorescence microscopy for life sciences such as operating in cryogenic conditions (Wang *et al.*, 2019) where SIL can prove useful. However, as a tool for simply improving spatial resolution in live cell imaging, based on the work conducted for this thesis, the downsides appear to outweigh the advantages.

6 CONCLUSIONS AND FUTURE DIRECTIONS

6.1 CONCLUSIONS

In this thesis I presented the blueprint for a SIM/SIL system, and laid the groundwork for using this system in combination with a range of other characterisation techniques to investigate the behaviour of proteins involved in cell division.

6.1.1 Applying SIM/SIL to imaging FtsZ and MipZ in *R. sphaeroides*

Whilst my original objective to image FtsZ and MipZ in *R. sphaeroides* using a combination of Structured Illumination Microscopy (SIM) and Solid Immersion Lens (SIL) was not achieved, useful conclusions can still be drawn from the work done on these proteins in isolation. Based on our current knowledge of FtsZ and MipZ across multiple bacterial species, a high-resolution SIM system with high temporal resolution would be incredibly valuable in assessing the structures and slower dynamics of both proteins. However, this would be of most value in 3D, in order to be able to observe the ring-like structures at mid-cell. Moving the focus position further into the cell with SIL will result in a degradation of NA, negating the purpose of the SIL. Wang *et al.*, (2019) used the same SIL and saw a 27% reduction in resolution moving from a 10 nm to 100 nm sample depth. As the sample depth continues to increase, the NA will trend towards the refractive index of the medium between the SIL and the sample (Wang, Pitter and Somekh, 2010), in this case around 1.39.

Where SIL could prove useful in this application is in TIRF imaging (Wang *et al.*, 2012) of the FtsZ ring-like structure at high frame rates, providing the user with high resolution. The limited field of view of SIL however is likely to limit its potential for collecting statistically significant data.

Despite not completing the microscope as designed, I believe that I have demonstrated that a live cell compatible SIM/SIL system is achievable. In the course of this DPhil project I have addressed

the main live cell incompatibilities of the design described previously (Wang, 2010; Wang, Pitter and Somekh, 2011b). These include the use of a DMD to speed up pattern generation and an improved method of mounting the SIL.

6.1.2 FtsZ and MipZ in *R. sphaeroides*

In this series of experiments, I imaged dynamic behaviour of FtsZ and MipZ using a novel labelling technique for α-proteobacteria. The data showed that MipZ is diffusing between the poles and mid-cell, seemingly dwelling at each of these locations, suggesting some kind of integration process. The data also showed the dynamic behaviour of FtsZ before constriction of the cell begins, which aligns with previous work (Chiu *et al.*, 2013; Dubarry *et al.*, 2019).

The *in vitro* work demonstrated no evidence of MipZ forming a high order polymer structure but much more work would be required to verify this finding. Given more time and my increased level of knowledge *in vitro* techniques, the experimental plan outlined in this thesis could yield some interesting insights into this biological system.

6.2 Future Directions

To build on the progress made in this work on live cell SIM/SIL, more time would be required to troubleshoot the structured illumination path where there appears to be two distinct problems. The first is that even without the ASIL, the two beams were not wall aligned at the sample plane which lead to a distorted illumination structure at the sample. Unless the two beams can be interfered properly at the sample plane, the contrast of the structured illumination will be too low and, in the case shown in Figure 53, the frequency will be wrong, creating a SIM image which is noisy with little, if any, resolution enhancement. To address this, I would ensure that the two beams entering the back focal plane of the objective are orthogonal to it, and that the point between the two beams is passing through the centre of it. This can be achieved by replacing the objective with a long tube, with irises at both ends. When the two beams pass through the centres of both irises, they are centred and orthogonal.

The second problem, as discussed in 5.7.1, is that theoretically determined pattern frequency was too high when the ASIL was used. To best way to address this would be to methodically increase the pattern frequency from course to the point at which the two beams are cut-off at the back focal plane of the objective. This would allow me to experimentally determine what a practical pattern frequency is, rather than relying on theory. The widefield bandwidth of the SIM system could also be tested by examining the PSF produced by sub-diffraction beads to determine what is the highest pattern frequency which can used.

It is likely these two approaches would have to be used iteratively to get a well aligned system with the optimal pattern frequency.

Once the system is operational the next step would be adding more excitation wavelengths and constructing a system to split the resulting colour channels. Adding more excitation wavelengths would introduce huge complexity to maintain the polarisation across all the channels and correct for chromatic aberration by defocussing each channel appropriately.

To push the spatial resolution as far as possible, the SIL could be changed from zirconia to diamond which would result in a 1.1-fold increase in NA but also reduce chromatic aberration. Then, rather than combining the SIL with linear SIM, non-liner SIM (Lu-Walther *et al.*, 2016) could be employed to go beyond two times the widefield bandwidth.

Moving to MipZ and FtsZ, the priority would be to find a fluorescent protein which is bright and photostable when compared to YFP and RFP used in Dubarry *et al.*, (2019), such as mNeonGreen or mScarlet. This would allow the use of dual colour 3D SIM for 3D imaging of the ring-like structure at mid-cell. Once MipZ and FtsZ images can be captured simultaneously, one could label FtsZ and a MipZ mutant on pIND to investigate whether the monomers, dimers, or a combination of both make up the MipZ ring-like structure at mid-cell.

Another approach which could be useful in examining the rings would be to image the cells end-on as is done in the VerCINI system from the Holden lab (Whitley *et al.*, 2022). Several imaging

modalities could be employed once the cells are supported end-on, such as 3D SIM or single particle tracking.

Finally, I believe there is a great amount of knowledge to be gained by complementing these advanced imaging modalities with *in vitro* work to further understand the relationship between MipZ and FtsZ. The HDX experiments in Corrales-Guerrero *et al.*, (2020, 2022) offer a unique way to learn more about the differences between MipZ and FtsZ binding in *R. sphaeroides* and *C. crescentus*. This approach provides an insight not achievable through fluorescence microscopy.

7 APPENDIX

7.1 BUFFERS AND MEDIA

Table 20 - M22 Media	
Ingredient	**Concentration**
1M Phosphate buffer	20ml/L
Concentrated Base	20ml/L
Growth Factor	2ml/L
$(NH4)_2$ SO_4 (Ammonium Sulphate)	0.5g/L
NaCl	0.5g/L
pH 7.2 with KOH	

Table 21 - 1M Phosphate buffer	
Ingredient	**Concentration**
K_2HPO_4 1M	174.18g/L
KH_2PO_4 1M	136.09g/L
pH 7 with KOH	

Table 22 - Concentrated Base	
Ingredient	**Concentration**
Nitrilotiracetic acid (diNa salt)	5.94g
Metals 44 solution	25ml
$MgSO_4$ $7H_2O$	14.5g/L
$CaCl_2$ $2H_2O$	1.67g/L
$FeSO_4$ $7H_2O$	50mg
Ammonium molybdate $4H_2O$ (B4) solution	4.6mg
pH to 6.8 with KOH	

Table 23 - Metals 44 Solution	
Ingredient	**Concentration**
Tetrasodium (EDTA)	2.5g/L
$ZnSO_4$ $7H_2O$	11g/L
$FESO_4$ $7H_2O$	5g/L
3M sulphuric acid	1.5ml/L
$MnSO_4$ $4H_2O$	2g/L
$CuSO_4$ $5H_2O$	0.39g/L
H_3BO_3 (boric acid)	0.12g/L
$CoCl_2$ $6H_2O$ (cobaltous chloride)	0.2g/L

Table 24 - Growth Factor	
Ingredient	**Concentration**
Biotin	20mg/L
$NaHCO_3$	500mg/L
Niacin (nicotinic acid)	1g/L
Thiamine HCl	500mg/L

Table 25 - LB / LB Agar	
Ingredient	**Concentration**
Tryptone	10g/L
Yeast Extract	5g/L
NaCl	10g/L
Agar (plates only)	20g/L

Table 26 - Succinate Media (Sux)	
Ingredient	**Concentration**
1M Phosphate buffer	20ml/L
Concentrated Base	20ml/L
Growth Factor	2ml/L
$(NH4)_2$ SO_4 (Ammonium Sulphate)	0.5g/L
NaCl	0.5g/L
Sodium succinate (6 H2O)	2g/L

Table 27 - FtsZ Buffer		
Ingredient	Concentration	Amount/L
Tris base (Merck)	50 mM	6.057 g/L
Imidazole (Merck)	20 mM	1.36 g/L
KCl (Merck)	300 mM	22.37g/L
HCl (Merck)	-	to pH8
DTT (Merck)	1 mM	0.154 g/L
Glycerol (ThermoFisher)	10%	100 ml/L

Table 28 - FtsZ Lysis Buffer		
Ingredient	**Concentration**	**Amount/L**
PMSF (Merck)	100 µg/ml	0.1 g/L
DNAse 1 (Roche)	10 µg/ml	0.01 g/L
EDTA free Complete (Roche)	1 tablet per 50ml	20 tablets/L
FtsZ buffer		to 1L

Table 29 - FtsZ Elution Buffer		
Ingredient	**Concentration**	**Amount/L**
Imidazole (Merck)	500 mM	32.68 g/L
FtsZ buffer		to 1L

Table 30 - MipZ Buffer		
Ingredient	**Concentration**	**Amount/L**
NaCl (Merck)	500mM	29.2 g/L
NaH_2PO_4 (Merck)	50mM	6 g/L
Imidazole (Merck)	20mM	1.36 g/L
DTT (Merck)	1mM	2 ml/L
NaOH (Merck)	-	to pH8

Table 31 - MipZ Lysis Buffer		
Ingredient	**Concentration**	**Amount/L**
PMSF (Merck)	100 µg/ml	0.1 g/L
DNAse 1 (Roche)	10 µg/ml	0.01 g/L
EDTA free Complete (Roche)	1 tablet per 50ml	20 tablets/L
MipZ buffer		to 1L

Table 32 - MipZ Elution Buffer		
Ingredient	**Concentration**	**Amount/L**
Imidazole (Merck)	500 mM	32.68 g/L
MipZ buffer		to 1L

Table 33 - MipZ Storage Buffer		
Ingredient	**Concentration**	**Amount/L**
Hepes (Merck)	50 mM	11.915 g/L
KCl (Merck)	50 mM	3.725 g/L
MgCl Hexahydrate (Merck)	5 mM	1.015 g/L
NaOH (Merck)	-	to pH 8
Glycerol (ThermoFisher)	10%	100 ml/L

Table 34 - Antibiotics	
Antibiotic	**Concentration**
Nalidixic acid	100µg/ml
Kanamycin	100µg/ml
Ampicillin	100µg/ml

7.2 List of Primers

Plasmid ID	Sequence	Related Plasmid
priSM0001	CTCAGCTAATTAAGCTTTTAACCGGAAATCTCCAGAGTAGacag	pSM0001
priSM0002	AGGCAAACGGATCCAGATCTGAAATCGGTACTGGCTTTCcattcg	pSM0001
priSM0003	gGAAAGCCAGTACCGATTTCAGATCTGGATCCGTTTGCCT	pSM0001
priSM0004	CTACTCTGGAGATTTCCGGTTAAAAGCTTAATTAGCTGAGCTTGGACT	pSM0001
priSM0005	GCCAGTGCCAAGCTTGCATGagaggtcggccagcg	pSM0002
priSM0006	tgggcaagcctgggctgggttgatccccggcccaagg	pSM0002
priSM0007	ctcccttgggccggggatcaacccagcccaggcttg	pSM0002
priSM0008	TGAAGCCCGACTTCAGATCTatggacaaagactgcgaaatgaagc	pSM0002
priSM0009	atttcgcagtctttgtccatAGATCTGAAGTCGGGCTTCACC	pSM0002
priSM0010	TATGACCATGATTACGAATTTCCTGATCGACTGCCCCGG	pSM0002
priSM0011	GCCGGGGCAGTCGATCAGGAAATTCGTAATCATGGTCATAGCTGTTTCCTGTGTGA	pSM0002
priSM0012	ggaggcgctggccgacctctCATGCAAGCTTGGCACTGGCC	pSM0002
priSM0017	agaacctgtattttcagggcatggcactcaacctcatgatgaacaac	pSM0004
priSM0018	cagcttcctttcgggctttgtcagtttgcctgacgccgc	pSM0004
priSM0019	tgcggcgtcaggcaaactgacaaagcccgaaaggaagc	pSM0004
priSM0020	atcatgaggttgagtgccatgccctgaaaatacaggttctcatg	pSM0004
priSM0021	GCTTTTATTAACCGGAAATCTCCAGAGTAGacag	pSM0001
priSM0022	ATCCAGATCTGAAATCGGTACTGGCTTTCcattcg	pSM0001
priSM0023	TACCGATTTCAGATCTGGATCCGTTTGCCT	pSM0001
priSM0024	AGATTTCCGGTTAATAAAAGCTTAATTAGCTGAGCTTGGACTCC	pSM0001
priSM0029	ttttcagggcatggcactcaacctcatgat	pSM0007
priSM0030	tcgggctttgtcagtttgcctgacgcc	pSM0007
priSM0031	ggcaaactgacaaagcccgaaaggaag	pSM0007
priSM0032	tgagtgccatgccctgaaaatacaggt	pSM0007
priSM0080	ttgggccggggatcaACCGGAAATCTCCAGAG	pSM0022
priSM0081	CTGAAGCTGCCGGG	pSM0022
priSM0082	GAAGTCGGGCTTCACCC	pSM0022
priSM0083	CTGGAGATTTCCGGTtgatccccggccc	pSM0022

Table 35 - List of primers used in this study.

7.3 HISTRAP FF ELUTION PROTOCOL

```
UNICORN 7.0                                                    1(6)
User: Default  16/07/2020 15:19:03 +01:00
Method: HisTrapExcel_1ml

Text instructions
Main method:
  0.00   Base: CV, 0.962 {ml}, (HisTrap FF, 1 ml)#Column type
  0.00   Phase: Method Settings
    0.00   Base: SameAsMain
    0.00   Alarm pre column pressure: Enabled, (0.50)#Pre column pressure
    limit {MPa}, 0.00 {MPa}
    0.00   Wavelength: (280)#UV1 {nm}, (Off)#UV2 {nm}, (Off)#UV3 {nm}
    0.00   Noise reduction UV: (5.0)#UV averaging time {sec}
    0.00   Injection valve: Manual load
    0.00   System flow: (1.000)#Flow rate {ml/min}, (Pre column pressure)
    #Pressure control
    0.00   End_Block
  0.00   Phase: Column Wash
    0.00   Base: SameAsMain
    0.00   Gradient: (0.0)#Percent B (Column Wash) {%B}, 0.00 {base}
    0.00   System flow: (1.000)#Flow rate {ml/min}, (Pre column pressure)
    #Pressure control
    0.00   Block: Start frac (Column Wash)
      0.00   Base: SameAsMain
      0.00   Last tube filled: (Pause)#Last tube filled action (Column
      Wash)
      0.00   Fractionation: Volume, (50 ml tubes)#Frac tube type (Column
      Wash), (45.0)#Frac volume (Column Wash) {ml}, (Next tube)#Frac start
      position (Column Wash)
      0.00   End_Block
    0.00   Block: Wash
      0.00   Base: SameAsMain
      (8.00)#Column wash volume   End_Block
    0.00   Block: Stop frac (Column Wash)
      0.00   Base: SameAsMain
      0.00   Stop fractionation
      0.00   End_Block
    0.00   End_Block
  0.00   Phase: Elution
    0.00   Base: SameAsMain
    0.00   Gradient: (0.0)#Percent B (Elution) {%B}, 0.00 {base}
    0.00   System flow: (1.000)#Flow rate {ml/min}, (Pre column pressure)
    #Pressure control
    0.00   Block: Start frac (Elution)
      0.00   Base: SameAsMain
      0.00   Last tube filled: (Pause)#Last tube filled action (Elution)
      0.00   Fractionation: Volume, (96 deep well plate)#Frac tube type
      (Elution), (0.40)#Frac volume (Elution) {ml}, (Next tube)#Frac start
      position (Elution)
      0.00   End_Block
    0.00   Block: Linear gradient
      0.00   Base: SameAsMain
```

```
      0.00   Gradient: (100.0)#Gradient target (Elution) {%B}, (20.00)
      #Gradient length (Elution) {base}
      20.00   End_Block
    0.00   Block: Gradient delay
      0.00   Base: Volume, ColumnSameAsMain
      (3.00)#Gradient delay volume   End_Block
    0.00   Block: Stop frac (Elution)
      0.00   Base: SameAsMain
      0.00   Stop fractionation
      0.00   End_Block
    0.00   End_Block
  0.00   Phase: Column Wash
    0.00   Base: SameAsMain
    0.00   Gradient: (100.0)#Percent B (Column Wash)_1 {%B}, 0.00 {base}
    0.00   System flow: (1.000)#Flow rate {ml/min}, (Pre column pressure)
    #Pressure control
    0.00   Block: Wash_1
      0.00   Base: SameAsMain
      (5.00)#Column wash volume_1   End_Block
    0.00   End_Block
  0.00   Phase: Equilibration
    0.00   Base: SameAsMain
    0.00   Gradient: (0.0)#Percent B (Equilibration)_1 {%B}, 0.00 {base}
    0.00   System flow: (1.000)#Flow rate {ml/min}, (Pre column pressure)
    #Pressure control
    0.00   System wash: (15)#Fill system (Equilibration)_1 {ml}
    0.00   Block: Equilibrate_1
      0.00   Base: SameAsMain
      (5.00)#Equilibration volume_1   End_Block
    0.00   End_Block
```

Method duration

```
Base:Time
Unit:min
```

Main method:

```
  0.00   Base: CV, 0.962 {ml}, (HisTrap FF, 1 ml)#Column type
  0.00   Phase: Method Settings
    0.00   Base: SameAsMain
    0.00   Alarm pre column pressure: Enabled, (0.50)#Pre column pressure
    limit {MPa}, 0.00 {MPa}
    0.00   Wavelength: (280)#UV1 {nm}, (Off)#UV2 {nm}, (Off)#UV3 {nm}
    0.00   Noise reduction UV: (5.0)#UV averaging time {sec}
    0.00   Injection valve: Manual load
    0.00   System flow: (1.000)#Flow rate {ml/min}, (Pre column pressure)
    #Pressure control
    0.00   End_Block
```

User: Default 16/07/2020 15:19:03 +01:00
Method: HisTrapExcel_1ml

```
0.00   Phase: Column Wash
  0.00   Base: SameAsMain
  0.00   Gradient: (0.0)#Percent B (Column Wash) {%B}, 0.00 {base}
  0.00   System flow: (1.000)#Flow rate {ml/min}, (Pre column pressure)
  #Pressure control
  0.00   Block: Start frac (Column Wash)
    0.00   Base: SameAsMain
    0.00   Last tube filled: (Pause)#Last tube filled action (Column
    Wash)
    0.00   Fractionation: Volume, (50 ml tubes)#Frac tube type (Column
    Wash), (45.0)#Frac volume (Column Wash) {ml}, (Next tube)#Frac start
    position (Column Wash)
    0.00   End_Block
  0.00   Block: Wash
    0.00   Base: SameAsMain
    (7.70)#Column wash volume   End_Block
  7.70   Block: Stop frac (Column Wash)
    7.70   Base: SameAsMain
    7.70   Stop fractionation
    7.70   End_Block
  7.70   End_Block
7.70   Phase: Elution
  7.70   Base: SameAsMain
  7.70   Gradient: (0.0)#Percent B (Elution) {%B}, 0.00 {base}
  7.70   System flow: (1.000)#Flow rate {ml/min}, (Pre column pressure)
  #Pressure control
  7.70   Block: Start frac (Elution)
    7.70   Base: SameAsMain
    7.70   Last tube filled: (Pause)#Last tube filled action (Elution)
    7.70   Fractionation: Volume, (96 deep well plate)#Frac tube type
    (Elution), (0.40)#Frac volume (Elution) {ml}, (Next tube)#Frac start
    position (Elution)
    7.70   End_Block
  7.70   Block: Linear gradient
    7.70   Base: SameAsMain
    7.70   Gradient: (100.0)#Gradient target (Elution) {%B}, (20.00)
    #Gradient length (Elution) {base}
    26.94   End_Block
  26.94   Block: Gradient delay
    26.94   Base: Volume, ColumnSameAsMain
    (29.94)#Gradient delay volume   End_Block
  29.94   Block: Stop frac (Elution)
    29.94   Base: SameAsMain
    29.94   Stop fractionation
    29.94   End_Block
  29.94   End_Block
29.94   Phase: Column Wash
  29.94   Base: SameAsMain
  29.94   Gradient: (100.0)#Percent B (Column Wash)_1 {%B}, 0.00 {base}
```

User: Default 16/07/2020 15:19:03 +01:00
Method: HisTrapExcel_1ml

```
    29.94   System flow: (1.000)#Flow rate {ml/min}, (Pre column pressure)
    #Pressure control
    29.94   Block: Wash_1
      29.94   Base: SameAsMain
      (34.75)#Column wash volume_1   End_Block
    34.75   End_Block
  34.75   Phase: Equilibration
    34.75   Base: SameAsMain
    34.75   Gradient: (0.0)#Percent B (Equilibration)_1 {%B}, 0.00 {base}
    34.75   System flow: (1.000)#Flow rate {ml/min}, (Pre column pressure)
    #Pressure control
    34.75   System wash: (15)#Fill system (Equilibration)_1 {ml}
    34.75   Block: Equilibrate_1
      34.75   Base: SameAsMain
      (39.56)#Equilibration volume_1   End_Block
    39.56   End_Block

Total Volume (approximately):39.56 ml
Total Time (approximately):39.56 min
```

Variable list

Phase	Block	Variable	Value	Unit
Method Settings	Main	Column type	HisTrap FF, 1 ml	
Method Settings	METHOD SETTINGS	Pre column pressure limit	0.50	{MPa}
		UV1	280	{nm}
		UV2	Off	{nm}
		UV3	Off	{nm}
		UV averaging time	5.0	{sec}
Method Settings,...	METHOD SETTINGS,...	Flow rate	1.000	{ml/min}
		Pressure control	Pre column pressure	
Column Wash	COLUMN WASH	Percent B (Column Wash)	0.0	{%B}
Column Wash	Start frac (Column Wash)	Last tube filled action (Column Wash)	Pause	
		Frac tube type (Column Wash)	50 ml tubes	
		Frac volume (Column Wash)	45.0	{ml}

Phase	Block	Variable	Value	Unit
		Frac start position (Column Wash)	Next tube	
Column Wash	Wash	Column wash volume	8.00	{CV}
Elution	ELUTION	Percent B (Elution)	0.0	{%B}
Elution	Start frac (Elution)	Last tube filled action (Elution)	Pause	
		Frac tube type (Elution)	96 deep well plate	
		Frac volume (Elution)	0.40	{ml}
		Frac start position (Elution)	Next tube	
Elution	Linear gradient	Gradient target (Elution)	100.0	{%B}
		Gradient length (Elution)	20.00	{base}
Elution	Gradient delay	Gradient delay volume	3.00	{ml}
Column Wash	COLUMN WASH_1	Percent B (Column Wash)_1	100.0	{%B}
Column Wash	Wash_1	Column wash volume_1	5.00	{CV}
Equilibration	EQUILIBRATION_1	Percent B (Equilibration)_1	0.0	{%B}
		Fill system (Equilibration)_1	15	{ml}
Equilibration	Equilibrate_1	Equilibration volume_1	5.00	{CV}

Method information

Properties:

Method name: HisTrapExcel_1ml
Method created by: Default
Date of creation: 11/06/2020 15:14:36 +01:00
Created for system: Akta PURE 01

User: Default 16/07/2020 15:19:03 +01:00
Method: HisTrapExcel_1ml

Date of last modification: 11/06/2020 15:17:13 +01:00
Method last modified by: Default

Strategy name: Npn2F091

Start protocol

Method Items to display at method start:
Result Name And Location

Result name and location

Result folder name: /DefaultHome
Result name: HisTrapExcel_1ml (Type: Method name) without unique identifier

Columns

HisTrap FF, 1 ml
Run Parameters

Technique	Affinity	
Column volume	0.962	ml
Max pre-column pressure	0.50	MPa
Max delta column pressure	0.30	MPa
Default flow rate	1.00	ml/min
Max flow rate	4.00	ml/min
Default linear flow rate	155.91	cm/h
Max linear flow rate	623.63	cm/h
Min pH value (short term)	2	
Max pH value (short term)	14	
Min pH value (long term)	3	
Max pH value (long term)	12	

Details

Hardware diameter	0.70	cm
Bed height	2.50	cm
Typical loading range	1-100	mg
Total liquid volume (Vt)	0.86	ml
Void volume (Vo)		ml
Typical peak width at base	3.00	ml
Average particle diameter	90.00	µm
Molecular weight range		Mr

Ordering information

Name	HisTrap FF, 1 ml
Code number	17-5319-01
Medium name	Ni Sepharose 6 Fast Flow
Medium code number	17-5318-02
Hardware name	HiTrap, 1 ml
Hardware code number	

7.4 SIZE EXCLUSION CHROMATOGRAPHY PROTOCOL

```
UNICORN 7.0                                                    1(7)
User: Default  7/16/2020 3:19:52 PM +01:00
Method: Hiload_superdex_75_short

Text instructions
Main method:
  0.00   Base: CV, 120.637 {ml}, (HiLoad 16/60 Superdex 75 pg)#Column type
  0.00   Phase: Method Settings
    0.00   Base: SameAsMain
    0.00   Alarm pre column pressure: Enabled, (0.50)#Pre column pressure
    limit {MPa}, 0.00 {MPa}
    0.00   Noise reduction UV: (5.0)#UV averaging time {sec}
    0.00   Injection valve: Manual load
    0.00   System flow: (1.000)#Flow rate {ml/min}, (Pre column pressure)
    #Pressure control
    0.00   End_Block
  0.00   Phase: Column Wash
    0.00   Base: SameAsMain
    0.00   Gradient: (0.0)#Percent B (Column Wash) {%B}, 0.00 {base}
    0.00   System flow: (1.000)#Flow rate {ml/min}, (Pre column pressure)
    #Pressure control
    0.00   System wash: (15)#Fill system (Column Wash) {ml}
    0.00   Block: Wash
      0.00   Base: SameAsMain
      (1.00)#Column wash volume   End_Block
    0.00   End_Block
  0.00   Phase: Equilibration
    0.00   Base: SameAsMain
    0.00   Gradient: (100.0)#Percent B (Equilibration) {%B}, 0.00 {base}
    0.00   System flow: (1.000)#Flow rate {ml/min}, (Pre column pressure)
    #Pressure control
    0.00   System wash: (15)#Fill system (Equilibration) {ml}
    0.00   Block: Hold until UV stable signal
      0.00   Base: Time, Any
      0.00   Watch UV parameters: 0.00 {mAU}, 1.00 {mAU}
      0.00   Hold until: UV, Stable signal, 0.03 {min}, 5.00 {base}
      0.00   End_Block
    0.00   Auto zero UV
    0.00   Block: Equilibrate
      0.00   Base: SameAsMain
      (1.10)#Equilibration volume   End_Block
    0.00   Auto zero UV
    0.00   End_Block
  0.00   Phase: Miscellaneous
    0.00   Base: SameAsMain
    0.00   Message: (Inject Sample)#Message, Screen, Default sound
    0.00   Pause: Infinite {min}
    0.00   End_Block
```

User: Default 7/16/2020 3:19:52 PM +01:00
Method: Hiload_superdex_75_short

```
  0.00   Phase: Sample Application
    0.00   Base: SameAsMain
    0.00   Block: Prepare sample loading
      0.00   Base: SameAsMain
      0.00   Set mark: ()#Sample_ID
      0.00   End_Block
    0.00   Block: Inject
      0.00   Base: Volume, ColumnSameAsMain
      0.00   Gradient: (100.0)#Percent B (Sample Appl) {%B}, 0.00 {base}
      0.00   Injection valve: Inject
      0.00   System flow: (1.000)#Flow rate {ml/min}, (Pre column pressure)
      #Pressure control
      (5.00)#Empty loop with   End_Block
    0.00   Injection valve: Manual load
    0.00   End_Block
  0.00   Phase: Elution
    0.00   Base: SameAsMain
    0.00   Gradient: (100.0)#Percent B (Elution) {%B}, 0.00 {base}
    0.00   System flow: (1.000)#Flow rate {ml/min}, (Pre column pressure)
    #Pressure control
    0.00   Block: Start frac (Elution)
      0.00   Base: SameAsMain
      0.00   Fractionation: Volume, (1.00)#Frac volume (Elution) {ml}
      0.00   End_Block
    0.00   Block: Isocratic
      0.00   Base: SameAsMain
      (1.00)#Isocratic elution length   End_Block
    0.00   Block: Stop frac (Elution)
      0.00   Base: SameAsMain
      0.00   Stop fractionation
      0.00   End_Block
    0.00   End_Block
```

Method duration

```
Base:Time
Unit:min
```

Main method:

```
  0.00   Base: CV, 120.637 {ml}, (HiLoad 16/60 Superdex 75 pg)#Column type
  0.00   Phase: Method Settings
    0.00   Base: SameAsMain
    0.00   Alarm pre column pressure: Enabled, (0.50)#Pre column pressure
    limit {MPa}, 0.00 {MPa}
```

```
    0.00   Noise reduction UV: (5.0)#UV averaging time {sec}
    0.00   Injection valve: Manual load
    0.00   System flow: (1.000)#Flow rate {ml/min}, (Pre column pressure)
    #Pressure control
    0.00   End_Block
  0.00   Phase: Column Wash
    0.00   Base: SameAsMain
    0.00   Gradient: (0.0)#Percent B (Column Wash) {%B}, 0.00 {base}
    0.00   System flow: (1.000)#Flow rate {ml/min}, (Pre column pressure)
    #Pressure control
    0.00   System wash: (15)#Fill system (Column Wash) {ml}
    0.00   Block: Wash
      0.00   Base: SameAsMain
      (120.64)#Column wash volume   End_Block
    120.64   End_Block
  120.64   Phase: Equilibration
    120.64   Base: SameAsMain
    120.64   Gradient: (100.0)#Percent B (Equilibration) {%B}, 0.00 {base}
    120.64   System flow: (1.000)#Flow rate {ml/min}, (Pre column pressure)
    #Pressure control
    120.64   System wash: (15)#Fill system (Equilibration) {ml}
    120.64   Block: Hold until UV stable signal
      120.64   Base: Time, Any
      120.64   Watch UV parameters: 0.00 {mAU}, 1.00 {mAU}
      120.64   Hold until: UV, Stable signal, 0.03 {min}, 5.00 {base}
      120.64   End_Block
    120.64   Auto zero UV
    120.64   Block: Equilibrate
      120.64   Base: SameAsMain
      (253.34)#Equilibration volume   End_Block
    253.34   Auto zero UV
    253.34   End_Block
  253.34   Phase: Miscellaneous
    253.34   Base: SameAsMain
    253.34   Message: (Inject Sample)#Message, Screen, Default sound
    253.34   Pause: Infinite {min}
    253.34   End_Block
  253.34   Phase: Sample Application
    253.34   Base: SameAsMain
    253.34   Block: Prepare sample loading
      253.34   Base: SameAsMain
      253.34   Set mark: ()#Sample_ID
      253.34   End_Block
    253.34   Block: Inject
```

```
      253.34   Base: Volume, ColumnSameAsMain
      253.34   Gradient: (100.0)#Percent B (Sample Appl) {%B}, 0.00 {base}
      253.34   Injection valve: Inject
      253.34   System flow: (1.000)#Flow rate {ml/min}, (Pre column
      pressure)#Pressure control
      (258.34)#Empty loop with   End_Block
    258.34   Injection valve: Manual load
    258.34   End_Block
  258.34   Phase: Elution
    258.34   Base: SameAsMain
    258.34   Gradient: (100.0)#Percent B (Elution) {%B}, 0.00 {base}
    258.34   System flow: (1.000)#Flow rate {ml/min}, (Pre column pressure)
    #Pressure control
    258.34   Block: Start frac (Elution)
      258.34   Base: SameAsMain
      258.34   Fractionation: Volume, (1.00)#Frac volume (Elution) {ml}
      258.34   End_Block
    258.34   Block: Isocratic
      258.34   Base: SameAsMain
      (378.97)#Isocratic elution length   End_Block
    378.97   Block: Stop frac (Elution)
      378.97   Base: SameAsMain
      378.97   Stop fractionation
      378.97   End_Block
    378.97   End_Block

Total Volume (approximately):378.97 ml
Total Time (approximately):378.97 min
```

Variable list

Phase	Block	Variable	Value	Unit
Method Settings	Main	Column type	HiLoad 16/60 Superdex 75 pg	
Method Settings	METHOD SETTINGS	Pre column pressure limit	0.50	{MPa}
		UV averaging time	5.0	{sec}
Method Settings,...	METHOD SETTINGS,...	Flow rate	1.000	{ml/min}

Phase	Block	Variable	Value	Unit
		Pressure control	Pre column pressure	
Column Wash	COLUMN WASH	Percent B (Column Wash)	0.0	{%B}
		Fill system (Column Wash)	15	{ml}
Column Wash	Wash	Column wash volume	1.00	{CV}
Equilibration	EQUILIBRATION	Percent B (Equilibration)	100.0	{%B}
		Fill system (Equilibration)	15	{ml}
Equilibration	Equilibrate	Equilibration volume	1.10	{CV}
Miscellaneous	MISCELLANEOUS	Message	Inject Sample	
Sample Application	Prepare sample loading	Sample_ID		
Sample Application	Inject	Percent B (Sample Appl)	100.0	{%B}
		Empty loop with	5.00	{ml}
Elution	ELUTION	Percent B (Elution)	100.0	{%B}
Elution	Start frac (Elution)	Frac volume (Elution)	1.00	{ml}
Elution	Isocratic	Isocratic elution length	1.00	{CV}

Method information
Properties:
Method name: Hiload_superdex_75_short
Method created by: Default
Date of creation: 6/25/2020 3:33:49 PM +01:00
Created for system: AKTA Pure 2
Date of last modification: 6/25/2020 3:33:49 PM +01:00

User: Default 7/16/2020 3:19:52 PM +01:00
Method: Hiload_superdex_75_short

Method last modified by: Default

Strategy name: AKTApure25_105

Start protocol

Method Items to display at method start:
Result Name And Location

Result name and location

Result folder name: /DefaultHome
Result name: Hiload_superdex_75_short (Type: Method name) without unique identifier

Columns

HiLoad 16/60 Superdex 75 pg
Run Parameters

Technique	GelFiltration	
Column volume	120.637	ml
Max pre-column pressure	0.50	MPa
Max delta column pressure	0.30	MPa
Default flow rate	1.00	ml/min
Max flow rate	1.60	ml/min
Default linear flow rate	29.84	cm/h
Max linear flow rate	47.75	cm/h
Min pH value (short term)	1	
Max pH value (short term)	14	
Min pH value (long term)	3	
Max pH value (long term)	12	

Details

Hardware diameter	1.60	cm
Bed height	60.00	cm
Typical loading range	0.6-5	ml
Total liquid volume (Vt)		ml
Void volume (Vo)	39.81	ml
Typical peak width at base	10.00	ml
Average particle diameter	34.00	µm
Molecular weight range	3000-70000	Mr

Ordering information

Name	HiLoad 16/60 Superdex 75 pg
Code number	17-1068-01
Medium name	Superdex 75 prep grade

User: Default 7/16/2020 3:19:52 PM +01:00
Method: Hiload_superdex_75_short

Medium code number	17-1044-01
Hardware name	XK 16/70
Hardware code number	28-9889-46

7.5 IMAGE OVERLAY CODE

```
//Switch for presence of data in green channel
greenChannel=0;
//SET TO NUMBER OF SLICES BEFORE RUN
n = 1000;

id=getImageID();
imageName=getTitle()
selectImage(id);

//Select green chanel and duplicate
if (greenChannel==1) {
	makeRectangle(0, 0, 428, 684);
	run("Duplicate...","duplicate");
	titleLeft=getTitle();
	selectImage(id);
}

//Select right red channel and duplicate
makeRectangle(428, 0, 428, 684);
run("Duplicate...","duplicate");
titleRight=getTitle();

//'Calculate' the name of the BF image
dashIndex=indexOf(imageName, "-");
titleLength=lengthOf(imageName);
print("titlelength", titleLength);
print("dashIndex", dashIndex);

if(dashIndex!=-1){
	titleGrey=substring(imageName,0,dashIndex)+"-BF.tif";
	print(titleGrey);
} else{
	titleGrey=substring(imageName,0,15) + ".tif";
}

//Select BF image and crop
selectWindow(titleGrey);
makeRectangle(0, 0, 428, 684);
run("Crop");

//create a BF frame from every EF frame
setBatchMode("hide");
imgID = getImageID();
title = getTitle();
for (i = 0; i < n; i++) {
selectImage(imgID);
run("Duplicate...", "name=hello title=DUPMERGE");
```

```
}

//Convert BF images to a stack
run("Images to Stack", "name=STACKORI title=DUPMERGE use");
setBatchMode("exit and display");
titleGrey2=getTitle();

if (greenChannel==1){
	run("Merge Channels...", "c1=" + titleRight + " c2=" + titleLeft + " c4=" + titleGrey2);
} else {
	run("Merge Channels...", "c1=" + titleRight + " c4=" + titleGrey2);
}
rename(substring(imageName,0,lengthOf(imageName)-4)+"composite.tif");

//clean up
selectWindow(titleGrey2)
close()
```

7.6 KYMOGRAPH BUILDER CODE

```
filepath=getInfo("image.directory");
fileName=getInfo("image.filename");
n=roiManager("Count");
print(filepath);

//for every of region
for (i = 0; i < n-1; i=i+2) {
	//For cell widths build kymograph
	roiManager("Select", i);
	RoiName=Roi.getName();
	outputFile=filepath+fileName+"-"+"ROI-"+RoiName;
	roiManager("Save", outputFile+".roi");
	run("KymographBuilder", "input="+fileName);

	//For cell lengths record length
	roiManager("Select", i+1);
	length=getValue("Length");

	//Save kymograph appending length to file name
	selectWindow(fileName+" (Projected Kymograph)");
	saveAs("Tiff", outputFile+"-Kymograph-"+length);
	close();
	selectWindow(fileName);
}

//Save region of interest
roiManager("save", filepath+fileName+"-ROIs.zip");
```

7.7 KYMOGRAPH ANALYSIS CODE

```
//declare variables
centroids=newArray();
x=newArray();
y=newArray();
displacement=newArray();
time=newArray();
index=0;
pixel_size=117/4;
time_interval=2;

//Print title, convert to 8 bit, denoise and upsample by 4x
print(getTitle());
run("8-bit");
run("Subtract...", "value=55");
run("Scale...", "x=4 y=4 interpolation=Bilinear create");

//Get image dimentions for loops
width=getWidth();
height=getHeight();

//Outer loop with j counter is moving from top to bottom of kymograph
//Inner loop with j counter is calculating the centroid of that line
for(j=0;j<=height;j++){
	xg=0;
	g=0;
	for(i=0;i<=width;i++){
		g+=getPixel(i,j);
		xg+=getPixel(i,j)*(i);
	}
	centroid=xg/g;
	if(isNaN(centroid)){
	} else{
		centroids[j]=centroid;
		x[index]=round(centroid);
		y[index]=j;
		index++;
	}
}

//Use centroid location for each line to mark line on image
makeSelection("polyline",x,y);

//Convert pixels to nm
for(i=0;i<x.length;i++){
	displacement[i]=x[i]*pixel_size;
}
```

```
//Convert kymograph lines to seconds
for(i=0;i<x.length;i++){
        time[i]=y[i]*time_interval;
}

//Print data for further analysis
Array.print(time);
Array.print(displacement);
```

8 REFERENCES

Abbe, E. (1873) ‘Beiträge zur Theorie des Mikroskops und der mikroskopischen Wahrnehmung’, *Archiv für Mikroskopische Anatomie*. Springer-Verlag, 9(1), pp. 413–418. doi: 10.1007/BF02956173.

Abramowitz, M. and Davidson, M. W. (2015) *Immersion Media, Molecular Expressions*. Available at: https://micro.magnet.fsu.edu/primer/anatomy/immersion.html (Accessed: 3 January 2024).

Agard, D. A. and Sedat, J. W. (1983) ‘Three-dimensional architecture of a polytene nucleus’, *Nature*, 302(5910), pp. 676–681. doi: 10.1038/302676a0.

Aizawa, S.-I. (2014) *The flagellar world : electron microscopic images of bacterial flagella and related surface structures*. Oxford: Academic Press.

Albertazzi, L. and Zijlstra, P. (2024) *Super-Resolution Microscopy for Material Science*. Boca Raton: CRC Press. doi: https://doi.org/10.1201/9781003220688.

Allan, D. B. *et al.* (2024) ‘soft-matter/trackpy: v0.6.2’. Zenodo. doi: 10.5281/zenodo.10696534.

Armitage, J. P. (2022) ‘Swimming Using a Unidirectionally Rotating, Single Stopping Flagellum in the Alpha Proteobacterium Rhodobacter sphaeroides’, *Frontiers in microbiology*. Frontiers Media SA, 13, p. 893524. doi: 10.3389/fmicb.2022.893524.

Axelrod, D. (1981) ‘Cell-substrate contacts illuminated by total internal reflection fluorescence’, *The Journal of Cell Biology*, 89(1), pp. 141–145. doi: 10.1083/jcb.89.1.141.

Backlund, M. P. *et al.* (2013) ‘The double-helix point spread function enables precise and accurate measurement of 3D single-molecule localization and orientation’, in *Proc.SPIE*, p. 85900L. doi: 10.1117/12.2001671.

Balsalobre, C. *et al.* (1993) ‘Using the metabolic capacity of rhodobacter sphaeroides to assess

heavy metal toxicity', *Environmental Toxicology and Water Quality*. John Wiley & Sons, Ltd, 8(4), pp. 437–450. doi: https://doi.org/10.1002/tox.2530080408.

Balzarotti, F. *et al.* (2017) 'Nanometer resolution imaging and tracking of fluorescent molecules with minimal photon fluxes', *Science*. American Association for the Advancement of Science, 355(6325), pp. 606–612. doi: 10.1126/science.aak9913.

Barak, L. S. and Webb, W. W. (1982) 'Diffusion of low density lipoprotein-receptor complex on human fibroblasts ', *Journal of Cell Biology*, 95(3), pp. 846–852. doi: 10.1083/jcb.95.3.846.

Berman, H. M. *et al.* (2000) 'The Protein Data Bank', *Nucleic Acids Research*, 28(1), pp. 235–242. doi: 10.1093/nar/28.1.235.

Betzig, E. (1995) 'Proposed method for molecular optical imaging', *Opt. Lett.* Optica Publishing Group, 20(3), pp. 237–239. doi: 10.1364/OL.20.000237.

Betzig, E. *et al.* (2006) 'Imaging Intracellular Fluorescent Proteins at Nanometer Resolution', *Science*. American Association for the Advancement of Science, 313(5793), pp. 1642–1645. doi: 10.1126/science.1127344.

Bisson-Filho, A. W. *et al.* (2017) 'Treadmilling by FtsZ filaments drives peptidoglycan synthesis and bacterial cell division.', *Science (New York, N.Y.)*. American Association for the Advancement of Science, 355(6326), pp. 739–743. doi: 10.1126/science.aak9973.

de Boer, P., Crossley, R. and Rothfield, L. (1992) 'The essential bacterial cell-division protein FtsZ is a GTPase.', *Nature*. England, 359(6392), pp. 254–256. doi: 10.1038/359254a0.

Buddelmeijer, N. and Beckwith, J. (2002) 'Assembly of cell division proteins at the E. coli cell center.', *Current opinion in microbiology*. England, 5(6), pp. 553–557. doi: 10.1016/s1369-5274(02)00374-0.

Chakrova, N. *et al.* (2015) 'Studying different illumination patterns for resolution improvement in fluorescence microscopy', *Optics Express*, 23(24), p. 31367. Available at:

https://www.osapublishing.org/abstract.cfm?URI=oe-23-24-31367 (Accessed: 20 June 2019).

Chalfie, M. *et al.* (1994) 'Green fluorescent protein as a marker for gene expression.', *Science (New York, N.Y.)*. United States, 263(5148), pp. 802–805. doi: 10.1126/science.8303295.

Cheng, L.-C. *et al.* (2014) 'Nonlinear structured-illumination enhanced temporal focusing multiphoton excitation microscopy with a digital micromirror device', *Biomedical Optics Express*. The Optical Society, 5(8), p. 2526. doi: 10.1364/boe.5.002526.

Chiu, S.-W. (2014) *Spatiotemporal Dynamics of Cytoskeletal and Chemosensory Proteins in the Bacterium Rhodobacter sphaeroides*. Oxford University.

Chiu, S. W. *et al.* (2013) 'Positioning of chemosensory proteins and ftsz through the rhodobacter sphaeroides cell cycle', *Molecular Microbiology*, 90(2), pp. 322–337. doi: 10.1111/mmi.12366.

Chung, E., Kim, D. and So, P. T. C. (2006) 'Extended resolution wide-field optical imaging: objective-launched standing-wave total internal reflection fluorescence microscopy', *Optics Letters*. Optical Society of America, 31(7), p. 945. doi: 10.1364/OL.31.000945.

Cnossen, J. *et al.* (2020) 'Localization microscopy at doubled precision with patterned illumination', *Nature Methods*, 17(1), pp. 59–63. doi: 10.1038/s41592-019-0657-7.

Cole, N. B. (2013) 'Site-specific protein labeling with SNAP-tags.', *Current protocols in protein science*. United States, 73, pp. 30.1.1-30.1.16. doi: 10.1002/0471140864.ps3001s73.

Coltharp, C. *et al.* (2016) 'Defining the rate-limiting processes of bacterial cytokinesis.', *Proceedings of the National Academy of Sciences of the United States of America*. United States, 113(8), pp. E1044-53. doi: 10.1073/pnas.1514296113.

Coons, A. H., Creech, H. J. and Jones, R. N. (1941) 'Immunological Properties of an Antibody Containing a Fluorescent Group.', *Proceedings of the Society for Experimental Biology and Medicine*. SAGE Publications, 47(2), pp. 200–202. doi: 10.3181/00379727-47-13084P.

Corrales-Guerrero, L. *et al.* (2020) 'Molecular architecture of the DNA-binding sites of the P-

loop ATPases MipZ and ParA from Caulobacter crescentus', *Nucleic acids research*, 48(9), pp. 4769–4779. doi: 10.1093/nar/gkaa192.

Corrales-Guerrero, L. *et al.* (2022) 'MipZ caps the plus-end of FtsZ polymers to promote their rapid disassembly', *Proceedings of the National Academy of Sciences*. Proceedings of the National Academy of Sciences, 119(50), p. e2208227119. doi: 10.1073/pnas.2208227119.

Culley, S. *et al.* (2018) 'SRRF: Universal live-cell super-resolution microscopy.', *The international journal of biochemistry & cell biology*. Netherlands, 101, pp. 74–79. doi: 10.1016/j.biocel.2018.05.014.

Dan, D. *et al.* (2013) 'DMD-based LED-illumination Super-resolution and optical sectioning microscopy', *Scientific Reports*. Nature Publishing Group, 3(1), p. 1116. doi: 10.1038/srep01116.

Darafsheh, A. *et al.* (2014) 'Advantages of microsphere-assisted super-resolution imaging technique over solid immersion lens and confocal microscopies', *Applied Physics Letters*. American Institute of Physics Inc., 104(6). doi: 10.1063/1.4864760.

Diaspro, A. (2011) *Optical fluorescence microscopy : from the spectral to the nano dimension*, *Optical fluorescence microscopy : from the spectral to the nano dimension*. Heidelberg ; Springer.

Dubarry, N. *et al.* (2019) 'In Vivo Imaging of the Segregation of the 2 Chromosomes and the Cell Division Proteins of Rhodobacter sphaeroides Reveals an Unexpected Role for MipZ.', *mBio*, 10(1), pp. e02515-18. Available at: http://www.ncbi.nlm.nih.gov/pubmed/30602584.

Duggan, P. S., Parker, S. D. and Phillips-Jones, M. K. (2000) 'Characterisation of a Rhodobacter sphaeroides gene that encodes a product resembling Escherichia coli cytochrome b561 and R. sphaeroides cytochrome b562', *FEMS Microbiology Letters*, 189(2), pp. 239–246. doi: 10.1111/j.1574-6968.2000.tb09237.x.

Edelstein, A. D. *et al.* (2014) 'Advanced methods of microscope control using μManager software.', *Journal of biological methods*. United States, 1(2). doi: 10.14440/jbm.2014.36.

Erickson, H. P. (1995) ‘FtsZ, a prokaryotic homolog of tubulin?’, *Cell*. United States, 80(3), pp. 367–370. doi: 10.1016/0092-8674(95)90486-7.

Fedosseev, R. *et al.* (2005) ‘Structured light illumination for extended resolution in fluorescence microscopy’, *Optics and Lasers in Engineering*. Elsevier, 43(3–5), pp. 403–414. doi: 10.1016/j.optlaseng.2004.04.008.

Fiolka, R., Beck, M. and Stemmer, A. (2008) ‘Structured illumination in total internal reflection fluorescence microscopy using a spatial light modulator’, *Optics Letters*. The Optical Society, 33(14), p. 1629. doi: 10.1364/ol.33.001629.

Fish, K. N. (2022) ‘Total Internal Reflection Fluorescence (TIRF) Microscopy’, *Current Protocols*. John Wiley & Sons, Ltd, 2(8), p. e517. doi: https://doi.org/10.1002/cpz1.517.

Fu, G. *et al.* (2010) ‘In Vivo Structure of the E. coli FtsZ-ring Revealed by Photoactivated Localization Microscopy (PALM)’, *PLOS ONE*. Public Library of Science, 5(9), p. e12680. Available at: https://doi.org/10.1371/journal.pone.0012680.

Gest, H. (2004) ‘The discovery of microorganisms by Robert Hooke and Antoni van Leeuwenhoek, Fellows of The Royal Society’, *Notes and Records of the Royal Society of London*, 58(2), pp. 187–201. doi: 10.1098/rsnr.2004.0055.

Gibson, B. *et al.* (2018) ‘The distribution of bacterial doubling times in the wild.’, *Proceedings. Biological sciences*. England, 285(1880). doi: 10.1098/rspb.2018.0789.

Gibson, D. G. *et al.* (2009) ‘Enzymatic assembly of DNA molecules up to several hundred kilobases’, *Nature Methods 2009 6:5*. Nature Publishing Group, 6(5), pp. 343–345. doi: 10.1038/nmeth.1318.

Gliko, O., Brownell, W. E. and Saggau, P. (2009) ‘Fast two-dimensional standing-wave total-internal-reflection fluorescence microscopy using acousto-optic deflectors’, *Optics Letters*. The Optical Society, 34(6), p. 836. doi: 10.1364/ol.34.000836.

Goehring, N. W. and Beckwith, J. (2005) 'Diverse paths to midcell: assembly of the bacterial cell division machinery.', *Current biology : CB*. England, 15(13), pp. R514-26. doi: 10.1016/j.cub.2005.06.038.

Goley, E. D. *et al.* (2010) 'Imaging-based identification of a critical regulator of FtsZ protofilament curvature in Caulobacter', *Molecular Cell*, 39(6), pp. 975–987. doi: 10.1016/j.molcel.2010.08.027.

Göttfert, F. *et al.* (2013) 'Coaligned Dual-Channel STED Nanoscopy and Molecular Diffusion Analysis at 20 nm Resolution', *Biophysical Journal*, 105(1), pp. L01–L03. doi: https://doi.org/10.1016/j.bpj.2013.05.029.

Guenther, B. D. and Steel, D. G. (2018) *Encyclopedia of modern optics, Encyclopedia of Modern Optics*. Oxford: Elsevier Academic Press. doi: 10.5860/choice.43-0036.

Gustafsson, Agard and Sedat (1999) 'I5M: 3D widefield light microscopy with better than 100 nm axial resolution', *Journal of Microscopy*, 195(1), pp. 10–16. doi: https://doi.org/10.1046/j.1365-2818.1999.00576.x.

Gustafsson, M. G. (2000) 'Surpassing the lateral resolution limit by a factor of two using structured illumination microscopy.', *Journal of microscopy*. England, 198(Pt 2), pp. 82–87. doi: 10.1046/j.1365-2818.2000.00710.x.

Gustafsson, M. G. L. (2000) 'Surpassing the lateral resolution limit by a factor of two using structured illumination microscopy', *Journal of Microscopy*. Wiley/Blackwell (10.1111), 198(2), pp. 82–87. doi: 10.1046/j.1365-2818.2000.00710.x.

Gustafsson, M. G. L. (2005) 'Nonlinear structured-illumination microscopy: Wide-field fluorescence imaging with theoretically unlimited resolution', *Proceedings of the National Academy of Sciences of the United States of America*. National Academy of Sciences, 102(37), pp. 13081–13086. doi: 10.1073/pnas.0406877102.

Gustafsson, M. G. L. *et al.* (2008) 'Three-dimensional resolution doubling in wide-field fluorescence microscopy by structured illumination', *Biophysical Journal*. Biophysical Society, 94(12), pp. 4957–4970. doi: 10.1529/biophysj.107.120345.

Gustafsson, M. G. L., Agard, D. A. and Sedat, J. W. (2000) 'Doubling the lateral resolution of wide-field fluorescence microscopy using structured illumination', in Conchello, J.-A. et al. (eds) *Three-Dimensional and Multidimensional Microscopy: Image Acquisition Processing VII*. SPIE, pp. 141–150. doi: 10.1117/12.384189.

Gustafsson, M. G. L., Agard, D. a and Sedat, J. W. (1995) 'Sevenfold improvement of axial resolution in 3D wide-field microscopy using two objective lenses', *Proceedings of SPIE*, 2412(1), pp. 147–156. doi: 10.1117/12.205334.

Hall, N. and Dobbie, I. (2022) 'Structured Illumination Microscopy', in. Switzerland: Springer International Publishing AG, pp. 173–194. doi: 10.1007/978-3-031-04477-9_7.

Heilemann, M. *et al.* (2008) 'Subdiffraction-resolution fluorescence imaging with conventional fluorescent probes', *Angewandte Chemie - International Edition*, 47(33), pp. 6172–6176. doi: 10.1002/anie.200802376.

Heintzmann, R. and Cremer, C. G. (1999) 'Laterally modulated excitation microscopy: improvement of resolution by using a diffraction grating', *Optical Biopsies and Microscopic Techniques*, III(January 1999), pp. 185–196. doi: 10.1117/12.336833.

Heintzmann, R. and Huser, T. (2017) 'Super-Resolution Structured Illumination Microscopy', *Chemical Reviews*. American Chemical Society, pp. 13890–13908. doi: 10.1021/acs.chemrev.7b00218.

Hell, S. and Stelzer, E. H. K. (1992) 'Properties of a 4Pi confocal fluorescence microscope', *J. Opt. Soc. Am. A*. Optica Publishing Group, 9(12), pp. 2159–2166. doi: 10.1364/JOSAA.9.002159.

Hell, S. W. *et al.* (1994) 'Confocal microscopy with an increased detection aperture: type-B 4Pi

confocal microscopy', *Opt. Lett.* Optica Publishing Group, 19(3), pp. 222–224. doi: 10.1364/OL.19.000222.

Hell, S. W. and Wichmann, J. (1994) 'Breaking the diffraction resolution limit by stimulated emission: stimulated-emission-depletion fluorescence microscopy', *Optics Letters*, 19(11), p. 780. doi: 10.1364/OL.19.000780.

Hess, S. T., Girirajan, T. P. K. and Mason, M. D. (2006) 'Ultra-high resolution imaging by fluorescence photoactivation localization microscopy', *Biophysical Journal*, 91(11), pp. 4258–4272. doi: 10.1529/biophysj.106.091116.

Hirvonen, L. M. *et al.* (2009) 'Structured illumination microscopy of a living cell', *European Biophysics Journal*. Springer-Verlag, 38(6), pp. 807–812. doi: 10.1007/s00249-009-0501-6.

Huang, B. *et al.* (2008) 'Three-dimensional super-resolution imaging by stochastic optical reconstruction microscopy.', *Science (New York, N.Y.)*. American Association for the Advancement of Science, 319(5864), pp. 810–3. doi: 10.1126/science.1153529.

Hussain, S. *et al.* (2018) 'MreB filaments align along greatest principal membrane curvature to orient cell wall synthesis', *eLife*. Edited by T. Mignot. eLife Sciences Publications, Ltd, 7, p. e32471. doi: 10.7554/eLife.32471.

Ind, A. C. *et al.* (2009) 'Inducible-expression plasmid for Rhodobacter sphaeroides and Paracoccus denitrificans', *Applied and Environmental Microbiology*, 75(20), pp. 6613–6615. doi: 10.1128/AEM.01587-09.

Ippolito, S. B., Goldberg, B. B. and Ünlü, M. S. (2005) 'Theoretical analysis of numerical aperture increasing lens microscopy', *Journal of Applied Physics*, 97(5), p. 53105. doi: 10.1063/1.1858060.

Jaschke, P. R. *et al.* (2011) 'Modification of the Genome of Rhodobacter sphaeroides and Construction of Synthetic Operons', in Voigt, C. B. T.-M. in E. (ed.) *Synthetic Biology, Part A*.

Academic Press, pp. 519–538. doi: 10.1016/b978-0-12-385075-1.00023-8.

Juette, M. F. *et al.* (2008) 'Three-dimensional sub-100 nm resolution fluorescence microscopy of thick samples', *Nature Methods*, 5(6), pp. 527–529. doi: 10.1038/nmeth.1211.

Justice, S. S., García-Lara, J. and Rothfield, L. I. (2000) 'Cell division inhibitors SulA and MinC/MinD block septum formation at different steps in the assembly of the Escherichia coli division machinery.', *Molecular microbiology*. England, 37(2), pp. 410–423. doi: 10.1046/j.1365-2958.2000.02007.x.

Katayama, R. *et al.* (2017) 'SIL-STED microscopy technique enhancing super-resolution of fluorescence microscopy', in Katayama R., T. Y. (ed.) *Proceedings of SPIE - The International Society for Optical Engineering*. SPIE. doi: 10.1117/12.2275957.

Keppler, A. *et al.* (2003) 'A general method for the covalent labeling of fusion proteins with small molecules in vivo', *Nature Biotechnology*, 21(1), pp. 86–89. doi: 10.1038/nbt765.

Khoo, J. H., Miller, H. and Armitage, J. P. (2022) 'Measurement of Macromolecular Crowding in Rhodobacter sphaeroides under Different Growth Conditions', *mBio*. American Society for Microbiology, 13(1), pp. e03672-21. doi: 10.1128/MBIO.03672-21.

Kiekebusch, D. *et al.* (2012) 'Localized Dimerization and Nucleoid Binding Drive Gradient Formation by the Bacterial Cell Division Inhibitor MipZ', *Molecular Cell*, 46(3), pp. 245–259. doi: 10.1016/j.molcel.2012.03.004.

Kiekebusch, D. and Thanbichler, M. (2014) 'Spatiotemporal organization of microbial cells by protein concentration gradients', *Trends in Microbiology*, pp. 65–73. doi: 10.1016/j.tim.2013.11.005.

Kim, W.-C. *et al.* (2017) 'Investigation on achieving super-resolution by solid immersion lens based STED microscopy', *Optics Express*. The Optical Society, 25(14), p. 16629. doi: 10.1364/oe.25.016629.

Kjaer, A. (2022) *Investigating bacteroidetes gliding motility*. University of Oxford.

Kner, P. *et al.* (2009) 'Super-resolution video microscopy of live cells by structured illumination', *Nature Methods*, 6(5), pp. 339–342. doi: 10.1038/nmeth.1324.

Lal, A., Shan, C. and Xi, P. (2016) 'Structured Illumination Microscopy Image Reconstruction Algorithm', *IEEE Journal of Selected Topics in Quantum Electronics*, 22(4), pp. 50–63. doi: 10.1109/JSTQE.2016.2521542.

Lambert, T. J. (2019) 'FPbase: a community-editable fluorescent protein database', *Nature Methods*, 16(4), pp. 277–278. doi: 10.1038/s41592-019-0352-8.

Landgraf, D. *et al.* (2012) 'Segregation of molecules at cell division reveals native protein localization', *Nature Methods*, 9(5), pp. 480–482. doi: 10.1038/nmeth.1955.

Lariviere, P. J. and Goley, E. D. (2022) 'Cell Division in Caulobacter crescentus: A Molecular-Scale Model BT - Cell Cycle Regulation and Development in Alphaproteobacteria', in Biondi, E. (ed.). Cham: Springer International Publishing, pp. 101–141. doi: 10.1007/978-3-030-90621-4_4.

Levin, P. A., Kurtser, I. G. and Grossman, A. D. (1999) 'Identification and characterization of a negative regulator of FtsZ ring formation in Bacillus subtilis.', *Proceedings of the National Academy of Sciences of the United States of America*. United States, 96(17), pp. 9642–9647. doi: 10.1073/pnas.96.17.9642.

Levin, P. A. and Losick, R. (1996) 'Transcription factor Spo0A switches the localization of the cell division protein FtsZ from a medial to a bipolar pattern in Bacillus subtilis.', *Genes & development*. United States, 10(4), pp. 478–488. doi: 10.1101/gad.10.4.478.

Li, D. *et al.* (2015) 'Extended-resolution structured illumination imaging of endocytic and cytoskeletal dynamics', *Science*, 349(6251). doi: 10.1126/science.aab3500.

Li, M. *et al.* (2020) 'Structured illumination microscopy using digital micro-mirror device and coherent light source', *Applied Physics Letters*, 116(23). doi: 10.1063/5.0008264.

Li, X. *et al.* (2017) 'Removal of cadmium and zinc from contaminated wastewater using Rhodobacter sphaeroides.', *Water science and technology : a journal of the International Association on Water Pollution Research*. England, 75(11–12), pp. 2489–2498. doi: 10.2166/wst.2016.608.

Li, Y. *et al.* (2018) 'MapZ Forms a Stable Ring Structure That Acts As a Nanotrack for FtsZ Treadmilling in Streptococcus mutans.', *ACS nano*. United States, 12(6), pp. 6137–6146. doi: 10.1021/acsnano.8b02469.

Liau, Z. L. *et al.* (2015) 'Solid-immersion fluorescence microscopy with increased emission and super resolution', *Journal of Applied Physics*, 117(1), p. 14502. doi: 10.1063/1.4905284.

Liu, P. Y. *et al.* (2014) 'Real-time Measurement of Single Bacterium's Refractive Index Using Optofluidic Immersion Refractometry', *Procedia Engineering*. No longer published by Elsevier, 87, pp. 356–359. doi: 10.1016/J.PROENG.2014.11.743.

Liu, Z. *et al.* (2005) 'High resolution, high collection efficiency in numerical aperture increasing lens microscopy of individual quantum dots', *Applied Physics Letters*, 87(7). doi: 10.1063/1.2012532.

Loose, M. and Mitchison, T. J. (2014) 'The bacterial cell division proteins ftsA and ftsZ self-organize into dynamic cytoskeletal patterns', *Nature Cell Biology*. Nature Publishing Group, 16(1), pp. 38–46. doi: 10.1038/ncb2885.

Los, G. V *et al.* (2005) 'HaloTag® Interchangeable Labeling Technology for Cell Imaging and Protein Capture', *Cell Notes*, (11), pp. 2–6. Available at: https://nld.promega.com/resources/pubhub/cellnotes/halotag-interchangeable-labeling-technology-for-cell-imaging-and-protein-capture/.

Los, G. V *et al.* (2008) 'HaloTag: A Novel Protein Labeling Technology for Cell Imaging and Protein Analysis', *ACS Chemical Biology*. American Chemical Society, 3(6), pp. 373–382. doi: 10.1021/cb800025k.

Lu-Walther, H.-W. *et al.* (2015) 'fastSIM: a practical implementation of fast structured illumination microscopy', *Methods and Applications in Fluorescence*. IOP Publishing, 3(1), p. 014001. doi: 10.1088/2050-6120/3/1/014001.

Lu-Walther, H.-W. *et al.* (2016) 'Nonlinear Structured Illumination Using a Fluorescent Protein Activating at the Readout Wavelength', *PLOS ONE*. Edited by V. E. Degtyar. Public Library of Science, 11(10), p. e0165148. doi: 10.1371/journal.pone.0165148.

Lutkenhaus, J. (2007) 'Assembly dynamics of the bacterial minCDE system and spatial regulation of the z ring', *Annual Review of Biochemistry*. Annual Reviews, pp. 539–562. doi: 10.1146/annurev.biochem.75.103004.142652.

Manley, S. *et al.* (2008) 'High-density mapping of single-molecule trajectories with photoactivated localization microscopy', *Nature Methods*. Nature Publishing Group, 5(2), pp. 155–157. doi: 10.1038/nmeth.1176.

Mansfield, S. M. and Kino, G. S. (1990) 'Solid immersion microscope', *Applied Physics Letters*. American Institute of Physics, 57(24), pp. 2615–2616. doi: 10.1063/1.103828.

Mary, H. (2022) 'KymographBuilder'. Available at: https://imagej.net/plugins/kymograph-builder.

Masuda, S. and Bauer, C. E. (2002) 'AppA Is a Blue Light Photoreceptor that Antirepresses Photosynthesis Gene Expression in Rhodobacter sphaeroides', *Cell*. United States: Elsevier Inc, 110(5), pp. 613–623. doi: 10.1016/S0092-8674(02)00876-0.

Masullo, L. A. *et al.* (2021) 'Pulsed Interleaved MINFLUX', *Nano Letters*. American Chemical Society, 21(1), pp. 840–846. doi: 10.1021/acs.nanolett.0c04600.

McQuillen, R. and Xiao, J. (2020) 'Insights into the Structure, Function, and Dynamics of the Bacterial Cytokinetic FtsZ-Ring', *Annual Review of Biophysics*. Annual Reviews, 49(1), pp. 309–341. doi: 10.1146/annurev-biophys-121219-081703.

Micron Oxford (2021) *Oxford Nanoimager (ONI)*. Available at: https://micronoxford.com/nanoimager.

Mollwitz, B. *et al.* (2012) 'Directed Evolution of the Suicide Protein O6-Alkylguanine-DNA Alkyltransferase for Increased Reactivity Results in an Alkylated Protein with Exceptional Stability', *Biochemistry*. American Chemical Society, 51(5), pp. 986–994. doi: 10.1021/bi2016537.

Monteiro, J. M. *et al.* (2018) 'Peptidoglycan synthesis drives an FtsZ-treadmilling-independent step of cytokinesis.', *Nature*. England, 554(7693), pp. 528–532. doi: 10.1038/nature25506.

Moore, D. A. *et al.* (2017) 'Probing for Binding Regions of the FtsZ Protein Surface through Site-Directed Insertions: Discovery of Fully Functional FtsZ-Fluorescent Proteins.', *Journal of bacteriology*. United States, 199(1). doi: 10.1128/JB.00553-16.

Müller, M. *et al.* (2016) 'Open-source image reconstruction of super-resolution structured illumination microscopy data in ImageJ', *Nature Communications*. Nature Publishing Group, 7(1), pp. 1–6. doi: 10.1038/ncomms10980.

Neil, M. A. A., Juškaitis, R. and Wilson, T. (1997) 'Method of obtaining optical sectioning by using structured light in a conventional microscope', *Opt. Lett.* Optica Publishing Group, 22(24), pp. 1905–1907. doi: 10.1364/OL.22.001905.

Nereng, K. S. and Kaplan, S. (1999) 'Genomic complexity among strains of the facultative photoheterotrophic bacterium Rhodobacter sphaeroides.', *Journal of bacteriology*. United States, 181(5), pp. 1684–1688. doi: 10.1128/JB.181.5.1684-1688.1999.

O'Holleran, K. and Shaw, M. (2012) 'Polarization effects on contrast in structured illumination microscopy', *Optics Letters*. Optical Society of America, 37(22), p. 4603. doi: 10.1364/OL.37.004603.

Olivo-Marin, J.-C. (2002) 'Extraction of spots in biological images using multiscale products',

Pattern Recognition, 35(9), pp. 1989–1996. doi: https://doi.org/10.1016/S0031-3203(01)00127-3.

Orsi, E. *et al.* (2021) 'The transition of Rhodobacter sphaeroides into a microbial cell factory', *Biotechnology and Bioengineering*. United States, 118(2), pp. 531–541. doi: 10.1002/bit.27593.

Penfold, R. J. and Pemberton, J. M. (1992) 'An improved suicide vector for construction of chromosomal insertion mutations in bacteria.', *Gene*. Netherlands, 118(1), pp. 145–146. doi: 10.1016/0378-1119(92)90263-o.

Perez, A. J. *et al.* (2019) 'Movement dynamics of divisome proteins and PBP2x:FtsW in cells of Streptococcus pneumoniae.', *Proceedings of the National Academy of Sciences of the United States of America*. United States, 116(8), pp. 3211–3220. doi: 10.1073/pnas.1816018116.

Peters, L. *et al.* (2019) 'Phototrophic purple bacteria as optoacoustic in vivo reporters of macrophage activity', *Nature Communications*, 10(1), p. 1191. doi: 10.1038/s41467-019-09081-5.

Potter, K. E. (2021) *Identification and characterisation of the type VI secretion system in rhodobacter sphaeroides*. University of Oxford.

RayChaudhuri, D. and Park, J. T. (1992) 'Escherichia coli cell-division gene ftsZ encodes a novel GTP-binding protein.', *Nature*. England, 359(6392), pp. 251–254. doi: 10.1038/359251a0.

Rayleigh (1879) 'XXXI. Investigations in optics, with special reference to the spectroscope', *The London, Edinburgh, and Dublin Philosophical Magazine and Journal of Science*. Taylor & Francis, 8(49), pp. 261–274. doi: 10.1080/14786447908639684.

Rego, E. H. *et al.* (2012) 'Nonlinear structured-illumination microscopy with a photoswitchable protein reveals cellular structures at 50-nm resolution', *Proceedings of the National Academy of Sciences*. National Academy of Sciences, 109(3), pp. E135–E143. doi: 10.1073/pnas.1107547108.

Rowlett, V. W. and Margolin, W. (2013) 'The bacterial Min system.', *Current biology : CB*. England, 23(13), pp. R553-6. doi: 10.1016/j.cub.2013.05.024.

Rowlett, V. W. and Margolin, W. (2014) '3D-SIM Super-resolution of FtsZ and its membrane tethers in Escherichia coli cells', *Biophysical Journal*. Biophysical Society, 107(8), pp. L17–L20. doi: 10.1016/j.bpj.2014.08.024.

Rusk, N. (2009) 'The fluorescence microscope', *Nature Cell Biology*, 11(S1), pp. S8–S9. doi: 10.1038/ncb1941.

Rust, M. J., Bates, M. and Zhuang, X. (2006) 'Sub-diffraction-limit imaging by stochastic optical reconstruction microscopy (STORM)', *Nature Methods*. Nature Publishing Group, 3(10), pp. 793–796. doi: 10.1038/nmeth929.

Sanderson, J. (2019) *Understanding Light Microscopy*, *Understanding Light Microscopy*. Hoboken, NJ: John Wiley & Sons Ltd (RMS-Wiley series). doi: 10.1002/9781118696736.

Sandmeyer, A. *et al.* (2019) 'DMD-based super-resolution structured illumination microscopy visualizes live cell dynamics at high speed and low cost', *bioRxiv*. Cold Spring Harbor Laboratory, pp. 1–32. doi: 10.1101/797670.

Sasaki, T. *et al.* (1997) 'Application of solid immersion lens to high-resolution photoluminescence imaging of patterned GaAs quantum wells', *Japanese Journal of Applied Physics, Part 2: Letters*. JJAP, 36(7 B), p. L962. doi: 10.1143/jjap.36.l962.

Saxton, M. J. (1997) 'Single-particle tracking: the distribution of diffusion coefficients', *Biophysical Journal*, 72(4), pp. 1744–1753. doi: https://doi.org/10.1016/S0006-3495(97)78820-9.

Schäfer, A. *et al.* (1994) 'Small mobilizable multi-purpose cloning vectors derived from the Escherichia coli plasmids pK18 and pK19: selection of defined deletions in the chromosome of Corynebacterium glutamicum', *Gene*, 145(1), pp. 69–73. doi: 10.1016/0378-1119(94)90324-7.

Schindelin, J. *et al.* (2012) 'Fiji: an open-source platform for biological-image analysis', *Nature Methods*, 9(7), pp. 676–682. doi: 10.1038/nmeth.2019.

Sehnal, D. *et al.* (2021) 'Mol* Viewer: modern web app for 3D visualization and analysis of large biomolecular structures', *Nucleic Acids Research*, 49(W1), pp. W431–W437. doi: 10.1093/nar/gkab314.

Shah, D. S. *et al.* (2000) 'Fine tuning bacterial chemotaxis: analysis of Rhodobacter sphaeroides behaviour under aerobic and anaerobic conditions by mutation of the major chemotaxis operons and cheY genes.', *The EMBO journal*. England, 19(17), pp. 4601–4613. doi: 10.1093/emboj/19.17.4601.

Shao, L. *et al.* (2008) 'I5S: Wide-field light microscopy with 100-nm-scale resolution in three dimensions', *Biophysical Journal*. Biophysical Society, 94(12), pp. 4971–4983. doi: 10.1529/biophysj.107.120352.

Shin, S. *et al.* (2018) 'Super-resolution three-dimensional fluorescence and optical diffraction tomography of live cells using structured illumination generated by a digital micromirror device', *Scientific Reports*, 8(1), p. 9183. doi: 10.1038/s41598-018-27399-w.

Sockett, R. E., Foster, J. C. A. and Armitage, J. P. (1990) 'Molecular Biology of the Rhodobacter Sphaeroides Flagellum', in Drews, G. and Dawes, E. A. (eds) *Molecular Biology of Membrane-Bound Complexes in Phototrophic Bacteria*. Boston, MA: Springer US, pp. 473–478. doi: 10.1007/978-1-4757-0893-6_55.

Sockett, R. Elizabeth, Foster, J. C. A. and Armitage, J. P. (1990) 'Molecular Biology of the Rhodobacter Sphaeroides Flagellum', *Molecular Biology of Membrane-Bound Complexes in Phototrophic Bacteria*. Springer, Boston, MA, pp. 473–478. doi: 10.1007/978-1-4757-0893-6_55.

Stokes, G. G. (1852) 'XXX. On the change of refrangibility of light', *Philosophical Transactions of the Royal Society of London*, 142, pp. 463–562. doi: 10.1098/rstl.1852.0022.

Strauss, M. P. *et al.* (2012) '3D-SIM Super Resolution Microscopy Reveals a Bead-Like Arrangement for FtsZ and the Division Machinery: Implications for Triggering Cytokinesis', *PLOS Biology*. Public Library of Science, 10(9), p. e1001389. Available at: https://doi.org/10.1371/journal.pbio.1001389.

Sun, Q. and Margolin, W. (1998) 'FtsZ dynamics during the division cycle of live Escherichia coli cells.', *Journal of bacteriology*. United States, 180(8), pp. 2050–2056. doi: 10.1128/JB.180.8.2050-2056.1998.

Sundararajan, K. *et al.* (2015) 'The bacterial tubulin FtsZ requires its intrinsically disordered linker to direct robust cell wall construction', *Nature Communications*. Nature Publishing Group, 6(1), pp. 1–14. doi: 10.1038/ncomms8281.

Suwanto, A. and Kaplan, S. (1989) 'Physical and genetic mapping of the Rhodobacter sphaeroides 2.4.1 genome: genome size, fragment identification, and gene localization', *Journal of Bacteriology*. American Society for Microbiology, 171(11), pp. 5840–5849. doi: 10.1128/jb.171.11.5840-5849.1989.

TelescopeOptics.net (2006) *COHERENT TRANSFER FUNCTION, FOURIER TRANSFORM*. Available at: https://www.telescope-optics.net/mtf2.htm (Accessed: 17 December 2023).

Terris, B. D. *et al.* (1994) 'Near-field optical data storage using a solid immersion lens', *Applied Physics Letters*. American Institute of Physics, 65(4), pp. 388–390. doi: 10.1063/1.112341.

Thanbichler, M. and Shapiro, L. (2006a) 'Chromosome organization and segregation in bacteria.', *Journal of structural biology*. United States, 156(2), pp. 292–303. doi: 10.1016/j.jsb.2006.05.007.

Thanbichler, M. and Shapiro, L. (2006b) 'MipZ, a Spatial Regulator Coordinating Chromosome Segregation with Cell Division in Caulobacter', *Cell*. Elsevier, 126(1), pp. 147–162. doi: 10.1016/j.cell.2006.05.038.

Thorlabs (2023) *Spatial Filters Tutorial*. Available at:

https://www.thorlabs.com/newgrouppage9.cfm?objectgroup_id=10768 (Accessed: 23 December 2023).

Tokunaga, M., Imamoto, N. and Sakata-Sogawa, K. (2008) 'Highly inclined thin illumination enables clear single-molecule imaging in cells', *Nature Methods 2008 5:2*. Nature Publishing Group, 5(2), pp. 159–161. doi: 10.1038/nmeth1171.

Toro-Nahuelpan, M. *et al.* (2019) 'A gradient-forming MipZ protein mediating the control of cell division in the magnetotactic bacterium Magnetospirillum gryphiswaldense', *Molecular Microbiology*, 112(5), pp. 1423–1439. doi: 10.1111/mmi.14369.

Tsang, M.-J., Yakhnina, A. A. and Bernhardt, T. G. (2017) 'NlpD links cell wall remodeling and outer membrane invagination during cytokinesis in Escherichia coli.', *PLoS genetics*. United States, 13(7), p. e1006888. doi: 10.1371/journal.pgen.1006888.

Vangindertael, J. *et al.* (2018) 'An introduction to optical super-resolution microscopy for the adventurous biologist', *Methods and Applications in Fluorescence*. IOP Publishing, 6(2). doi: 10.1088/2050-6120/aaae0c.

Vicidomini, G., Bianchini, P. and Diaspro, A. (2018) 'STED super-resolved microscopy', *Nature Methods*, 15(3), pp. 173–182. doi: 10.1038/nmeth.4593.

Wagstaff, J. M. *et al.* (2017) 'A Polymerization-Associated Structural Switch in FtsZ That Enables Treadmilling of Model Filaments.', *mBio*. United States, 8(3). doi: 10.1128/mBio.00254-17.

Wang, L. (2010) *High-resolution Structured Illumination Solid Immersion Fluorescence Microscopy*. University of Nottingham.

Wang, L. *et al.* (2012) 'Highly confined surface imaging by solid immersion total internal reflection fluorescence microscopy', *Optics Express*. Optical Society of America, 20(3), p. 3311. doi: 10.1364/OE.20.003311.

Wang, L. *et al.* (2019) 'Solid immersion microscopy images cells under cryogenic conditions with 12 nm resolution', *Communications Biology*. Nature Publishing Group, 2(1), p. 74. doi: 10.1038/s42003-019-0317-6.

Wang, L., Pitter, M. C. and Somekh, M. G. (2010) 'Wide-field high-resolution solid immersion fluorescence microscopy applying an aplanatic solid immersion lens', *Applied Optics*. Optical Society of America, 49(31), p. 6160. doi: 10.1364/AO.49.006160.

Wang, L., Pitter, M. C. and Somekh, M. G. (2011a) 'Wide-field high-resolution structured illumination solid immersion fluorescence microscopy', *Optics Letters*. Optical Society of America, 36(15), p. 2794. doi: 10.1364/OL.36.002794.

Wang, L., Pitter, M. C. and Somekh, M. G. (2011b) 'Wide-field high-resolution structured illumination solid immersion fluorescence microscopy', *Optics Letters*. Optical Society of America, 36(15), p. 2794. doi: 10.1364/OL.36.002794.

Whitley, K. D. *et al.* (2021) 'FtsZ treadmilling is essential for Z-ring condensation and septal constriction initiation in Bacillus subtilis cell division', *Nature Communications*, 12(1), p. 2448. doi: 10.1038/s41467-021-22526-0.

Whitley, K. D. *et al.* (2022) 'High-resolution imaging of bacterial spatial organization with vertical cell imaging by nanostructured immobilization (VerCINI)', *Nature Protocols*, 17(3), pp. 847–869. doi: 10.1038/s41596-021-00668-1.

Wildanger, D. *et al.* (2012) 'Solid immersion facilitates fluorescence microscopy with nanometer resolution and sub-Ångström emitter localization', *Advanced Materials*. John Wiley & Sons, Ltd, 24(44), pp. OP309–OP313. doi: 10.1002/adma.201203033.

Wilhelm, J. *et al.* (2021) 'Kinetic and Structural Characterization of the Self-Labeling Protein Tags HaloTag7, SNAP-tag, and CLIP-tag', *Biochemistry*. American Chemical Society, 60(33), pp. 2560–2575. doi: 10.1021/acs.biochem.1c00258.

Woldemeskel, S. A. *et al.* (2017) 'A conserved coiled-coil protein pair focuses the cytokinetic Z-ring in Caulobacter crescentus', *Molecular Microbiology*, 105(5), pp. 721–740. doi: 10.1111/mmi.13731.

Wu, Q. *et al.* (1999) 'Realization of numerical aperture 2.0 using a gallium phosphide solid immersion lens', *Applied Physics Letters*, 75(26), pp. 4064–4066. doi: 10.1063/1.125537.

Wu, Q., Ghislain, L. P. and Elings, V. B. (2000) 'Imaging with solid immersion lenses, spatial resolution, and applications', *Proceedings of the IEEE*. Institute of Electrical and Electronics Engineers Inc., 88(9), pp. 1491–1498. doi: 10.1109/5.883320.

Wu, Y. and Shroff, H. (2018) 'Faster, sharper, and deeper: structured illumination microscopy for biological imaging', *Nature Methods*. Nature Publishing Group, pp. 1011–1019. doi: 10.1038/s41592-018-0211-z.

Yang, X. *et al.* (2017) 'GTPase activity-coupled treadmilling of the bacterial tubulin FtsZ organizes septal cell wall synthesis.', *Science (New York, N.Y.)*. United States, 355(6326), pp. 744–747. doi: 10.1126/science.aak9995.

Young, G. *et al.* (2018) 'Quantitative mass imaging of single biological macromolecules.', *Science (New York, N.Y.)*. United States, 360(6387), pp. 423–427. doi: 10.1126/science.aar5839.

Zhang, J. *et al.* (2006) 'Surface-plasmon microscopy with a two-piece solid immersion lens: Bright and dark fields', *Applied Optics*. OSA - The Optical Society, 45(31), pp. 7977–7986. doi: 10.1364/AO.45.007977.

Zhang, J., See, C. W. and Somekh, M. G. (2007) 'Imaging performance of widefield solid immersion lens microscopy', *Applied Optics*. OSA - The Optical Society, 46(20), pp. 4202–4208. doi: 10.1364/AO.46.004202.